論文 / 著書情報
Article / Book Information

題目(和文)	
Title(English)	Catalytic Conversion of Tar Using Nickel Nanoparticles Embedded in the Rice Husk Char for Biomass Gasification
著者(和文)	Yafei Shen
Author(English)	Yafei Shen
出典(和文)	学位:博士（工学）, 学位授与機関:東京工業大学, 報告番号:甲第9842号, 授与年月日:2015年3月26日, 学位の種別:課程博士, 審査員:吉川　邦夫,加茂　徹,高橋　史武,時松　宏治,梶谷　史朗
Citation(English)	Degree:, Conferring organization: Tokyo Institute of Technology, Report number:甲第9842号, Conferred date:2015/3/26, Degree Type:Course doctor, Examiner:,,,,
学位種別(和文)	博士論文
Type(English)	Doctoral Thesis

Table of Contents

Chapter 1

General Introduction

1.1 Biomass Energy

Biomass is carbon based and is composed of a mixture of organic molecules containing hydrogen, usually including atoms of oxygen, often nitrogen and small quantities of other atoms, including silica, alkali, alkaline earth and heavy metals. Biomass is a renewable energy resource derived from biological sources, such as energy crops, agricultural residues, forestry residues, algal biomass and municipal solid wastes. Biomass utilization is recognized as one of the most promising solutions for current energy and environmental problems. Alternative renewable energy technologies such as hydropower energy, solar energy and wind power, which often suffer from intermittent power generation issue, are less reliable in term of security of supply. Meanwhile, biomass is the only renewable energy source that can be converted into liquid fuel and used as feedstock in chemicals synthesis [1-1]. For instance, the biomass power generating industry in the United States, consisting of approximately 11,000 MW of summer operating capacity actively supplying power to the grid, can produce about 1.4% of the U.S. electricity supply. Fig. 1 illustrates the trends of the top five countries in generating electricity from biomass. It can be indicated that the electricity generated from biomass significantly increase, especially for China in recent years, thus requiring a further development of biomass utilization for electricity and biofuels.

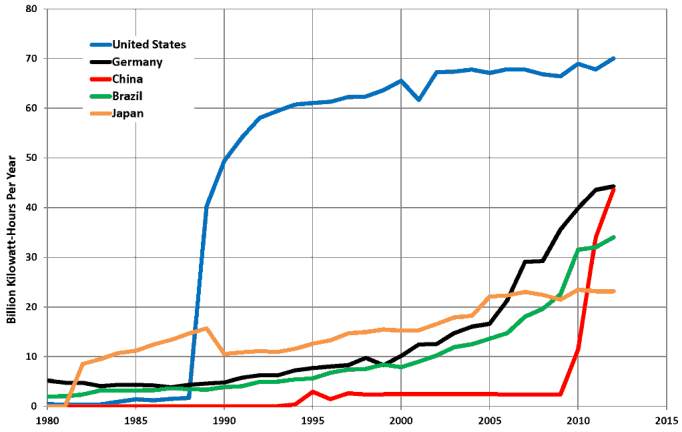

Figure 1.1 Trends in the top five countries generating electricity from biomass (*Adapted from Wikipedia*)

1.2 Biomass Pyrolysis/Gasification

The thermochemical process including combustion, pyrolysis and gasification can convert biomass into the useful bioenergy (i.e., fuel gas, bio-oil) and biochar. Biomass pyrolysis or gasification is recognized as one of the most promising technologies for producing sustainable fuels that could be used for power generation systems or syngas applications. For instance, biomass pyrolysis at higher temperatures would produce the bio-char, bio-oil and syngas for boiler and power generation (Fig. 1.2). Moreover, the proportion of the derived products, to some extent, depends on the pyrolysis temperature and other conditions. Compared with the partial oxidative gasification process, the inert high-temperature pyrolysis of biomass has low process efficiency, but can produce fuel gas with a high heating value [1-2]. Pyrolysis can be divided into three subclasses; slow pyrolysis, fast pyrolysis and flash pyrolysis [1-3]. The main operational parameters are outlined in Table 1.1. Significantly, gasification of biomass has several environmental advantages over fossil fuels, namely lower emission of CO_2 and other flue gases such as H_2S, SO_2, NO_x [1-3], [1-4], [1-5], [1-6], [1-7]. Biomass gasification is a thermochemical process in which biomass undergoes the incomplete combustion to produce a gas product referred to syngas that mainly consists of H_2, CO, CH_4, CO_2, and N_2 (if air or N_2 is used as the carrier gas) in various proportions. Biomass pyrolysis or gasification

has many advantages compared to the direct combustion. The main reasons are that it can convert the low-value feedstocks to high quality combustible synthesis gas, which can be not only directly burned or used for electricity generation but also turned into liquid transportation fuels [1-8].

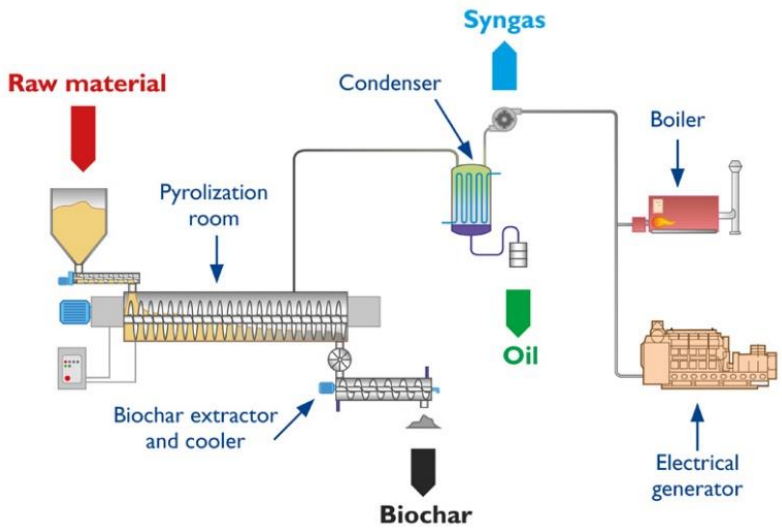

Figure 1.2 Pyrolysis of biomass for bio-char, oil and syngas production (*Adapted from Google*)

Table 1.1 Operating Parameters of the Pyrolysis Process [1-3]

Pyrolysis	Heating rate (K/s)	Residence time (s)	Temperature (^oC)	Particle size (mm)	Product
Slow	<1	300-1800	400 600	5-50	Char Gas, oil, char
Fast	500-10^5	0.5-5	500-650	<1	70% oil 15% char 15% gas
Flash	>10^5	<1 <1 <0.5	<650 >650 1000	<0.2	Oil Gas Gas

Processes occurring in biomass gasification are often distinguished: drying and devolatilization, volatile and char combustion, and gasification and tar reforming with steam and CO_2. These processes can be identified in certain spatial regions in fixed bed gasifiers [1-9]. As for biomass pyrolysis illustrated in Fig. 1.3, during transient heating of the particle, temperature increases locally, leading first to the evaporation of moisture (drying stage) and then to the progressive release of pyrolytic volatiles (*primary pyrolysis stage*). The primary volatiles are produced from the thermal scission of chemical bonds in the individual constituents of biomass, which are cellulose, hemicellulose, lignin and extractives, and comprise permanent gas species (*e.g., CO_2, CO, CH_4*) along with the condensable species at ambient conditions (i.e., some organic compounds and water). Although each of the biomass constituents decompose at faster rates in different temperature ranges, the primary pyrolysis stage is complete at lower temperatures (*<500 °C*), thereby yielding a carbon-rich non-volatile solid that is called char or charcoal. The produced char also contain a significant part of the mineral matter originally present in the parent fuel. Nevertheless, if the fuel is converted at higher temperatures some of the primary volatiles released inside the particle can further participate in a variety of secondary reactions to form product "2". Serial and parallel reactions can occur, either heterogeneously or homogeneously, such as the cracking, the reforming, the dehydration, and so on [1-10], [1-11], [1-12].

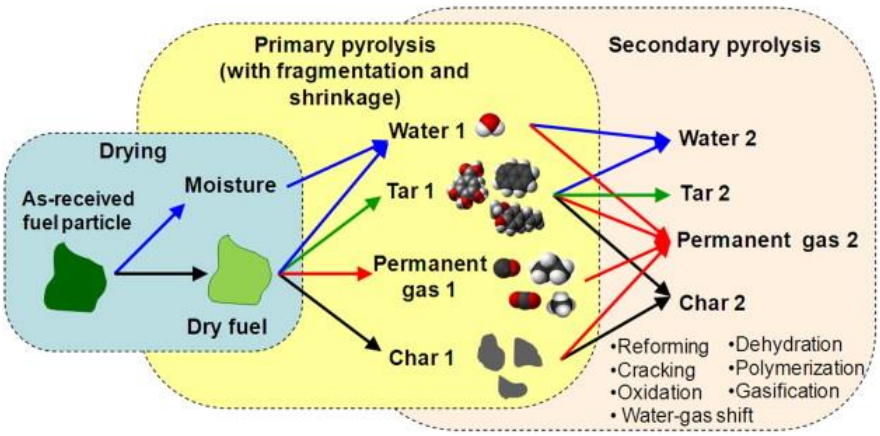

Figure 1.3 Thermal degradation of a solid biomass particle in inert atmosphere: drying, primary pyrolysis and secondary pyrolysis [1-12]

During the devolatilization, biomass (i.e., fuel) is thermally decomposed into a carbonaceous solid named char, while it releases volatiles, expressed in a simplified route by R1 in Table 1.2 and Fig. 1.4. The volatiles include the non-condensable gases, such as CO_2, H_2, CO, CH_4, H_2, and so on, condensable gases (tar) and water vapor (both from chemically bound and from the free water in the fuel). The devolatilization stage, chemical decomposition by heating in the absence of oxygen, is also termed as pyrolysis. During pyrolysis, volatile material is released from the fuel. This is a thermochemical process driven by the heating of the fuel and oxygen is supposed not to penetrate into the fuel particle, so the process proceeds in an atmosphere free of oxygen. This is due to the high release of volatiles from biomass fuels, which obstructs the transport of oxygen from the bulk fluidization agent to the interior of the fuel particle. However, oxygen may exist in the gas around the particle and can react with the volatiles, or it can react with a char particle after devolatilization. After the primary decomposition, various gas-gas and gas-solid reactions take place: secondary pyrolysis, during which the tar may be reformed (R12 and R13), oxidized (R11), and cracked (R15). The light hydrocarbons (e.g., CH_4, C2+) and other combustible gases (e.g., CO, H_2) may react with O_2 by reactions (R7-R9). The carbon in char can be burnt (R2 and R3) or gasified [reforming with CO_2, H_2O, and less with H_2, by reactions (R4-R6)], mainly depending on the oxygen concentration in the specific location of gasifier where the char is present.

Table 1.2 Main Thermochemical Reactions in Biomass Gasification

Stoichiometry		Heat of reaction (kJ/mol)	Name
Biomass → char + light gas (CO + H_2 + CO_2 + CH_4 + C_2 + N_2 + ...) + H_2O + tar	(R1)	Endothermic	Biomass devolatilization
C + 1/2O_2 → CO	(R2)	-111	Complete combustion
C + O_2 → CO_2	(R3)	-394	Partial combustion
C + CO_2 → 2CO	(R4)	+173	Boudouard combustion
C + H_2O → CO + H_2	(R5)	+131	Steam gasification
C + 2H_2 → CH_4	(R6)	-75	Hydrogen gasification
CO + 1/2O_2 → CO_2	(R7)	-283	Carbon monoxide oxidation
H_2 + 1/2O_2 → H_2O	(R8)	-242	Hydrogen oxidation
CH_4 + O_2 → CO_2 + 2H_2O	(R9)	-283	Methane oxidation
CO + H_2O → CO_2 + 2H_2	(R10)	-41	Water-gas-shift reaction
C_nH_m + (n/2)O_2 → nCO + (m/2)H_2	(R11)	Highly endothermic (200-300)	Partial oxidation
C_nH_m + $n$$CO_2$ → (2n)CO + (m/2)H_2	(R12)		Dry reforming
C_nH_m + $n$$H_2O$ → nCO + (m/2+n)H_2	(R13)		Steam reforming
C_nH_m + (2n-m/2)H_2 → $n$$CH_4$	(R14)		Hydrogen reforming
C_nH_m → (m/4)CH_4 + (n-m/4)C	(R15)		Thermal cracking

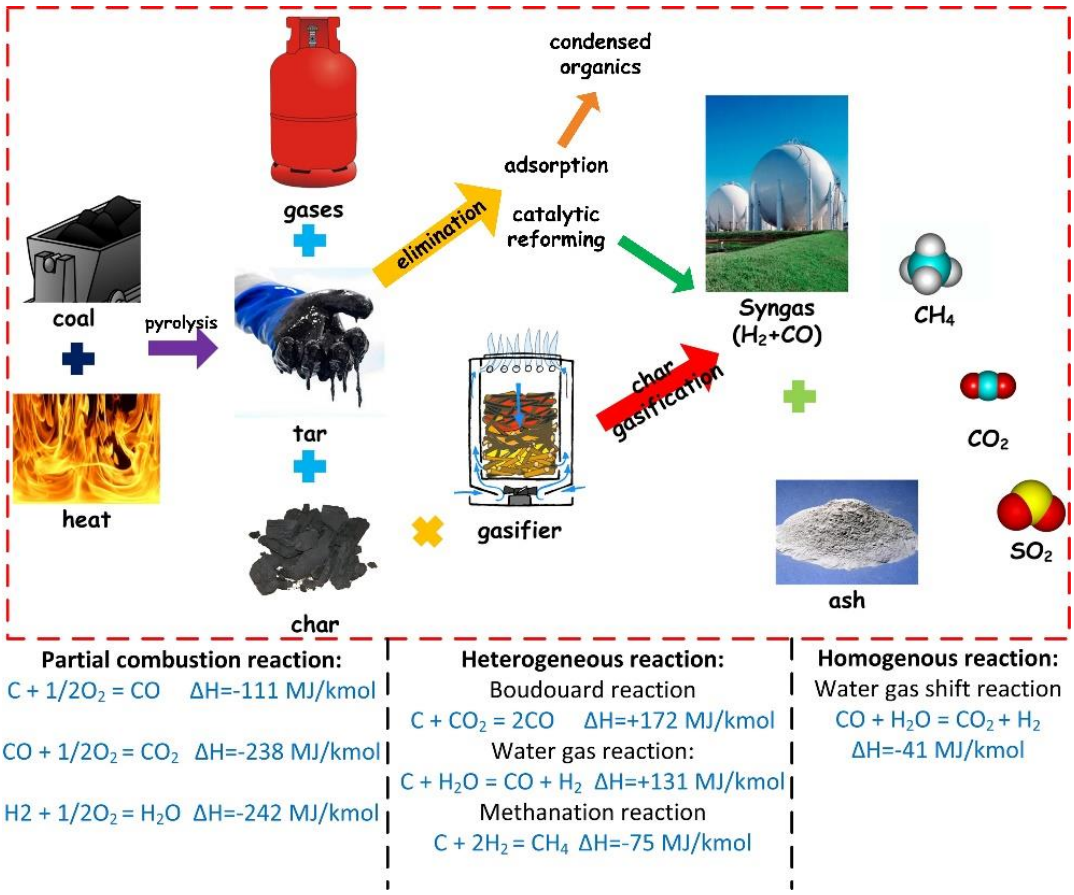

Figure 1.4 Main thermochemical reactions occurring in the coal or biomass gasification

1.3 Biomass Tar

In common, condensable aromatic organics (*e.g., polycyclic aromatic hydrocarbons*) referred to as "tar" are generated along with the producer gas during biomass gasification and their contents vary from 0.5-100 g/m^3 depending on the design of a gasifier, feedstock types, and operating conditions and so on [1-13]. Biomass tar is a generic term comprising all organic compounds in syngas except for gaseous hydrocarbons. Tars can condense or polymerize to more complex structures (e.g., coke) in pipes, filters, or heat exchangers of downstream equipment and processes, which may result in the mechanical breakdown of the entire system. Additionally, tars may deactivate catalysts in the refining process. Tar removal by the adsorption and reforming to syngas should be important and indispensable to commercialize this technology for applications in power generation and synthetic fuel production [1-14].

1.4 Tar Removal Methods

It is essential to reduce the level of tars to enable widespread utilization of syngas. Considerable efforts have been directed to tar removal from fuel gas. Broadly speaking, tar removal technologies could be divided into two approaches: gas downstream cleaning after the gasifier (secondary methods) and treatment inside the gasifier (primary methods). Fig. 1.5 illustrates the difference between the primary and the secondary methods. The primary methods include measures taken during the gasification process to prevent or convert tar formed in the gasifier. Secondary methods are measures to improve the hot product gas issuing from the gasifier. An ideal primary method concept can eliminate the requirement for the secondary treatment. The secondary methods have been studied widely and are well understood. In contrast, the primary methods have not yet been fully understood and are currently investigated a great deal.

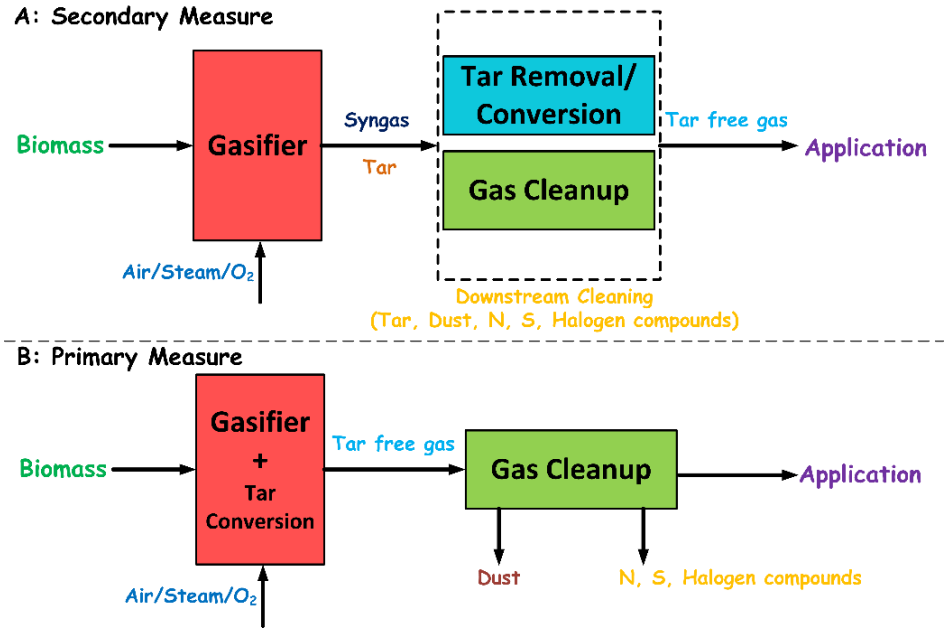

Figure 1.5 Comparison of primary and secondary measures for gas cleaning

1.4.1 Primary Methods

The primary methods include the selection of operating conditions, bed additives or catalysts in the gasifier, and the gasifier design. The operating conditions can play a crucial role during biomass

gasification process in many ways, such as the carbon conversion, the producer gas composition, the tar formation, and the tar reduction. The most significant influencing parameters are the temperature, the gas concentration, and the residence time. For a given gasifier design and biomass type, these variables are the result of setting the following variables: the air ratio (i.e., oxygen feed in relation to the stoichiometric), the composition of gasifying medium (flow rates of oxygen/steam in relation to the flow rate of biomass), and the addition of catalysts and additives. The key variable in gasification is the temperature. Fig. 1.6 summarizes the effect of the temperature in the gasifier on key variables (i.e., the heating value of the gas and tar and char conversion) and processes, such as the sintering, when gasifying different biomasses. The temperature range of 800-900 °C is normally employed in biomass gasification, considering the balance of the benefits and the drawbacks associated with the thermal level [1-13].

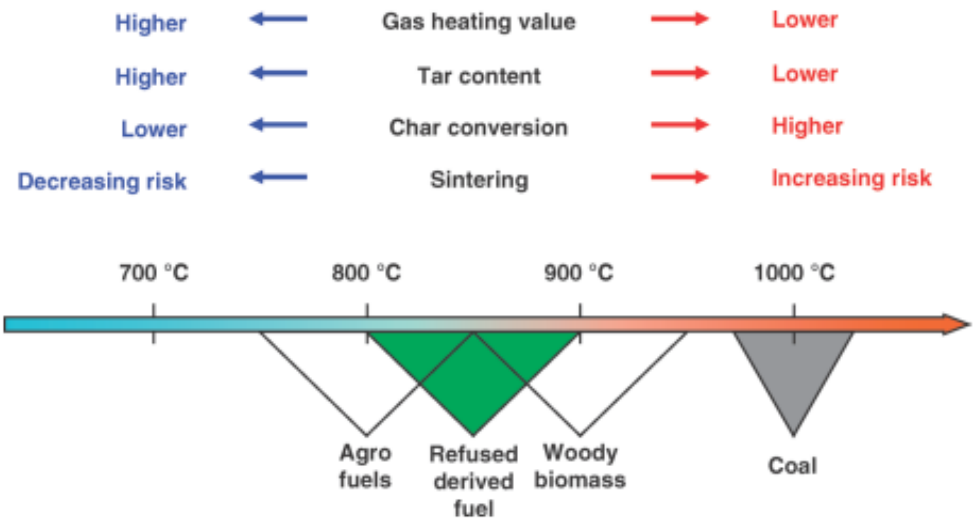

Figure 1.6 Effect of the temperature adjustment on parameters and processes during gasification of various fuels [1-13]

Addition of steam could enhance the reforming reaction of tar and char gasification, improving the gas quality and reducing the tar content. However, these reactions consume heat, which must be added to the reactor, for example, by addition of oxygen. If the oxygen is added by air, the gas is diluted with nitrogen and the heating value of the gas produced is reduced. If pure oxygen is used,

a better gas quality is achieved, but oxygen affects the economic feasibility of the gasification process. Therefore, the composition of the gasification agent must be assessed by appreciating the technical benefits and the economical drawbacks. In-bed additives in the fluidized-bed gasifiers have been also attracted much attention. Addition of catalysts, such as carbonate rocks (e.g., dolomite and limestone), olivine, and metal-based catalysts improve significantly the gas quality by reducing tar content. Nevertheless, loss of catalyst materials by entrainment, the inhibition caused by carbon and sulfur, or the contamination of the ashes greatly limits these options. Again, an economic evaluation of the process determines which technique is feasible in the practical use. The measure that yields the maximum reduction of tar in the bed is not necessarily the best: primary measures should be understood as a primary action in conjunction with secondary measures. The overall process should be optimized in terms of the technical reliability and the economy feasibility.

1.4.2 Secondary Methods

Secondary methods are conventionally used to treat with the hot product gas of the gasifier. The methods can be chemical or physical treatments. Secondary chemical methods are composed of tar cracking in the downstream of the gasifier, either thermally or catalytically. Secondary physical methods consist of the use of cyclones, filters of various types (baffle, ceramic, and fabric), rotating particle separators, electrostatic filters, and scrubbers. Removal of tars by means of condensation is, in principle, the least complicated way to remove tars. Various cooling methods have been applied in biomass gasification systems, including scrubbers, venturies, humidified packed beds, and so on. In the direct water-cooled tar-removal systems, some of the dust, HCl, sulfur oxides, and alkaline metals are removed by water (e.g., venturi scrubber). A significant drawback of the direct water-cooled systems is the downstream of wastewater contaminated by tar, which needs further treatment [1-13].

In methods based on scrubbing with water, an important factor to consider is the amount of soluble tars in the water stream, mainly phenols. Phenols are relatively easily destroyed at a relative high temperature in the gasifier. Properly linked primary measures with this secondary wet cleaning concept could be a sound technical solution for small- to medium-scale plants for power generation. Conversion of tar in the hot gas by thermal cracking/reforming is generally preferred, since the energetic value of tar remains in the gas phase, while it is decomposed into light fuel gases. Thermal cracking is only effective at relatively high temperatures, whilst a catalytic technique is more effective at the thermal level of the hot gas. However, the latter is more expensive and has some technical shortcomings, such as inactivation caused by carbon deposition. Some novel catalysts can overcome these disadvantages, but they still require much demonstration prior to the industrial implementation. Therefore, tar cracking systems have not been widely commercially available, but are under development. In summary, although some secondary gas cleaning methods are reported to be effective, they are usually not economically viable.

In our laboratory, some researchers have preliminary studied the tar removal by oil absorption and char materials adsorption as illustrated in Fig. 1.7 [1-15], [1-16], [1-17]. For instance, Paethanom *et al*. [1-18] combined an oil scrubber with the chestnut wood char adsorption bed from the lab-scale to pilot-scale facility of integrated pyrolysis regenerated plant. It showed that the optimum system needed for 0.045 m^3/h pyrolysis gas about 1 L of oil. The oil scrubber charged with 1 L of vegetable oil was combined with a 41 g of chestnut wood pyrolysis char adsorption bed and reached 97.6% of the gravimetric tar removal. It is noted that the service life, detailed mechanism and kinetics of various tar compounds adsorption on chars are unclear and needed to be further studied. Biochars derived from the pyrolysis and carbonization of biomass normally contain many nitrogen or oxygen functional groups such as -NH_2/-OH, C-O, C=O, etc (Fig. 1.6A). Firstly, -NH_2 on the char surface is one kind of basic functional groups, while phenol is a Lewis acid, accordingly, phenol is prone to

combine with -NH_2 through the acid-base interaction. Secondly, -OH, C-O and C=O groups could interact with phenol via hydrogen bond. Additionally, the strong electron-donating ability of the hydroxyl group can cause the aromatic ring of phenol to be a π-electron rich system (Fig. 1.6B). Thereby, the aromatic rings of different phenol molecules can easily form π-π* stacking interactions to provide a multilayer adsorption system. Compared to the *Van der Waals* force, which is the primary driving force in adsorption of activated carbon, the chemical interactions between the functional groups and phenol molecule are more effective to enhance the adsorption [1-19].

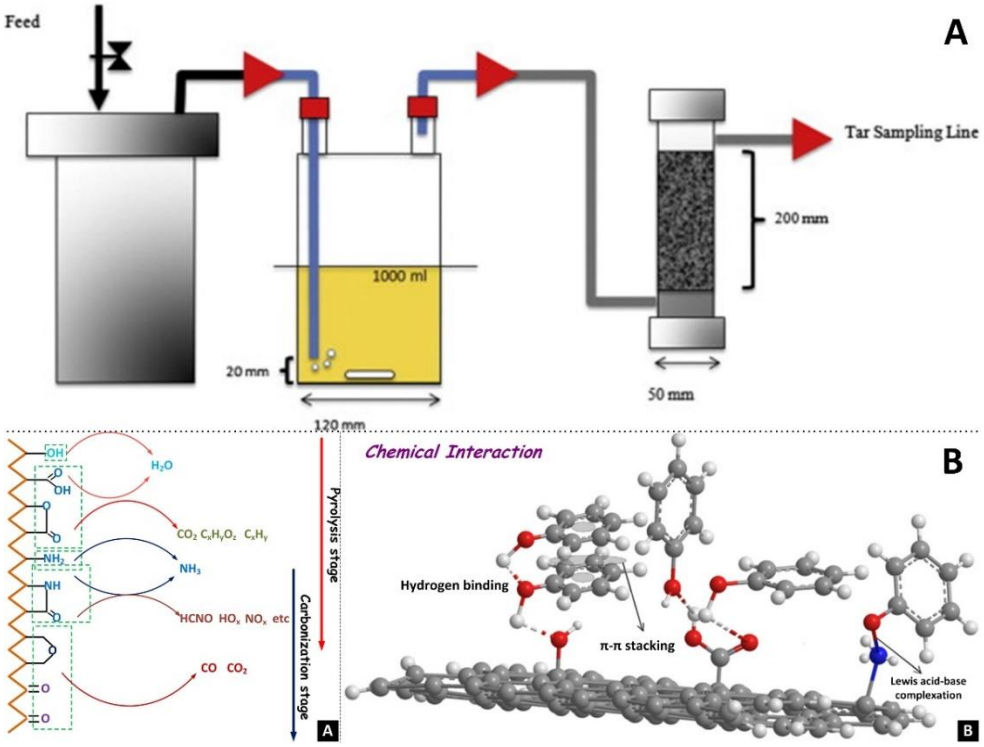

Figure 1.7 Tar removals by oil absorption (A) and char adsorption (B)

1.5 Catalytic Conversion

Several approaches for tar elimination in the primary or secondary treatment, such as physical treatment [1-15], [1-16], [1-17], [1-18], thermal cracking [1-20], plasma-assisted cracking [1-21], and catalytic reforming [1-22], [1-23], [1-24], [1-25], [1-26], have been extensively employed. Physical treatment such as adsorption and absorption is a sustainable and feasible method for tar removal. Moreover, physical processes used for tar removal are uncomplicated adaptable to any

gasification system. However, it always depends on gas quality specifications required for specific downstream applications. In general, char adsorption could adsorb the light tar compounds, while the heavy tar is normally eliminated by chemical methods, such as the catalytic and non-catalytic thermochemical conversion. Among these, the catalytic conversion has been considered to be one of the most promising in the large-scale applications due to its fast reaction rate and reliability [1-26] and its ability to transform tar into high-value added gases such as CO and H_2 in the presence or absence of steam. Various types of catalysts such as calcined rocks [1-27], zeolites [1-28], iron ores [1-29], alkali metals [1-30], nickel-based catalysts [1-31], [1-32], and noble metals catalysts [1-33], [1-34], [1-35], [1-36], [1-37] have been developed for their usefulness on tar reforming in biomass gasification. With regards to the catalytic reactivity and economic reasons, nickel-based catalysts are considered to be the most promising for tar removal and gas upgrading [1-38], [1-39], [1-40], [1-41], [1-42], [1-43], [1-44]. Nickel-based catalysts are commonly supported by natural materials (*e.g., dolomite, olivine, charcoal and palygorskite*) (as shown in Fig. 1.8) or metal oxides (*e.g., Al_2O_3 and MgO*) (as shown in Fig. 1.9) [1-45], [1-46], [1-47], [1-48], [1-49], [1-50], [1-51]. Additionally, Table 1.3 summarizes the advantages and disdvantages of different catalysts used for tar elimination [1-52]. These catalyst supports are relative expensive and unsustainable. Besides, the catalyst preparation steps are time and energy consuming. Therefore, these factors would limit the extensive applications of nickel-based catalysts. As an alternative, the by-product of char has been studied to be a sustainable catalyst with fair performance in tar removal [1-53], [1-54], [1-55], [1-56] and an excellent carbonaceous adsorbent [1-57]. The char-supported catalysts with low cost could be simply gasified to recover the energy of char without the need of frequent regeneration after deactivation. However, char could also be consumed due to the participation of gasification reactions and its properties are not fixed mainly depending on the biomass types and the process conditions.

Table 1.3 Summary of Catalysts Advantages and Disdvantages [1-52]

Catalyst	Advantage	Disadvantage
calcined rocks	1. inexpensive and abundant; 2. attain high tar conversion ~95% conversion with dolomite; 3. often used as guard beds for expensive catalysts most popular for tar elimination	fragile materials and quickly eroded from fluidized beds
olivine	1. inexpensive; 2. high attrition resistance	lower catalytic activity than dolomite
clay minerals	1. inexpensive and abundant; 2. fewer disposal problems	1. lower catalytic activity than dolomite; 2. most natural clays do not support the high temperatures (800-850 °C) needed for tar elimination (lose pore structure)
iron ores	inexpensive and abundant	1. rapidly deactivated in the absence of hydrogen; 2. lower catalytic activity than dolomite
char	1. inexpensive and abundant; 2. sustainable (natural production inside the gasifier); 3. high tar conversion compared to dolomite; 4. neutral or weak base properties	1. consumption because of gasification reactions; 2. its properties are not fixed depending on biomass type and process conditions
fluid cracking catalysts (FCC)	1. relatively inexpensive but not cheaper than the above; 2. more known about it from experience with FCC units	1. rapid deactivation by coke; 2. lower catalytic activity than dolomite
alkali-metal-based	1. natural production in the gasifier; 2. reduce ash-handling problems	1. particle agglomeration at high temperatures; 2. lower catalytic activity than dolomite
activated alumina	high tar conversion comparable to that of	rapid deactivation by coke

	dolomite	
transition-metal-based	1. able to attain complete tar elimination at ~900 °C; 2. increase the yield of CO_2 and H_2; 3. higher tar reforming activity (Ni-based catalysts are 8-10 times more active than dolomite)	1. rapid deactivation because of sulfur and high tar content in the feed; 2. relatively expensive; 3. relatively easier regenerated

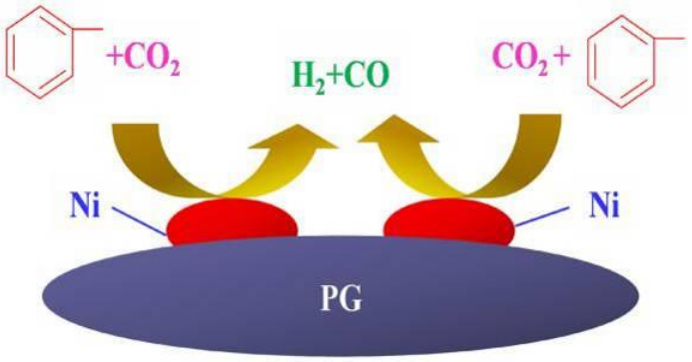

Figure 1.8 Dry reforming of tar compounds over the palygorskite (PG) supported Ni catalyst [1-51]

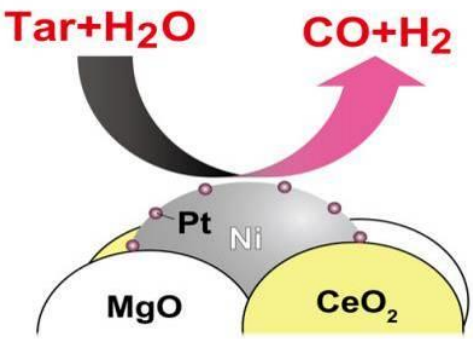

Figure 1.9 Steam reforming of tar compounds over the metal oxides supported Ni catalyst [1-32]

Fig. 1.10 shows the schematic diagram of the interaction among char, vapor and tar during biomass pyrolysis. On one hand, carbon derived from char can interact in a wide range of pyrolysis reactions. On the other hand, carbon derived from char can interact at the later stage of pyrolysis reactions. The attractiveness of biochars as catalysts originates from low cost and natural production inside the gasifier. However, it could be consumed by steam or CO_2 in the producer gas. The requirement

for a continuous external char supply or withdrawal most likely depends on the balance of biochars production and consumption in the gasification system. Interestingly, biochars showed a good catalytic performance for tar conversion as well.

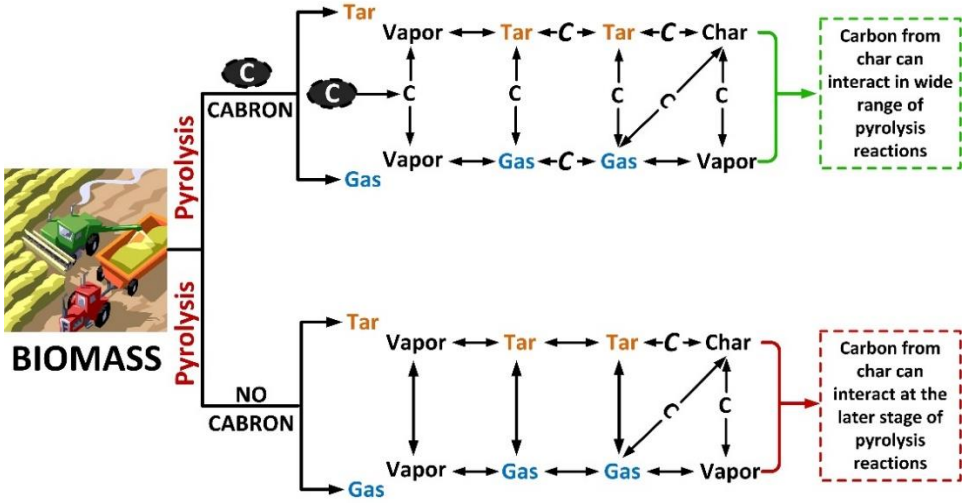

Figure 1.10 Schematic diagram of the interaction among char, vapor and tar during biomass pyrolysis

Z. Abu El-Rub [1-53] comparatively studied the biomass char and other catalysts for tar model compounds reduction. As shown in Fig. 1.11A, dolomite and nickel catalyst showed the highest phenol conversion efficiencies at 700 °C (90 and 91 wt.%, respectively). However, the commercial biomass char (C.B. char) showed a moderate phenol conversion (82 wt.%). Since the heterocyclic tars (e.g., phenol) at a gasification temperature of 800 °C or above are thermally cracked, only a small amount of the heterocyclic tars (e.g., phenol) remains in the producer gas to be reformed catalytically. Naphthalene is a major tar compound at 900 °C. In summary, the catalytic reactivity obtained at 40 g/Nm^3 is followed by the order of commercial nickel > dolomite > olivine > silica sand. The relative low reactivity of the dolomite can be attributed to the low iron content. The activity of olivine can be improved by a pre-treatment to make the iron active present on the surface of olivine. The ranking of catalytic activity is obtained: C.B. char > biomass char > ash > fluid cracking catalyst (FCC) (Fig. 1.11B).

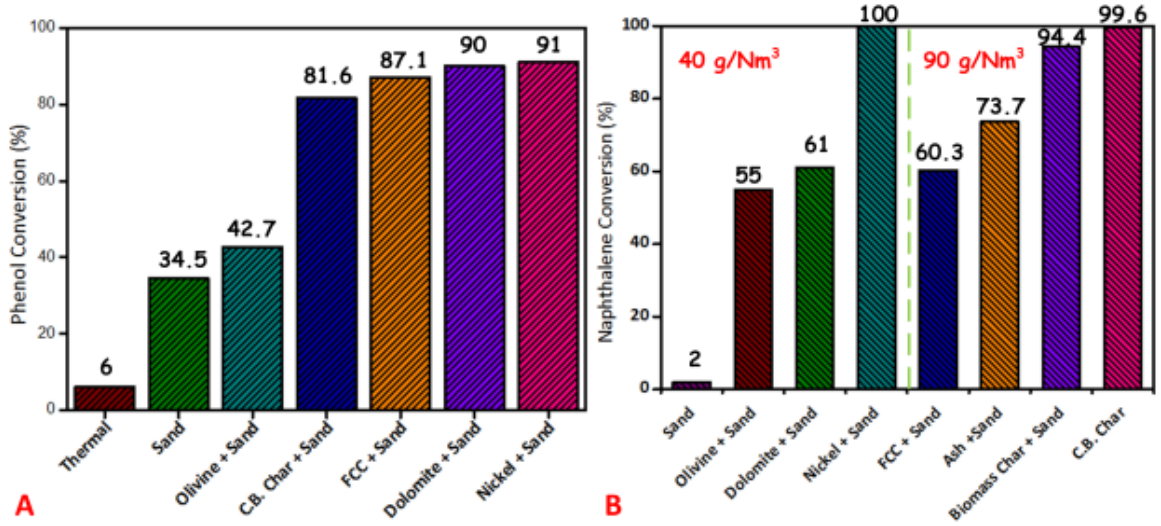

Figure 1.11 (A) Effect of catalysts on phenol conversion. T = 700 °C, τ = 0.3 s, feed gas composition: 6 vol.% CO_2, 10 vol.% H_2O and balance N_2, inlet phenol concentration: 8-12 g/Nm^3; (B) Naphthalene conversion T = 900 °C, initial naphthalene concentration: 40 g/Nm^3 and 90 g/Nm^3 (other conditions are the same as phenol conversion). [1-53]

1.6 Rice Husk to Energy and Materials

In general, the catalytic performance of char on tar conversion depends on gasification/pyrolysis conditions, catalytic conditions, gasifier types, tar composition and biomass sources, etc. With the increase of requirement and the development of technologies, the production and consumption of rice has been increasing year by year. Consequently, large amounts of rice husk and rice straw can be produced. According to recent estimations, the global production of rice is around 685 million tons (including rice, straw and husk), and rice husk means between 0.2 and 0.33 kg per kg of rice harvested [1-58]. Rice husk is always burnt in open fields, and this practice normally involves energy waste. Moreover, it causes a serious environmental problem. These abundant agricultural biomass wastes can be directly burnt out for heating applications. Additionally, they could be gasified into the syngas for power generation (as illustrated in Fig. 1.12) or chemicals synthesis. In downstream systems, the high quality syngas, in terms of low-tar content and high heating value, is particularly required.

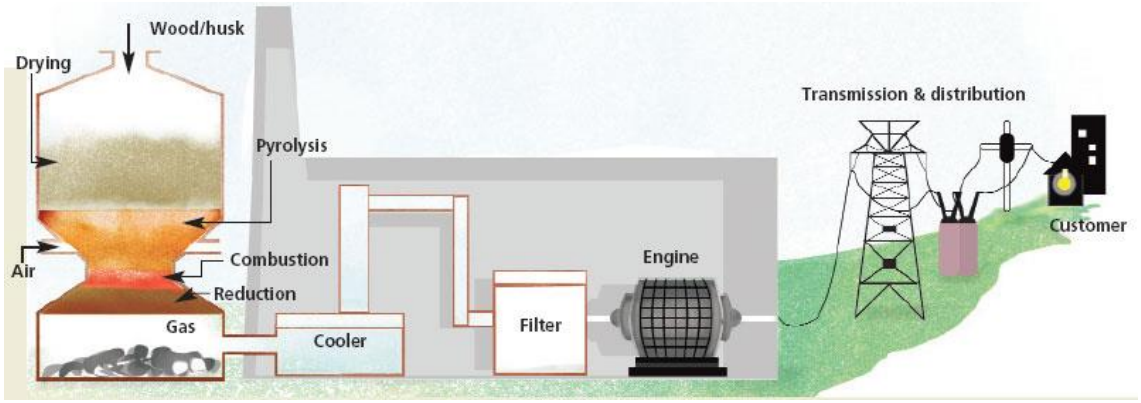

Figure 1.12 Schematic diagram of power generation from husk and wood gasification (*http://www.downtoearth.org.in/content/powered-husk*)

As a special biomass source, the volatile matters of rice husk was about 60 wt.% lower than some other biomass species (e.g., grass, up to 95%) because of higher ash content (17-26 wt.%) mainly in the form of inorganic matters (e.g., amorphous silica) [1-59]. Consequently, the by-product of char derived from rice husk pyrolysis has a potential to be made into the high value-added carbon and silicon materials. As shown in Fig. 1.13, after pyrolysis at 400-900 ^{o}C, the synthesis gas, char and oil can be produced from rice husk. Because of high content of silica and carbon, rice husk char or ash could be recycled for the fabrication of silica-based materials, carbonaceous adsorbents and catalyst supports. It should be noted that the char catalytic performance mainly depends on the pyrolysis conditions, gasifier types, tar composition and biomass sources, etc. So far, rice husk char derived from rice husk pyrolysis has never been studied as a catalyst support for tar conversion and syngas upgrading.

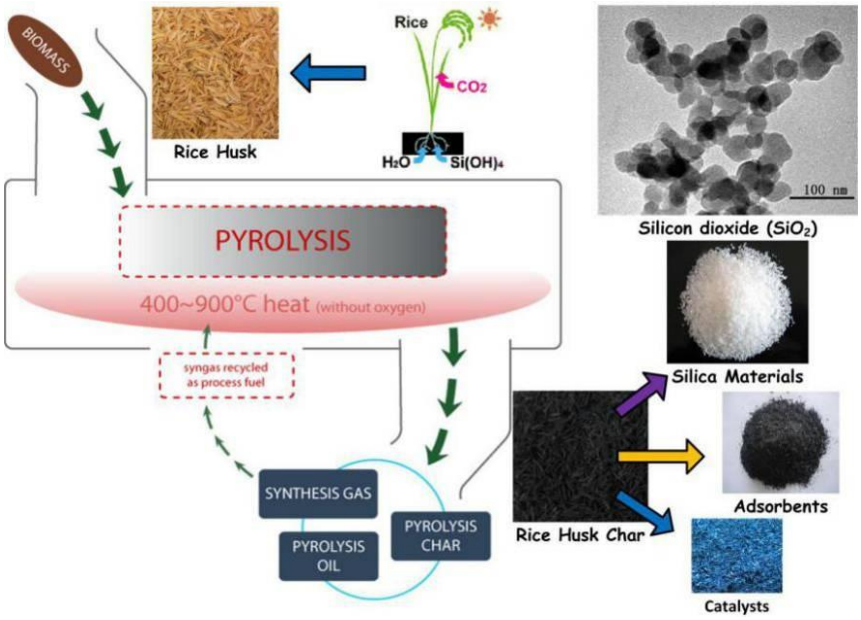

Figure 1.13 Schematic diagram of rice husk to energy and materials via pyrolysis

1.7 Objective and Structure of This Thesis

The main objective of this study is to develop a sustainable rice husk ash or char supported nickel catalyst for tar conversion during high temperature pyrolysis/gasification of biomass. In this work, rice husk could be used as porous silica and carbon precursor. And metal nickel organic coordination complex (R-Ni) is employed as a catalyst precursor. Preliminarily, rice husk char or ash supported iron or nickel catalysts would be comparatively studied for tar *in situ* reduction via co-pyrolysis with biomass (i.e., rice husk) at a high temperature (800 °C). After that, the metal nickel nanoparticles could be generated in the carbon matrix of rice husk char via one-step pyrolysis, which is further studied for tar catalytic conversion, including *in situ* and *ex situ*. The structure is shown in Fig. 1.14.

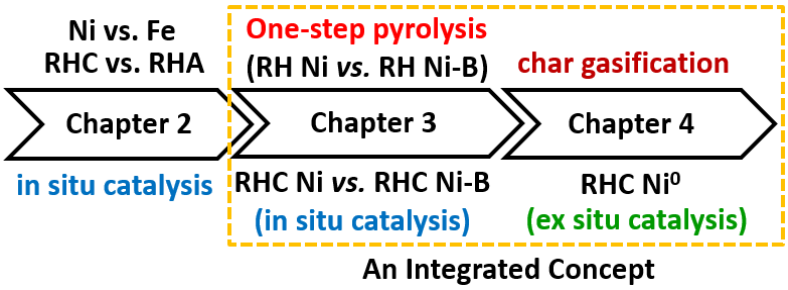

Figure 1.14 Simplified structure of the thesis

The contents of doctor thesis have been divided into five chapters as follows:

1. Introduction
2. In situ catalytic conversion of tar using rice husk char or ash supported nickel-iron catalysts for biomass gasification combined with the mixing-simulation in the fluidized-bed gasifier
3. Nickel nanoparticles generated in the carbon matrix of rice husk char for *in situ* catalytic conversion of tar derived from biomass pyrolysis
4. Ex situ catalytic conversion of tar and syngas over the metallic nickel nanoparticles embedded in the carbon matrix of rice husk char for biomass gasification
5. Conclusions & recommendations

References

[1-1] F.L. Chan, A. Tanksale, Review of recent developments in Ni-based catalysts for biomass gasification. *Renewable & Sustainable Energy Reviews* 2014, 38, 428-438.

[1-2] J.A. Ruiz, M.C. Juárez, M.P. Morales, P. Muñoz, M.A. Mendívil, Biomass gasification for electricity generation: Review of current technology barriers. *Renewable & Sustainable Energy Reviews* 2013, 18, 174-183.

[1-3] P. Basu, *Gasification theory and modeling of gasifiers.* In: Biomass Gasification Design Handbook. Boston: Academic Press; 117-165.

[1-4] W. Torres, S.S. Pansare, Jr J.G. Goowin, Hot gas removal of tars, ammonia, and hydrogen sulfide from biomass gasification gas. *Catalysis Reviews* 2007, 49, 407-456.

[1-5] G.J. Stiegel, R.C. Maxwell, Gasification technologies: the path to clean, affordable energy in the 21st century. *Fuel Processing Technology* 2001, 71, 79-97.

[1-6] I.I. Ahmed, N. Nipattummakul, A.K. Gupta, Characteristics of syngas from cogasification of polyethylene and woodchips. *Applied Energy* 2011, 88, 165-174.

[1-7] I.I. Ahmed, A.K. Gupta, Evolution of syngas from cardboard gasification. *Applied Energy* 2009, 86, 1732-1740.

[1-8] A.V. Bridgwater, The technical and economic feasibility of biomass gasification for power generation. *Fuel* 1995, 74, 631-653.

[1-9] J. Han, H. Kim, The reduction and control technology of tar during biomass gasification/pyrolysis: an overview. *Renewable & Sustainable Energy Reviews* 2008, 12, 397-416.

[1-10] D. Mohan, C.U. Pittman, P.H. Steele, Pyrolysis of wood/biomass for bio-oil: a critical review. *Energy & Fuels* 2006, 20, 848-889.

[1-11] C. Di Blasi, Modeling chemical and physical processes of wood and biomass pyrolysis. *Progress in Energy and Combustion Science* 2008, 34, 47-90.

[1-12] D. Neves, H. Thunman, A. Matos, L. Tarelho, A.G. Barea, Characterization and prediction of biomass pyrolysis products. *Progress in Energy and Combustion Science* 2011, 37, 611-630.

[1-13] A. Gómez-Barea and B. Leckner, *Gasification of Biomass and Waste.* Wiley: Handbook of combustion 2010, 5, 365-399.

[1-14] G.Q. Guan, G. Chen, Y. Kasai, E.W.C. Lim, X.G. Hao, M. Kaewpanha, A. Abuliti, C. Fushimi, A. Tsutsumi, Catalytic steam reforming of biomass tar over iron- or nickel-based catalyst supported on calcined scallop shell. *Applied Catalysis B: Environmental* 2012, 115-116, 159-168.

[1-15] T. Phuphuakrat, T. Namioka, K. Yoshikawa, Tar removal from biomass pyrolysis gas in two-step function of decomposition and adsorption. *Applied Energy* 2010, 87, 2203-2211.

[1-16] A. Paethanom, S. Nakahara, M. Kobayashi, P. Prawisudha, K. Yoshikawa, Performance of tar removal by absorption and adsorption for biomass gasification. *Fuel Processing Technology* 2012, 104, 144-154.

[1-17] P. Hasler, T. Nussbaumer, Gas cleaning for IC engine applications from fixed bed biomass gasification. *Biomass Bioenergy*1999, 16, 385-395.

[1-18] A. Paethanom, P. Bartocci, B.D. Amico, F. Testarmata, N. Moriconi, K. Slopiecka, K. Yoshikawa, A low-cost pyrogas cleaning system for power generation: Scalling up from lab to pilot. *Applied Energy* 2013, 111, 1080-1088.

[1-19] W.J. Liu, F.X. Zeng, H. Jiang, X.S. Zhang, Preparation of high adsorption capacity bio-chars from waste biomass. *Bioresources Technology* 2011, 102, 8247-8252.

[1-20] L. Fagbemi, L. Khezami, R. Capart, Pyrolysis products from different biomasses: application to the thermal cracking of tars. *Applied Energy* 2001, 69, 293-306.

[1-21] S.A. Nair, A.J.M. Pemen, K. Yan, E.J.M. Van Heesch, K.J. Ptasinski, A.A.H. Drinkenburg, Chemical processes in tar removal from biomass derived fuel gas by pulsed corona discharges. *Plasma Chemistry Plasma Processing* 2003, 23, 665-680.

[1-22] E.G. Baker, L.K. Mudge, Mechanisms of catalytic biomass gasification. *Journal of Analytical and Applied Pyrolysis* 1984, 6, 285-297.

[1-23] D. Wang, W. Yuan, W. Ji, Use of biomass hydrothermal conversion char as the Ni catalyst support in benzene and gasification tar removal. *Transaction of the ASABE* 2010, 53, 795-800.

[1-24] Z. Abu El-Rub, E. A. Bramer, and G. Brem, Review of catalysts for tar elimination in biomass gasification processes. *Industrial & Engineering Chemistry Research* 2004, *43,* 6911-6919.

[1-25] Y. Shen, K. Yoshikawa, Recent progresses in catalytic tar elimination during biomass gasification or pyrolysis – A Review. *Renewable & Sustainable Energy Reviews* 2013, 21, 371-392.

[1-26] G.W. Huber, S. Iborra, A. Corma, Synthesis of transportation fuels from biomass: chemistry, catalysts, and engineering. *Chemical Reviews* 2006, 106, 4044-4098.

[1-27] Q.Z. Yu, C. Brage, T. Nordgreen, K. Sjöström, Effects of Chinese dolomites on tar cracking in gasification of birch. *Fuel* 2009, 88, 1922-1926.

[1-28] B. Dou, J. Gao, X. Sha, S.W. Baek, Catalytic cracking of tar component from high temperature fuel gas. *Applied Thermal Engineering* 2003, 23, 2229-2239.

[1-29] S.S. Tamhankar, K. Tsuchiya, J.B. Riggs, Catalytic cracking of benzene on iron oxide-silica: catalyst activity and reaction mechanism. *Applied Catalysis* 1985, 16, 103-121.

[1-30] T. Suzuki, H. Ohme, Y. Watanabe, Alkali metal catalyzed carbon dioxide gasification of carbon. *Energy & Fuels* 1992, 6, 343-351.

[1-31] M. He, B. Xiao, Z. Hu, S. Liu, X. Guo, S. Luo, Syngas production from catalytic gasification of waste polyethylene: influence of temperature on gas yield and composition. *International Journal of Hydrogen Energy* 2009, 34, 1342-1348.

[1-32] D. Li, Y. Nakagawa, K. Tomishige, Development of Ni-based catalysts for steam reforming of tar derived from biomass pyrolysis. *Chinese Journal of Catalysis* 2012, 33, 583-594.

[1-33] T. Furusawa, A. Tsutsumi, Comparison of Co/MgO and Ni/MgO catalysts for the steam reforming of naphthalene as a model compound of tar derived from biomass gasification. *Applied Catalysis A: General* 2005, 278, 207-212.

[1-34] S.J. Juutilainen, P.A. Simell, A.O. Krause, Zirconia: Selective oxidation catalyst for removal tar and ammonia from biomass gasification gas. *Applied Catalysis B: Environmental* 2006, 1-2, 86-92.

[1-35] D.A. Constantinou, M.C. Álvarez-Galván, J.L.G. Fierro, A.M. Efstathiou, Low-temperature conversion of phenol into CO, CO_2 and H_2 by steam reforming over La-containing supported Rh catalysts. *Applied Catalysis B: Environmental* 2012, 117-118, 81-95.

[1-36] S. Cheah, K.R. Gaston, Y.O. Parent, M.W. Jarvis, T.B. Vinzant, K.M. Smith, N.E. Thornburg, M.R. Nimlos, K.A. Magrini-Bair, Nickel cerium olivine catalyst for catalytic gasification of biomass. *Applied Catalysis B: Environmental* 2013, 134-135, 34-45.

[1-37] P. Azadi, E. Afif, H. Foroughi, T. Dai, F. Azadi, R. Farnood, Catalytic Reforming of Activated Sludge Model Compounds in Supercritical Water Using Nickel and Ruthenium Catalysts. *Applied Catalysis B: Environmental* 2013, 134-135, 265-273.

[1-38] H. Zhao, K.J. Draelants, G.V. Baron, Performance of a nickel-activated candle filter for naphthalene cracking in synthetic biomass gasification gas. *Industrial & Engineering Chemistry Research* 2000, 39, 3195-3201.

[1-39] D.N. Bangala, N. Abatzoglou, E. Chornet, Steam reforming of naphthalene on Ni-Cr/Al_2O_3 catalysts doped with MgO, TiO_2, and La_2O_3. *AIChE Journal* 1998, 44, 927-936.

[1-40] C.M. Kinoshita, Y. Wang, J. Zhou, Effect of reformer conditions on catalytic reforming of biomass-gasification tars. *Industrial & Engineering Chemistry Research* 1995, 34, 2949-2954.

[1-41] J. Corella, A. Orío, J. Toledo, Biomass gasification with air in a fluidized bed: exhaustive tar elimination with commercial steam reforming catalysts. *Energy Fuels* 1999, 13(3), 702-709.

[1-42] P.H. Blanco, C. Wu, J.A. Onwudili, P.T. Williams, Characterization and evaluation of Ni/SiO_2 catalysts for hydrogen production and tar reduction from catalytic steam pyrolysis-reforming of RDF. *Applied Catalysis B: Environmental* 2013, 134-135, 238-250.

[1-43] C. Li, D. Hirabayashi, K. Suzuki, A crucial role of O_2^- and O_2^{2-} on mayenite structure for biomass tar steam reforming over Ni/$Ca_{12}Al_{14}O_{33}$. *Applied Catalysis B: Environmental* 2009, 3-4, 351-360.

[1-44] T. Kimura, T. Miyazawa, J. Nishikawa, S. Kado, K. Okumura, T. Miyao, S. Naito, K. Kunimori, K. Tomishige, Development of Ni catalysts for tar removal by steam gasification of biomass. *Applied*

Catalysis B: Environmental 2006, 3-4, 160-170.

[1-45] F. Pompeo, N.N. Nichio, O.A. Ferretti, D. Resasco, Study of Ni catalysts on different supports to obtain synthesis gas. *International Journal of Hydrogen Energy* 2005, 30, 1399-1405.

[1-46] V.R. Choudhary, A.S. Mamman, Energy efficient conversion of methane to syngas over NiO-MgO solid solution. *Applied Energy* 2000, 66, 161-175.

[1-47] T.J. Wang, J. Chang, C.Z. Wu, Y. Fu, Y. Chen, The steam reforming of naphthalene over a nickel-dolomite cracking catalyst. *Biomass Bioenergy* 2005, 28, 508-514.

[1-48] C. Courson, L. Udron, D.W. Ski, C. Petit, A. Kiennemann, Hydrogen production from biomass gasification on nickel catalysts: tests for dry reforming of methane. *Catalysis Today* 2002, 76, 75-86.

[1-49] I.G. Lee, S.K. Ihm, Catalytic gasification of glucose over Ni/activated charcoal in supercritical water. *Industrial & Engineering Chemistry Research* 2009, 48, 1435-1442.

[1-50] D.D. Le, X. Xiao, K. Morishita, T. Takarada, Biomass gasification using nickel loaded brown coal char in fluidized bed gasifier at relatively low temperature. *Journal of Chemical Engineering of Japan* 2009, 42, 51-57.

[1-51] T. Chen, H. Liu, P. Shi, D. Chen, L. Song, H. He, R.L. Frost, CO_2 reforming of toluene as model compound of biomass tar on Ni/Palygorskite. *Fuel* 2013, 107, 699-705.

[1-52] Z. Abu El-Rub, E.A. Bramer, G. Brem, Review of catalysts for tar elimination in biomass gasification. *Industrial & Engineering Chemistry Research* 2004, 43, 6911-6919.

[1-53] Z. Abu El-Rub, E.A. Bramer, G. Brem, Experimental comparison of biomass chars with other catalysts for tar reduction. *Fuel* 2008, 87, 2243-2252.

[1-54] Z. Abu El-Rub, E.A. Bramer, G. Brem, Tar reduction in biomass gasification using biomass char as a catalyst. In: Proceeding of conference and technology exhibition on biomass for energy, industry and climate protection, Rome, Italy; 2004. p. 1046-1049.

[1-55] Z. Abu El-Rub, Biomass char as an in-situ catalyst for tar removal in gasification systems. PhD dissertation, Enschede: University of Twente; 2008.

[1-56] P. Gilbert, C. Ryu, V. Sharific, J. Swithenbank, Tar reduction in pyrolysis vapours from biomass over a hot char bed. *Bioresources Technology* 2009, 100, 6045-6051.

[1-57] C. Danny, K. Ko, J.F. Porter, G. McKay, Optimised correlations for the fixed-bed adsorption of metal ions on bone char. *Chemical Engineering Science* 1999, 55, 5819-5829.

[1-58] J.S. Lim, Z. Abdul Manan, S.R. Wan Alwi, H. Hashim, A review on utilization of biomass from rice industry as a source of renewable energy. *Renewable & Sustainable Energy Reviews* 2012, 16, 3084-3094.

[1-59] D. Pottmaier, M. Costa, T. Farrow, A.A.M. Oliveira, O. Alarcon, C. Snap, Comparison of rice husk and wheat straw: from slow and fast pyrolysis to char combustion. *Energy & Fuels* 2013, 27, 7115-7125.

Chapter 2

In Situ Catalytic Conversion of Tar Using the Rice Husk Char or Ash Supported Nickel-Iron Catalysts for Biomass Gasification Combined with the Mixing-simulation in the Fluidized-bed Gasifier

2.1 Introduction

Physical treatment such as adsorption and absorption is a sustainable and feasible method for tar removal. Moreover, the physical processes for tar removal are uncomplicated and adaptable to any gasification system. However, it depends on the gas quality specifications required for the specific downstream applications as well. In general, char adsorption could adsorb the light tar compounds, while heavy tar is widely removed by chemical methods, such as catalytic and non-catalytic thermal conversion. Metals such as iron present in the char most likely play an important role in catalytic reactivity. The further research work will test the char catalytic performance for tar decomposition. In addition, the chemical properties of char should be modified to improve its catalytic performance. Recently, Li et al. [2-1], [2-2], [2-3] have engaged on the char and the char-supported catalysts for the tar reforming. The tar yields always decreased with the increase of the temperature due to the enhanced thermal cracking or catalytic reforming. However, the tar yields after pyrolysis were similar to those after steam reforming without catalysts at lower temperatures. The external steam has very weak influences on the thermal cracking of tar due to a low reactivity at a relative low temperature [2-4], [2-5]. The use of the char-supported iron catalyst can reach about 84% and 96% tar reduction at 800 and 850 °C, respectively. Furthermore, the tar yields after the steam reforming with the char-supported nickel catalyst were lower than those after the steam reforming with the

char-supported iron catalyst, especially at a low temperature. It is clearly shown that nickel has a higher activity for the tar reforming than iron even at the temperature as low as 500 °C [2-6], [2-7]. During catalytic reforming of tar, the char-supported catalyst could undergo significant changes, including the gasification of char by the gasifying agents intended to reform tar. Furthermore, the char-supported catalyst will be in constant contact with and thus interact with the volatiles (i.e., tar) being reformed. It is also known that the volatile-char interactions can cause significant changes to the char structure and substantial volatilization of alkali and alkaline earth metallic species from the solid, which are most likely to change the catalyst activity [2-8], [2-9]. In addition, the interactions of volatiles and char could cause volatile components to form soot on the surface of char [2-10], influencing the char reactivity as well. Therefore, the changes in the char reactivity are significant considerations for the disposal of spent catalyst via gasification or combustion.

Although iron exhibited a promising catalytic performance on the tar conversion at relative high temperatures, nickel as a catalyst have been widely used in the tar reforming [2-11], [2-12]. The reason is that nickel-based catalysts can get a higher tar reforming efficiency at a relative lower temperature. Carbon/coke formation is usually regarded as one main problem for the deactivation of nickel-based catalysts [2-13]. Wang *et al*. [2-14] studied the tar reforming over the char and char-supported nickel catalysts, which are prepared by mechanically mixing NiO with the char particles. Nickel was distributed more uniformly on the surface of the coal char than on the wood char. It could be ascribed to the porous surface structure of the coal char, which enhanced the adhesion of NiO particles. The wood char had relatively smooth and less porous surfaces that did not allow the easy deposition of Ni particles. Significantly, physical and chemical properties (e.g., porosity and metallic contents) of chars are highly dependent on their origins and production methods [2-15], [2-16]. Consequently, the nickel distributions on the char support and tar removal performance are expected to vary with different char types, including coal char, wood char. In this chapter, *in-situ*

catalytic conversion of tar is investigated via co-pyrolysis of biomass with the rice husk char (RHC) supported iron or nickel catalysts at a high temperature.

2.2 Experimental

2.2.1 Biomass and Char Characterization

Biomass feedstock of RH was collected from Thailand. The as-received RH was dried in an oven at 105 ^{o}C overnight. After that, the dry-based RH was devolatilized by pyrolysis at 700 ^{o}C for 30 min for rice husk char (RHC) production. Furthermore, the rice husk ash (RHA) was obtained by burning the as-prepared RHC in a muffle furnace under the air for 1 h. Table 2.1 presents the properties of RH, RHC and RHA including the ultimate and the proximate analyses, which were conducted by the elemental analyzer (*EA*, *Vario MICRO Cube, Elementar, Germany*) and the thermogravimetric analyzer (TGA, DTG-50, *SHIMADZU, Japan*), respectively. In addition, the chemical composition of RHA was determined by the X-ray fluorescence (*XRF, SHIMADZU, Rayny EDX 700, Japan*). It is found that RHA contains amounts of SiO_2, up to 94.64%, and a small quantity of minerals, such as alkali or earth alkali metal oxides. If RHC or RHA is employed as a catalyst support, it is necessary to load metal species (e.g., Ni, Fe) with the objective of improving the catalytic performances. Besides, the BET surface area of RHC was larger than those of RH and RHA. It indicates that RHC is considerable to be used as a support for catalysts preparation.

Table 2.1 Properties of RH, RHC and RHA

	Ultimate analysis (wt.%, dry & ash free basis)					Proximate analysis (wt.%, dry basis/as received)				S_{BET} (m^2/g)
	C	*H*	*O* [a]	*N*	*S*	*VM* [c]	*FC* [d]	*Ash*	*Moisture*	
RH	37.9	6.3	55.3	0.4	0.1	60.5/ 59.3	11.9/ 10.4	22.0/ 20.5	5.6/ 9.8	2.2
RHC	64.8	2.4	35.1	0.1	0	11.7	34.3	52.0	2.0	117.0 [b]
RHA	9.5	0.3	90.2	0	0	5.4	7.8	85.3	1.5	65.4

Chemical composition of RHA (wt.%)

SiO_2	Al_2O_3	Fe_2O_3	CaO	MgO	Na_2O	K_2O	Zn (ppm)	Mn (ppm)	Cu (ppm)	Cd (ppm)
94.64	0.06	0.23	1.88	0.96	0.39	0.58	18.20	52.24	32.17	0.48

[a] Calculated by mass difference; [b] 700 °C char, changed with pyrolysis conditions;

[c] VM-volatile matters; [d] FC-fixed carbon.

2.2.2 Catalysts Preparation

The general preparation of the RHC/RHA catalysts was illustrated in Fig. 2.1. RHA Ni (Ni^{2+}: 0.2 mol/L), RHA Fe (Fe^{3+}: 0.2 mol/L) and RHA Ni-Fe (Ni^{2+}: 0.1 mol/L, Fe^{3+}: 0.1 mol/L) catalysts were prepared by the incipient wetness impregnation and calcination using $Fe(NO_3)_3{\cdot}9H_2O$ and $Ni(NO_3)_2{\cdot}6H_2O$ as iron and nickel precursors, respectively. After isothermally impregnation and drying at 105 °C, the dry-based metal species in RHC were calcined in the air atmosphere at 600 °C for 1 h. However, RHC Ni-Fe (Ni^{2+}: 0.1 mol/L, Fe^{3+}: 0.1 mol/L) was prepared without calcination. Furthermore, the fresh and used catalysts were characterized by the TGA and the X-ray diffraction (*XRD*, *Rigaku, XRD-DSC II, Japan*), respectively.

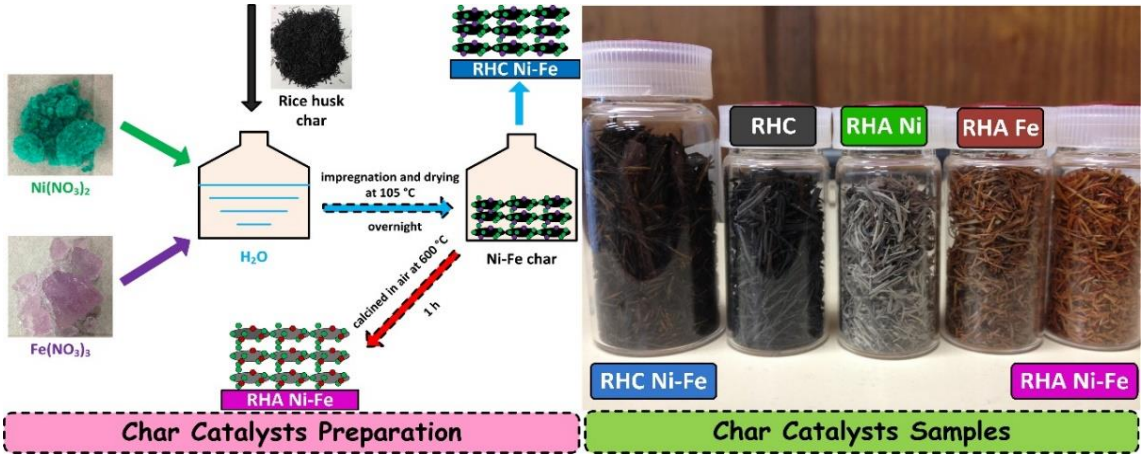

Figure 2.1 Schematic diagram of the RHC/RHA Ni-Fe catalysts preparation procedure

2.2.3 Biomass Gasification and Tar Conversion

The experimental parameters of the operating condition are shown in Table 2.2. Fig. 2.2A presents a schematic diagram of the experimental apparatus, mainly including a gas supplying system, a gas cleaning system and a two-staged pyrolysis facility, which is divided into the gasification zone and the reforming zone. Initially, the temperature was heated up to 800 °C. Subsequently, the carrier gas was continuously supplied to the entire system before adding the feedstock to ensure biomass gasification process conducted in the absence oxygen atmosphere. When raw RH blended with the RHC/RHA supported catalysts was fed into the pyrolyzer, the volatile matters were rapidly released in the forms of gas and tar molecules (Fig. 2.2B). Consequently, biomass tar could be *in-situ* cracked and transformed by thermochemical reactions including catalytic reforming. Finally, the residual tar was condensed and collected in the gas-cleaning unit.

Table 2.2 Experimental Parameters of Operating Conditions

Condition	Parameter
Gasification style	fast pyrolysis
Pyrolysis temperature (°C)	800
Reformer temperature (°C)	800
Biomass feedstock	rice husk
Feedstock size (mm)	<0.5
Sample weight (g)	10
Carrier gas	N_2
Carrier gas flow rate (L/min)	1.0
Char particle size (mm)	original size
Amount of used catalyst (g)	5

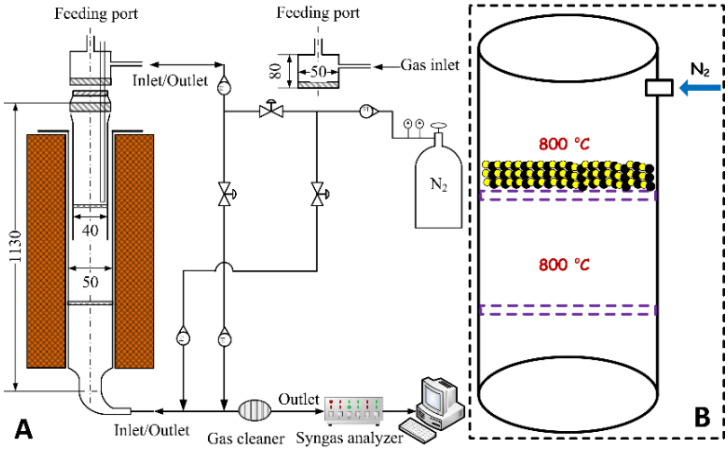

Figure 2.2 Schematic of the experimental setup (A) and biomass gasification scheme (B)

Figure 2.3 Snapshot of the lab-scale experimental setup

2.2.4 Sampling and Analysis

The condensable tar can be collected by isopropanol (IPA) in the ice bath (as illustrated in Fig. 2.4), which is accordingly determined by weighing [2-17]. The yield of producer gas including the non-condensable tar was estimated by the mass balance. The produced syngas mainly composed of H_2, CH_4, CO, CO_2, and C2 (i.e., C_2H_4, C_2H_6) was collected by using an air bag at the outlet and measured by the micro gas chromatograph (*Agilent, Micro GC, 3000A, America*), which was fitted with a thermal conductivity detector (TCD). Each trial was maintained for ten minutes to ensure the mass balance, whilst the repeatability experiments were performed. Thus, the collected tar sample was the total quantity of tars generated from the repeatability experiments.

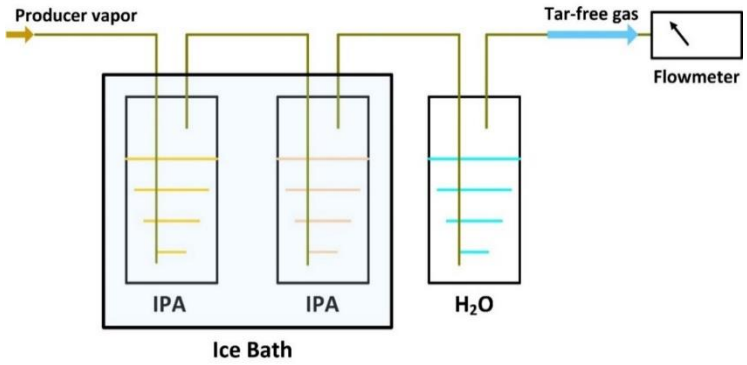

Figure 2.4 Tar condensation and collection by isopropanol (IPA) in the ice bath

2.3 Results and Discussions

2.3.1 Characteristics of RH and RHC

Fig. 2.5 shows the scanning electron microscope (SEM) photographs of RH and RHC with BET surface areas (Table 2.1). From these characterizations, it can be observed that RHC became a highly porous carbon material after high-temperature pyrolysis, just like activated carbon, so it has considerable characteristics to be employed as a catalyst support or a carbon-based adsorbent. Moreover, RH is very abrasive and wears conveying elements very quickly because of the high silica content. RH has a typical globular structure, whose main components are in the lemma or palea form, which tightly

interlocked with another (Fig. 2.5). The corrugate structural outer epidermis is highly ridged, containing papillae and hairs of varying sizes and well organized in a linear profile (linear ridges and furrows), while its ridges are punctuated with the prominent globular protrusions [2-18]. However, biomass are assembled around the stable Si-O carcass, concentrated in the protuberances and hairs (trichomes) on the outer and inner epidermis, adjacent to the rice kernel [2-19]. Many cavities having varying particle sizes were indicated distributing within the ash samples, evidenced of the interconnected porous network and large internal specific surface area [2-20]. RHC obtained from 700 °C pyrolysis can achieve a higher tar adsorption efficiency (more than 80%) due to its larger BET surface area (~117 m^2/g) [2-21], which is higher than the common minerals such as dolomites (5-20 m^2/g) [2-22].

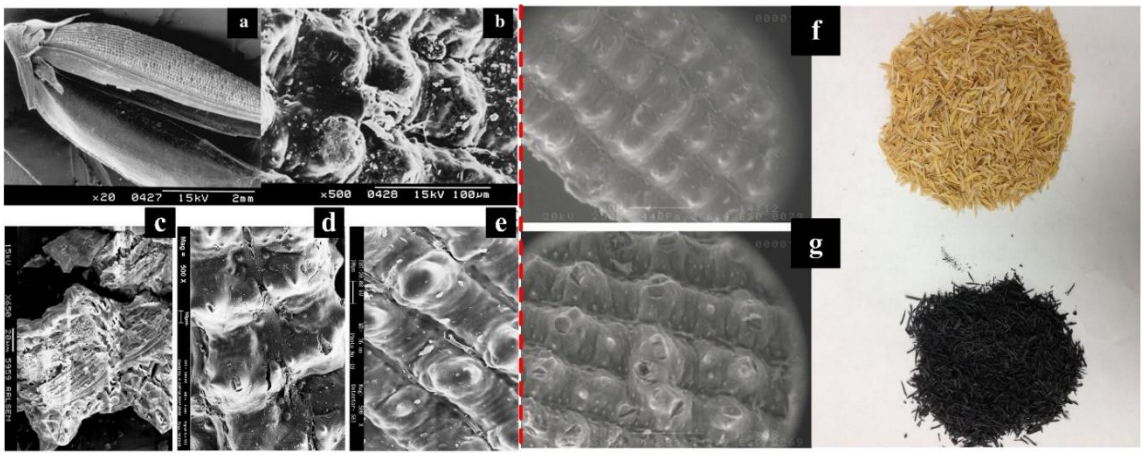

Figure 2.5 SEM images of RH (20×) (a), RH (500×) (b), RHC (1000×) (c) and its morphological details (1000×) (d), (650×) (e); RH (f) and RHC (g) in this work.

Comparative nitrogen adsorption-desorption curves of the grounded raw RH, RHC, RHA and γ-Al_2O_3 are shown in Fig. 2.6. According to the *Brunauer-Deming-Deming-Teller* classification, raw RH obeys the type III adsorption isotherm without the obvious hysteresis loop convex over the entire range, indicating the relatively low specific surface area, pore volume, weak forces and low adsorption performance within the whole range of the studied pressures. With the same classification, both RHC and RHA could be characterized by the type IV adsorption isotherm, resulting from the surface

coverage of mesoporous walls followed by pore filling associated with various hysteresis loops. At relatively low P_i/P_0 values, the isotherms shape is similar to the type II isotherm but at P_i/P_0 values above 0.4, pore condensation would take place, illustrating the porous structures of RHC and RHA. Hysteresis loops associated with capillary condensation in both samples are the narrow type H_1 hysteresis loop, with almost vertical and parallel branches (opened ended cylindrical channel with uniform size and shape), associated with delayed condensation and little percolation hold-up. It can be indicated that carbonized RHC possesses better adsorption performance for metal ions than RH and RHA. Thus, RHC can be employed as a carbon-silica hybrid material with a high heat conductivity and thermal stability.

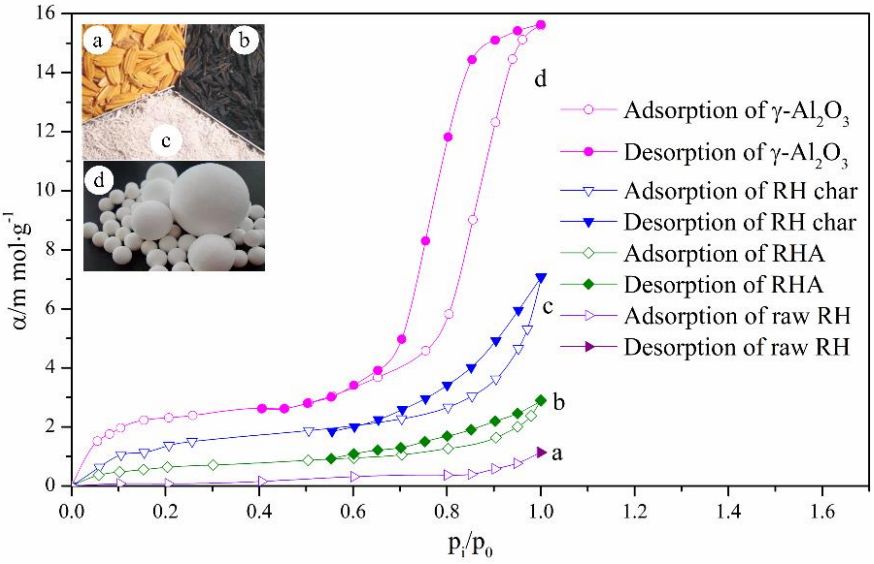

Figure 2.6 Nitrogen adsorption-desorption isotherms at 77 K of (a) RH, (b) RHC, (c) RHA and (d) γ-Al_2O_3

2.3.2 Catalysts Characterization

Fig. 2.7 shows the thermogravimetric (TG) curves of the prepared catalysts in the air atmosphere with a heating rate of 20 °C/min. It can be clearly observed that the RHA supported catalysts had a high thermal stability due to the calcination. However, the weights of RHC and RHC Ni-Fe decreased obviously with the increase of the heating temperature in the air condition. When the temperature was above 400 °C, the weight of RHC decreased rapidly. After that, the weight kept constant after

the temperature increased up to 600 °C. It can be concluded that RHC and RHC Ni-Fe are benefit for tar conversion in the absence or low oxygen atmosphere to extend their service life. It is most likely that most of carbon in RHC can react with sufficient oxygen to generate carbon oxides (i.e., CO, CO_2) at a very high temperature. The carbonaceous residue with a high content of SiO_2 had high thermal stability and abrasive resistance. From the TG curves of RHC and RHC Ni-Fe, it may be concluded that the temperature range of 400-450 °C could be chosen for the thermal regeneration (*e.g., steam activation*) of the RHC supported catalysts.

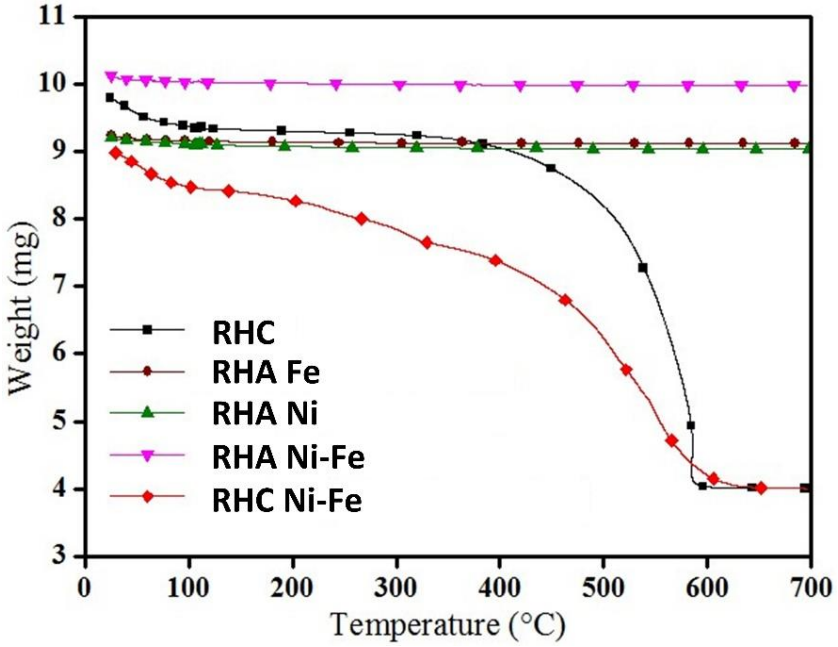

Figure 2.7 TG curves of RHA and RHC supported catalysts under the air atmosphere

The identification of crystal phases was conducted by XRD analysis using Rigaku D/Max 3400 powder diffraction with Cu Kα radiation ($\lambda = 0.1542$) at 45 kV and 40 mA with a scanning rate of 5°/min. Fig. 2.8 shows the XRD patterns of RHC, the fresh and used RHC/RHA supported nickel-iron catalysts. And their characteristic peaks are listed in Table 2.3. The typical amorphous silica characteristic peak in RHC is observed at a broad peak centered at 2ϑ = 22.5°, which is attributed to the presence of disordered cristobalite. In the RHA supported metal (i.e., Fe, Ni) catalysts, the main crystal phases were metal oxides. As for the fresh RHA Fe 1, the iron crystal phases were in the forms of iron oxide

and magnesioferrite, which might be caused by iron oxide sintering with the mineral MgO in RHA. Nevertheless, the iron crystal phases in the used RHA Fe 2 were both iron oxide and metallic iron. During the pyrolysis, partial iron oxide in RHA Fe 1 can be reduced to the metallic iron (i.e., Fe^0) by the carbothermal reduction (R1 and R2) and the hydrogenation reduction (R3). Likewise, partial nickel oxides in the fresh RHA Ni were reduced to the metallic nickel (i.e., Ni^0) after used for biomass catalytic pyrolysis. In addition, the bimetallic catalysts of RHA Ni-Fe and RHC Ni-Fe can form the crystal structures of nickel iron oxides. The nickel oxides in the carbon matrix of RHC could be easier reduced to the metallic nickel, whereas the iron oxides (e.g., Fe_2O_3) were initially transformed into the magnetites (i.e., Fe_3O_4).

$$C + MeO \rightarrow Me + CO \quad (R1)$$

$$CO + MeO \rightarrow Me + CO_2 \quad (R2)$$

$$H_2 + MeO \rightarrow Me + H_2O \quad (R3)$$

MeO refers to the specific divalent metal oxides such as NiO.

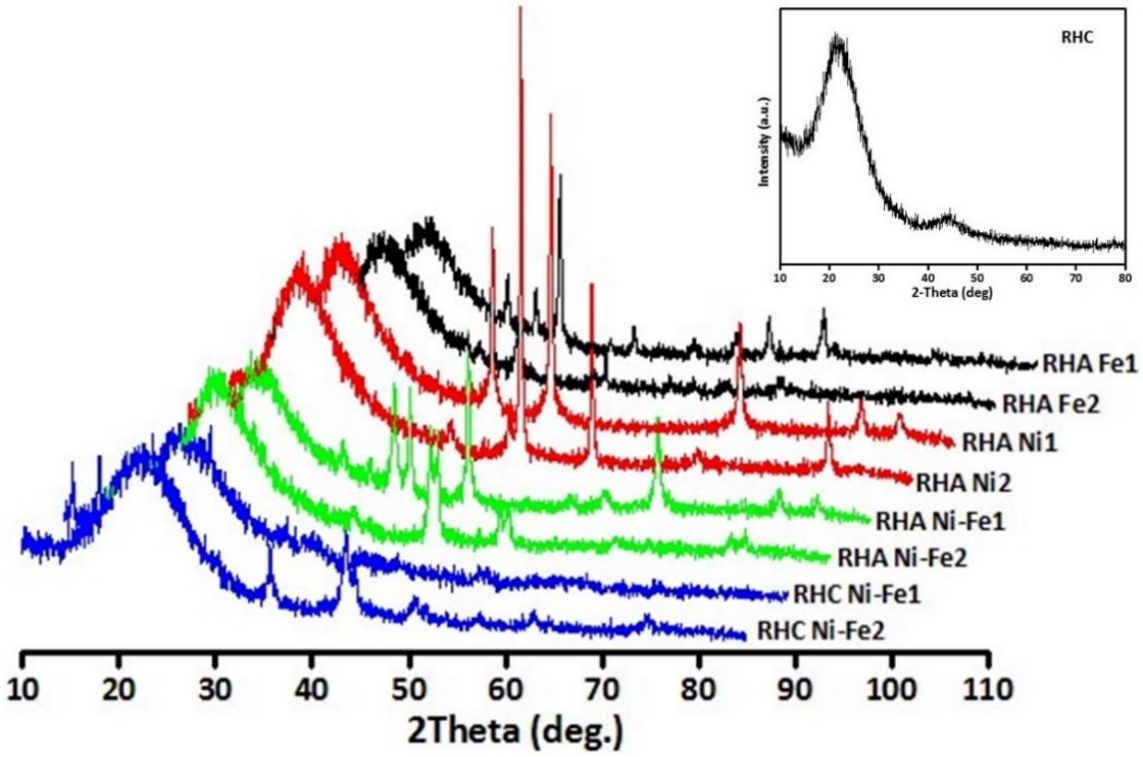

Figure 2.8 XRD patterns of the RHC, the fresh (1) and used (2) RHC/RHA supported catalysts

Table 2.3 XRD Characteristic Peak Lists of the Fresh and Used RHC/RHA Supported Catalysts

No.	2θ (deg)	d (Å)	Height (cps)	FWHM (deg)	Int. I (cps deg)	Phase name
			RHA Fe 1			
1	30.22 (6)	2.955 (5)	70 (8)	0.33 (7)	41 (3)	Magnesioferrite, syn(2,2,0)
2	33.10 (6)	2.705 (4)	72 (8)	0.35 (6)	41 (3)	Iron oxide (1,0,4)
3	35.639 (12)	2.5172 (8)	274 (17)	0.27(2)	120 (3)	Magnesioferrite, syn(3,1,1), Iron oxide (1,1,0)
4	36.9946	2.4280	0.6652	0.4004	5.2712	Magnesioferrite, syn(2,2,2)
5	40.8148	2.2091	338.3194	0.4004	6.6079	Iron oxide(1,1,-3)
6	43.34(8)	2.086(4)	27(5)	0.36(6)	10(2)	Magnesioferrite, syn(4,0,0), Iron oxide(2,0,2)
7	49.53(10)	1.839(3)	14(4)	0.57(14)	11(3)	Iron oxide(0,2,4)
8	53.94(10)	1.699(3)	23(5)	0.65(8)	16(3)	Magnesioferrite, syn(4,2,2), Iron oxide(2,0,5)
9	57.407(14)	1.6039(4)	49(7)	0.37(4)	22(2)	Magnesioferrite, syn(5,1,1), Iron oxide(0,1,8)
10	62.82(2)	1.4781(5)	72(8)	0.40(3)	41(2)	Magnesioferrite, syn(4,4,0)
11	64.13(8)	1.4510(17)	9(3)	0.7(2)	8(12)	Iron oxide(0,2,7)
12	71.3758	1.3204	202.9877	0.4004	2.9033	Magnesioferrite, syn(6,2,0), Iron oxide(1,0,10)
13	74.5292	1.2722	851.8438	0.4004	5.9823	Magnesioferrite, syn(5,3,3)
			RHA Fe 2			
1	30.3(2)	2.95(2)	11(3)	0.6(4)	12(5)	Iron oxide(2,2,0)
2	35.64(3)	2.5169(19)	65(8)	0.55(6)	59(3)	Iron oxide(3,1,1)
3	43.47(15)	2.080(7)	17(4)	0.89(19)	23(5)	Iron oxide(4,0,0)
4	44.63(3)	2.0287(15)	70(8)	0.20(4)	17(2)	Iron, syn(1,1,0)
5	53.81(14)	1.702(4)	4(2)	0.5(4)	2(2)	Iron oxide(4,2,2)
6	57.44(4)	1.6030(11)	13(4)	0.29(12)	6.9(17)	Iron oxide(5,1,1)
7	62.70(14)	1.481(3)	19(4)	0.79(16)	21(3)	Iron oxide(4,4,0)
8	63.90(17)	1.456(4)	7(3)	2.2(8)	32(5)	Iron, syn(2,0,0)
			RHA Ni 1			
1	37.236(19)	2.4128(12)	298(17)	0.29(2)	144(3)	Bunsenite(1,1,1)
2	43.254(9)	2.0900(4)	520(23)	0.27(2)	247(3)	Bunsenite(2,0,0)
3	62.88(3)	1.4767(6)	177(13)	0.41(4)	117(3)	Bunsenite(2,2,0)
4	75.36(3)	1.2602(4)	57(8)	0.39(4)	32(2)	Bunsenite(3,1,1)
5	79.34(10)	1.2066(13)	32(6)	0.51(8)	20(2)	Bunsenite(2,2,2)
			RHA Ni 2			
1	37.1689	2.4170	1.8510	0.1895	11.0002	Bunsenite, syn(1,1,1)
2	43.2593	2.0898	5.6194	0.1895	19.4574	Bunsenite, syn(2,0,0)
3	44.461(10)	2.0360(4)	846(29)	0.189(18)	261(5)	Nickel, syn(1,1,1)
4	51.801(8)	1.7635(3)	331(18)	0.181(14)	103(2)	Nickel, syn(2,0,0)
5	62.9559	1.4752	1.6701	0.1895	6.8988	Bunsenite, syn(2,2,0)
6	76.317(11)	1.2468(15)	128(11)	0.19(2)	42(2)	Nickel, syn(2,2,0)
			RHA Ni-Fe 1			
1	30.35(4)	2.943(4)	40(6)	0.30(7)	18(3)	Nickel iron oxide(2,2,0)
2	33.11(5)	2.704(4)	22.9777	0.17(15)	4.1273	Hematite, syn(1,0,4)
3	35.63(2)	2.5178(14)	167(13)	0.35(4)	110(3)	Nickel iron oxide(3,1,1), Hematite, syn(1,1,0)
4	37.246(14)	2.4121(9)	176(13)	0.24(3)	78(3)	Nickel oxide(0,0,3), Nickel iron oxide(2,2,2)
5	43.262(15)	2.0897(7)	293(17)	0.28(3)	140(3)	Nickel oxide(0,1,2), Nickel iron oxide(4,0,0), Hematite, syn(2,0,2)
6	49.33(17)	1.846(6)	7(3)	0.3(2)	4(2)	Hematite, syn(0,2,4)
7	53.94(2)	1.6985(6)	20(4)	0.10(6)	4.1(12)	Hematite, syn(1,1,6)
8	57.58(4)	1.5995(9)	21(5)	0.60(10)	15(2)	Nickel iron oxide(5,1,1),

						Hematite, syn(1,2,2)
9	62.85(2)	1.4773(5)	151(12)	0.41(5)	112(3)	Nickel oxide(1,1,0), Nickel Iron Oxide(4,4,0)
10	75.36(2)	1.2602(3)	29(5)	0.39(7)	12(2)	Nickel oxide(0,2,1), Nickel iron oxide(6,2,2), Hematite, syn(2,1,7)
11	79.37(8)	1.2062(10)	26(5)	0.42(15)	19(2)	Nickel oxide(0,0,6), Nickel Iron oxide(4,4,4), Hematite, syn(1,3,1)
				RHA Ni-Fe 2		
1	35.93(5)	2.497(3)	16(4)	0.71(15)	13(4)	Tetrataenite(1,0,-1), Maghemite-Q, syn(2,2,5), Magnetite, syn(3,1,1)
2	43.591(19)	2.0746(9)	180(13)	0.44(4)	163(7)	Tetrataenite(1,1,-1), Maghemite-Q, syn(0,0,12), Magnetite, syn(4,0,0), Nickel oxide(2,0,0)
3	44.412(18)	2.0382(8)	137(12)	0.22(3)	45(6)	Nickel, syn(1,1,1), Maghemite-Q, syn(4,0,2)
4	50.87(3)	1.7935(9)	59(8)	0.29(4)	26(4)	Tetrataenite(0,0,2), Maghemite-Q, syn(2,2,11)
5	51.75(8)	1.765(2)	51(7)	0.60(10)	49(6)	Nickel, syn(2,0,0), Maghemite-Q, syn(4,2,4)
6	63.1114	1.4719	4.6439	0.5974	13.9212	Tetrataenite(1,1,-2), Maghemite-Q, syn(3,3,11), Magnetite, syn(4,4,0), Nickel oxide(2,2,0)
7	74.7538	1.2689	43.4666	0.5974	23.0236	Tetrataenite(2,0,-2), Maghemite-Q, syn(5,4,3), Magnetite, syn(5,3,3)
8	76.165	1.2489	37.5747	0.5974	27.5757	Nickel, syn(2,2,0), Maghemite-Q, syn(5,0,13), Magnetite, syn(6,2,2), Nickel oxide(3,1,1)
				RHC Ni-Fe 1		
1	10.94(2)	8.078(16)	63(8)	0.22(3)	17(2)	Nickel nitrate hydroxide hydrate(2,0,0)
2	13.69(3)	6.465(16)	77(9)	0.32(3)	28(3)	Nickel nitrate hydroxide hydrate(2,0,-2)
3	16.6995	5.3045	13.3456	0.3163	9.9955	Nickel nitrate hydroxide hydrate(3,0,0)
4	25.1916	3.5323	136.1396	0.3163	19.3182	Nickel nitrate hydroxide hydrate(2,0,-4)
5	32.9989	2.7123	19.4265	0.3163	10.2001	Nickel nitrate hydroxide hydrate(3,1,0), Hematite, syn(1,0,4)
6	35.8752	2.5011	58.9951	0.3163	10.1228	Hematite, syn(1,1,0)
7	53.7269	1.7047	13.6425	0.3163	4.8268	Hematite, syn(1,1,6)
				RHC Ni-Fe 2		
1	30.20(15)	2.956(14)	23(5)	1.0(3)	48(6)	Maghemite, syn(2,2,0)
2	35.70(3)	2.5129(17)	64(8)	0.44(5)	42(3)	Maghemite, syn(3,1,1)
3	43.43(3)	2.0818(12)	121(11)	0.6597	157.4386	Iron nitride(1,1,1), Maghemite, syn(4,0,0)
4	44.4788	2.0353	63.8036	0.3719	25.2644	Maghemite, syn(4,1,0), Nickel, syn(1,1,1)
5	50.58(7)	1.803(2)	33(6)	0.5454	38.7336	Iron nitride(2,0,0), Maghemite, syn(4,2,1)
6	51.73(3)	1.7659(9)	29.0116	0.3139	17.8529	Nickel, syn(2,0,0)
7	53.89(7)	1.700(2)	10(3)	0.3(3)	5(2)	Maghemite, syn(4,2,2)

8	57.38(18)	1.604(4)	13(4)	0.73(14)	11(3)	Maghemite, syn(5,1,1)
9	62.87(17)	1.477(3)	18(4)	1.1(3)	37(3)	Maghemite, syn(4,4,0)
10	74.42(8)	1.2738(12)	18(4)	1.8(2)	72(4)	Iron nitride(2,2,0), Maghemite, syn(5,4,1), Nickel, syn(2,2,0)

2.3.3 Tar evolution and Conversion Efficiency

Biomass tar is a complex organic mixture of the condensable or non-condensable hydrocarbons comprising single-ring to five-ring aromatic compounds with other oxygen-containing hydrocarbons and polycyclic aromatic hydrocarbons (PAHs) produced during the thermochemical conversion. The most frequent individual tar species studied experimentally and as modeling tar compounds include acetol, acetic acid and guaiacols (primary tars), phenols, cresols and toluene (secondary tars), and naphthalene (tertiary tar). Biomass is generally composed of lignin, cellulose, and hemicellulose. Lignin fraction, which is aromatic form in nature, normally consists of 20-40 wt.% dry-based biomass [2-23]. Scheme 2.1 illustrates the mechanism of tar evolution assuming lignin units as precursors. Three lignin-units of vanillin ($C_8H_8O_3$), guaiacol ($C_7H_8O_2$), and catechol ($C_6H_6O_2$) are pyrolyzed or react with hydrogen. Moreover, the reaction pathway can be determined by the most thermodynamically favorable reactions. Reaction R1 represents the vanillin pyrolysis, and reaction R1a is the vanillin reacting with hydrogen. Phenol is transformed into cyclopentadiene, and CO is abstracted from the phenol according to the reaction R4. Afterward, cyclopentadiene combines to form naphthalene in accord with reaction R7 [2-23], [2-24].

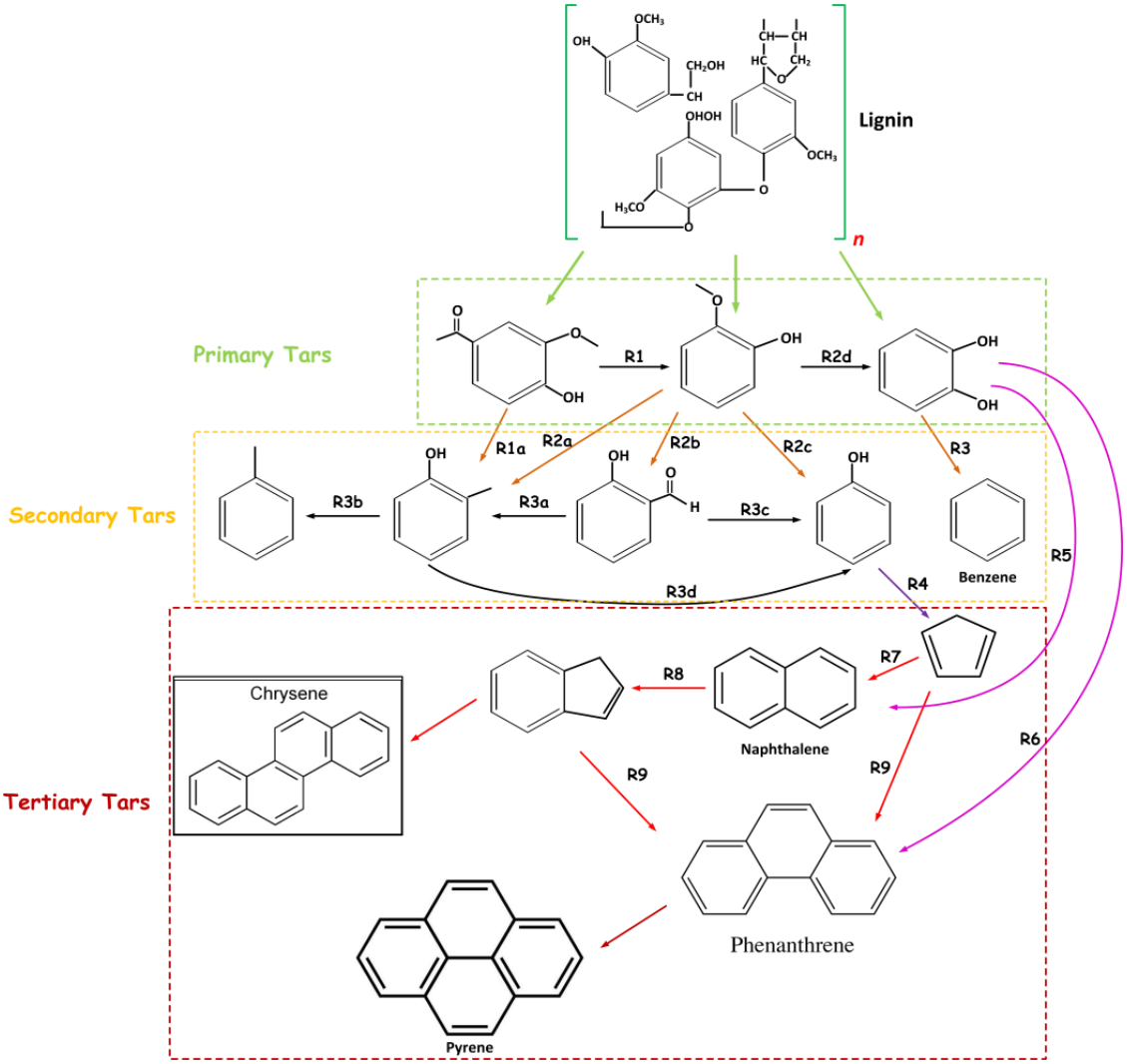

Scheme 2.1 Proposed mechanisms for primary, secondary, and tertiary tar formation

Fig. 2.9 shows the condensable tar yield and the conversion efficiency by co-pyrolysis of RH with the different char-supported catalysts. From the tar instance graphs after *in-situ* conversion, it can be observed that the tar yield decreased by co-pyrolysis with the RHC supported catalysts. Biomass tar conversion efficiency was only 42% by blending with the RHC; whereas it can reach about 93% by blending with the RHA Ni. It can be indicated that the nickel-based catalysts have higher tar cracking/reforming activity as reported in reference [2-25]. Metallic nickel (Ni^0) catalyst exhibited much higher reforming activity of hydrocarbons than the metallic iron (Fe^0) catalysts caused by the high activation energy of C-H and C-C bond in hydrocarbon molecules on the Ni surface. Compared with the two bimetallic catalysts of RHA Ni-Fe and RHC Ni-Fe, RHC Ni-Fe shows higher tar conversion

efficiency (92.3% *vs.* 86%). According to the catalysts characterization, RHA Ni-Fe exists mainly in the form of SiO_2-supported catalyst, whereas RHC Ni-Fe is the carbon-silica hybrid supported catalyst. Carbon in the RHC Ni-Fe plays a significant role for tar reforming. On one hand, porous carbon can enhance the BET surface area of catalysts contributing to the sorption effect; one the other hand, carbon itself can work as an intermediate for decreasing metal oxides and tar at a high temperature by reductive reactions. Guan et al. [2-26] proposed that parts of metal oxides can be reduced into the metallic state by the syngas (e.g., H_2 and CO) initially produced from the biomass pyrolysis without the aid of the catalyst. Therefore, Fe and Ni in their metallic forms rather than their oxide forms were considered the active sites for the tar reforming. Besides, it is possible that the amorphous NiO in the RHC Ni-Fe catalyst might easier to be reduced into the metallic state of Ni (Ni^0) than the crystalline NiO in RHA Ni-Fe. Therefore, RHC Ni-Fe without calcination and H_2 pretreatment can also be used for the tar conversion. The synergistic effect between the activation of tar on the nickel species and the oxygen atom supplied to the carbonaceous intermediate from neighboring iron atoms was not displayed. Probably without the presence of steam, the iron distribution in the samples after pyrolysis shows an imbalance between the phases FeO and Fe_3O_4 providing for tar reforming. Those iron species always take place in the redox equations of water gas shift reactions (i.e., R4, R5). Therefore, steam reforming with the char-supported monometallic Fe and bimetallic Ni-Fe catalysts should be further studied to enhance the tar conversion efficiency and H_2 yield.

$$Fe_3O_4 + CO \leftrightarrow 3FeO + CO_2 \qquad \text{(R4)}$$

$$3FeO + H_2O \leftrightarrow H_2 + Fe_3O_4 \qquad \text{(R5)}$$

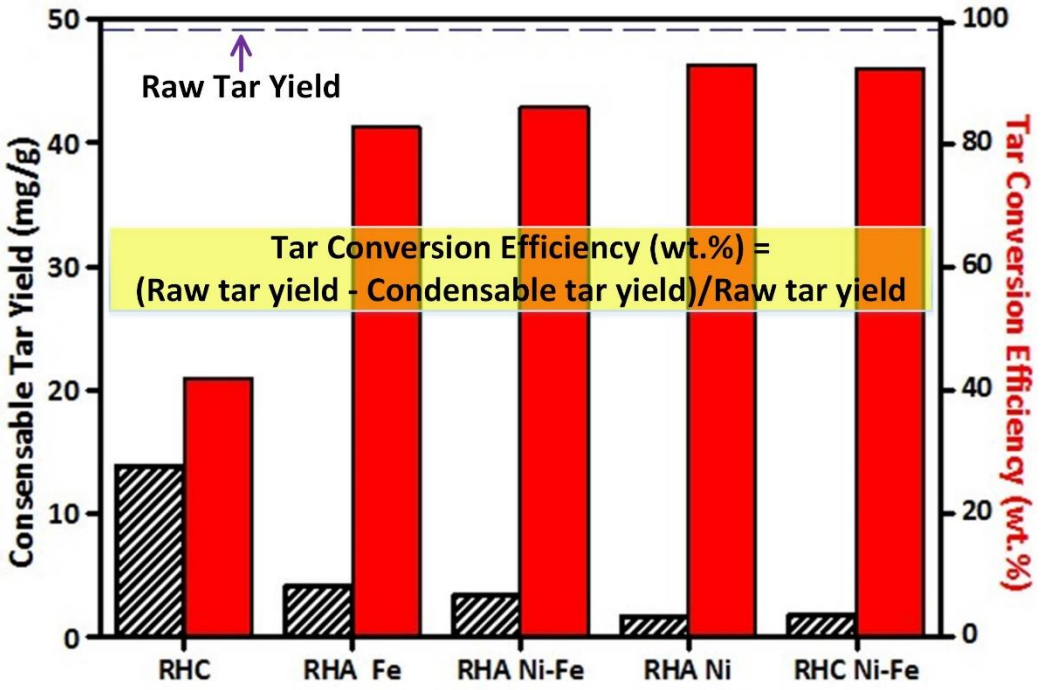

Figure 2.9 Heavy tar yield and conversion efficiency with the different char-supported catalysts

As shown in Fig. 2.10, the composition of tar derived from RH fast pyrolysis is composed of polycyclic aromatic compounds, e.g., indene, naphthalene, methylnaphthalenes, biphenyl, acenaphthylene, and phenanthrene, which have been considered as the main tar compounds in different thermal processes such as pyrolysis or gasification of biomass and wastes. Although benzene and toluene have been also reported as tar compounds, they are volatile enough to be evaporated during the collection and analysis process. Herein, the resulting samples were deficient in lighter aromatic compounds such as benzene. Using the RHC Ni-Fe, the signals of 3 and 4-ring compounds were reduced and cracked into 2-ring or 1-ring organic compounds, e.g., phenanthrene; nevertheless, 1-ring compounds such as styrene are accordingly detected. The lighter hydrocarbons can be subsequently aromatized via the *Diels-Alder* type reactions due to the thermal degradation of alkanes into alkenes resulting in the formation of 1-ring compounds such as toluene and styrene. The following reactions could illustrate the formation mechanism for toluene and alkylaromatics, which are possibly produced by alkane's thermal-degradation via *Diels-Alder* reaction (Scheme 2.2).

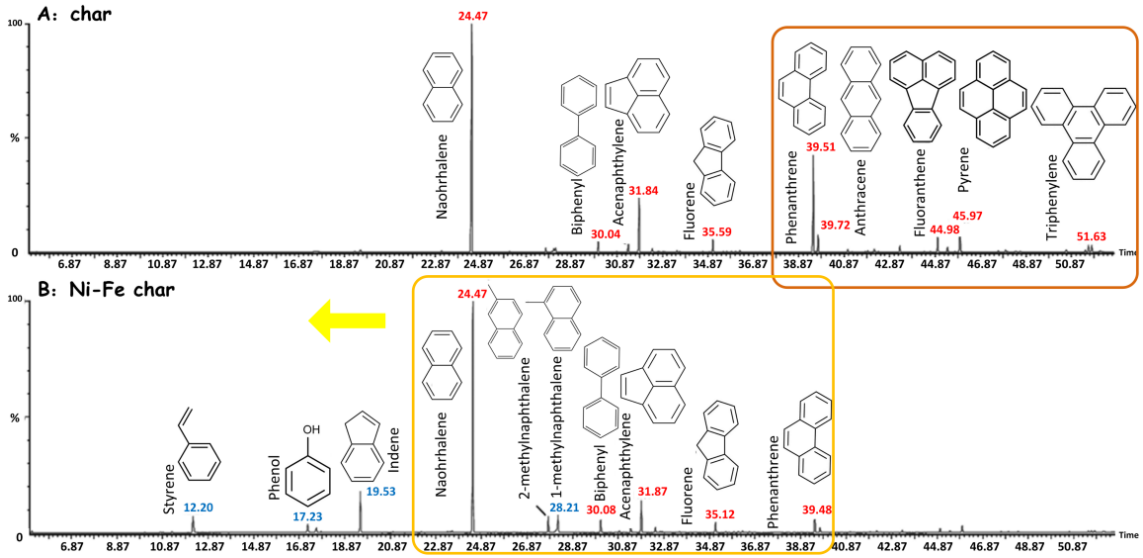

Figure 2.10 Tar components derived from RH co-pyrolysis with RHC and Ni-Fe char (RHC Ni-Fe)

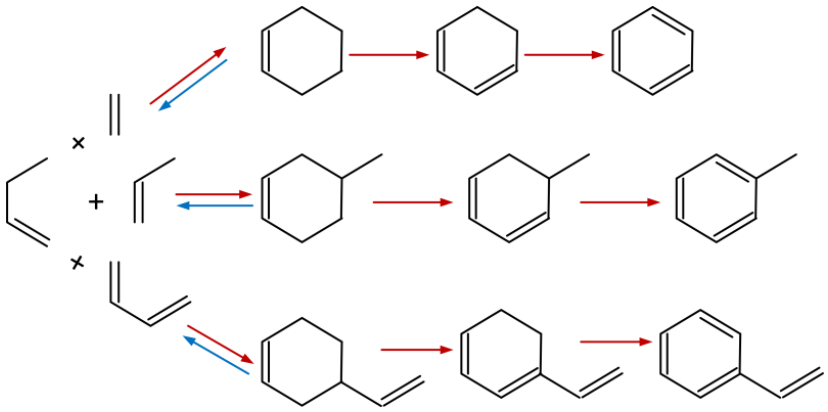

Scheme 2.2 the formation mechanism for toluene and alkylaromatics produced by thermal degradation of alkanes via Diels-Alder reaction

2.3.4 Gas Yield and Composition

Synthesis gas is the predominant product of biomass gasification. Their properties can reflect the pyrolysis and tar conversion efficiency with different catalysts, since tar is cracked to small molecular gases by the catalytic reforming. The gas yield could be estimated by expression (E1). In addition, the concentration of syngas components (i.e., H_2, CO, CO_2, CH_4, C_2H_4 and C_2H_6) can be calculated by expression (E2)-(E6).

$$\text{Gas } Yield\ (L/g) = \frac{\text{Exit gas (L)} - \text{N}_2 \text{ flow rate (L/min)} \times \text{Pyrolysis time (min)}}{\text{Feedstock weight (g)}} \qquad \text{(E1)}$$

$$\mathrm{H_2\,(vol.\%)} = \frac{H_2(\%)}{H_2(\%)+CO(\%)+CO_2(\%)+CH_4(\%)+C_2H_4(\%)+C_2H_6(\%)} \quad \text{(E2)}$$

$$\mathrm{CO\ (vol.\%)} = \frac{CO(\%)}{H_2(\%)+CO(\%)+CO_2(\%)+CH_4(\%)+C_2H_4(\%)+C_2H_6(\%)} \quad \text{(E3)}$$

$$\mathrm{CO_2(vol.\%)} = \frac{CO_2(\%)}{H_2(\%)+CO(\%)+CO_2(\%)+CH_4(\%)+C_2H_4(\%)+C_2H_6(\%)} \quad \text{(E4)}$$

$$\mathrm{CH_4\ (vol.\%)} = \frac{CH_4(\%)}{H_2(\%)+CO(\%)+CO_2(\%)+CH_4(\%)+C_2H_4(\%)+C_2H_6(\%)} \quad \text{(E5)}$$

$$\mathrm{C2\,(vol.\%)} = \frac{C_2H_4(\%)+C_2H_6(\%)}{H_2(\%)+CO(\%)+CO_2(\%)+CH_4(\%)+C_2H_4(\%)+C_2H_6(\%)} \quad \text{(E6)}$$

Fig. 2.11 shows the producer gas yield and syngas composition when different catalysts were used. It can be found that the amount of gas yield increased when the RHC and RHC-supported catalysts were applied. The increase of the gas yield may be attributed to the thermochemical reactions between char, tar and catalysts at higher temperatures. On the one hand, char can react with syngas (i.e., CO_2 and H_2) to produce more other syngas components (i.e., CO, CH_4); on the other hand, tar can be cracked and converted into gas components by dry reforming over RHC and RHC-supported catalysts. More importantly, the further devolatilization of char can contribute to the increase of gas yield. In particular, the gas yield can reach approximately 2.11 L/g when co-pyrolysis of RH and RHC Ni-Fe at 800 ^{o}C. When char was blended with RH, the CO volume concentration increased from 44.8% to 52.0%, while the CO_2 volume concentration decreased from 24.0% to 15.8%. It is suggested that CO_2 most likely reacted with carbon in char by *Boudouard reaction* in the presence of nickel catalysts, resulting in the increase of the volume concentration of CO. Meanwhile, the volume concentration of methane (CH_4) slightly increased from 7.5% to 8.0%, possibly due to the methanation reactions between CO_2, C and H_2. In addition, char itself could play the role of an adsorption-enhanced catalyst for tar and CO_2 conversion.

Because of further decomposition of char and the catalytic effect, the gas yield by mixing with the RHC Ni-Fe was slight higher than the gas yield by blending with the RHA Ni-Fe (2.11 L/g *vs.* 1.96 L/g).

Regarding to the volume concentrations of CO (55.2% *vs.* 41.8%) and H_2 (22.7% *vs.* 31.5%), it was concluded that H_2 could be slightly consumed in the presence of char and metal oxides at the high temperatures. In this work, the high volume concentration of H_2 was not achieved, but the volume concentrations of CO and CH_4 got improved. It should be noted that compared to raw yield (24.0%), CO_2 volume concentrations were greatly decreased (the yields as follows: 15.8, 11.9, and 8.2%) by blending with RHC, RHC Ni-Fe and RHA Ni, respectively. Furthermore, it corresponds to the previous result that NiO can play a critical role in decreasing the carbon deposition and increasing the amount of CO in the gaseous product [2-27]. The lower heating value (LHV) and the higher heating value (HHV) of syngas is calculated by the empirical expressions E7 [2-28] and E8 [2-29], respectively, where (CO), (H_2), and (CH_4) are molar fraction of syngas in Fig. 2.11. The theoretical results are shown in Table 2.4. The LHV and HHV can reach about 10.64-12.80 MJ/m^3, and 13.02-14.55 MJ/m^3, respectively, at 800 °C, indicating a good quality of syngas. Furthermore, the syngas showed a higher HHV by co-pyrolysis with the RHC and RHC supported catalysts.

$$\mathrm{LHV}(kJ/m^3) = [30(CO) + 25.7(H_2) + 85.4(CH_4)] \times 4.2 \quad \text{(E7)}$$

$$\mathrm{HHV}(kJ/Nm^3) = \frac{12.63(CO) + 12.75(H_2) + 39.82(CH_4) + 63.43(C_nH_m)}{100} \quad \text{(E8)}$$

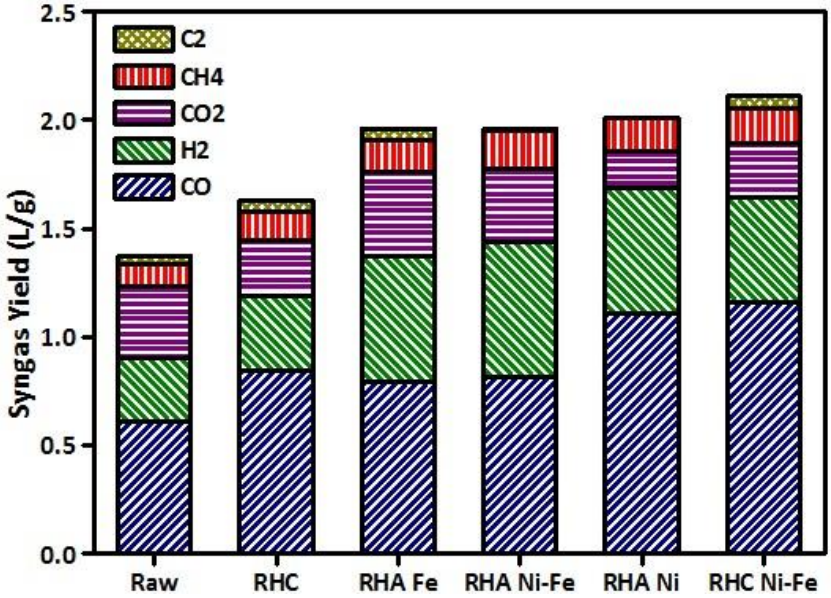

Figure 2.11 Gas yield and composition with char and char-supported catalyst

Table 2.4 LHV and HHV of the Produced Syngas using RHC and RHC/RHA Supported Catalysts

	No catalyst	RHC	RHA Fe	RHA Ni-Fe	RHA Ni	RHC Ni-Fe
LHV (MJ/m^3)	10.64	11.69	10.95	11.93	12.80	12.10
HHV (MJ/m^3)	13.02	14.46	13.50	13.17	13.78	14.55

2.3.5 Mass Balance

The main products derived from RH pyrolysis are composed of gas, solid and liquid. As above, the composition of gas products usually includes CO, H_2, CO, CH_4, CO_2 and light hydrocarbons. The liquid products normally include water and tar (i.e., heavy and light tar), estimated by the difference of gas and solid products. Besides, the solid product is defined as the char or ash (exclusive of catalysts). Fig. 2.12 shows the yields of products derived from RH co-pyrolysis with RHA or RHC supported catalysts. It is found that the yield of solid product could keep stable with or without catalysts, indicating the char was not consumed by the pyrolysis. The yield of gas product increased with the yield decrease of the liquid product. It suggests that the liquid product could be transformed into the gas product via the catalytic conversion, e.g., the dry and the steam reforming.

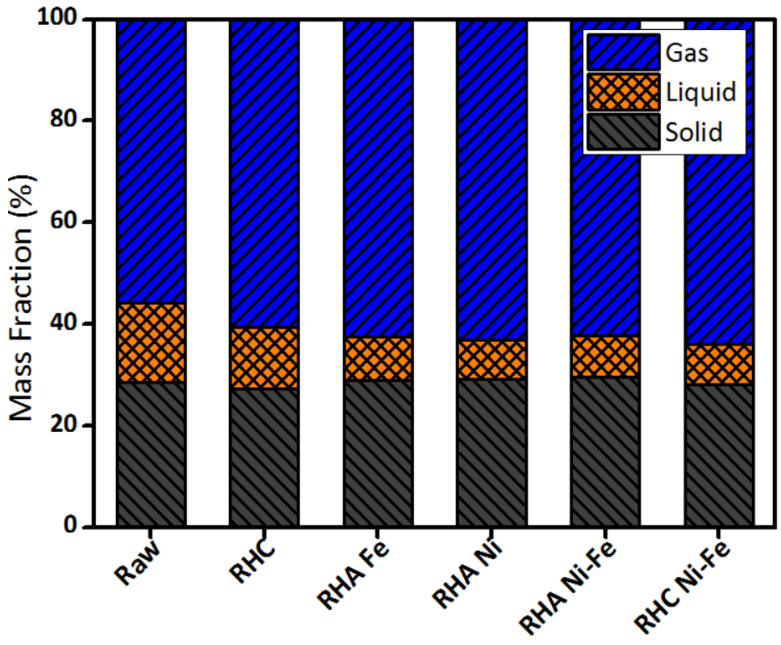

Figure 2.12 Products yields from RH co-pyrolysis with RHC or RHA supported catalysts

2.3.6 XPS Analysis

X-ray photoelectron spectroscopy (XPS) analysis has been widely applied for studying the surface chemistry of metals, alloys, oxides and hydroxides with particular reference to oxidation, corrosion and chemical attack including acid dissolution. In this work, the XPS spectra of the studied catalysts indicated the presence of four distinct peaks due to nickel, iron, silica and carbon. The XPS patterns of Ni 2p, Si 2p, and C 1s regions for RHA Ni are depicted in Fig. 2.13A, with the curve-fitting spectra included. It is clearly observed that an understanding of multiple splitting and satellite structure is crucial to the interpretation of the Ni 2p line-shape. In general, the charging effects were corrected by adjusting the binding energy of C 1s to 284.6 eV. The binding energy of NiO usually distributes at 853.3 eV in the standard spectrum. However, the Ni 2p3/2 peak of RHA Ni centered at 855.1 eV attributed to the strong interaction with the support (e.g., silica, alumina) indicating the presence of NiO or other substances between NiO and $NiAl_2O_4$. The presence of satellite peaks demonstrated nickel species in the forms of NiO or Ni_2O_3 were present in the oxygen-containing environment for calcination. After the reaction, the satellite peaks disappeared possibly due to the carbthermal reduction under the low oxygen condition, corresponding to the previous results of XRD analysis. Meanwhile, more disordered small peaks appeared around 852.0 eV indicating the peaks of metallic Ni possibly due to the nickel oxides reduction (Fig. 2.13B). It was reported that nickel oxide showed a little interaction with silica but strong interaction with alumina in the impregnated catalysts after calcination [2-30]. NiO can react with Al_2O_3 in the air at 450-600 ^oC to generate $NiAl_2O_4$ spinel onto the surface [2-30]. $NiAl_2O_4$ at the binding energy of 855.4 eV is present in the RHA Ni as well (Fig. 2.13). The spinel peak was not detected by XRD measurement explained by the poor crystallinity and trace amount of spinel formed at the lower calcination temperature and the shorter calcination time. Besides, it can be obviously seen that the carbon energy loss peak at ~296 eV in the RHA Ni, indicating that carbon in RHC became more stable after the reaction.

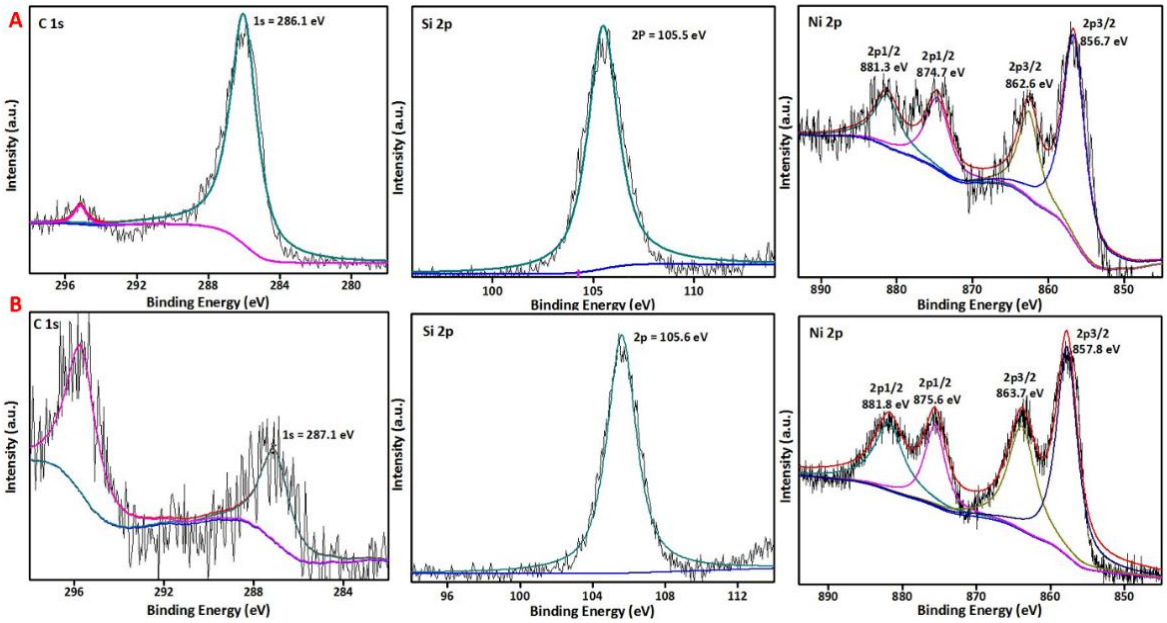

Figure 2.13 XPS patterns of the fresh and used RHA Ni catalyst

Although oxidizing gases are possibly generated from the nitrate salt decomposition, the only crystalline species observed are the reduced iron oxides, suggesting that the impact of these low concentration gases on the chemical impregnated iron oxides is negligible. It was also reported that Fe_2O_3 could be reduced into Fe_3O_4 or other reduced iron species by CO and H_2 [2-31]. The peak positions of Fe 2p1/2 and Fe 2p3/2 depend on the ionic states of Fe. Meanwhile, the satellite peak positions for the Fe 2p1/2 and Fe 2p3/2 peaks are very sensitive to the oxidation states. Thus, these peaks could be used for qualitatively determining the ionic states of iron. In general, the binding energies of FeO, Fe_3O_4, Fe_2O_3 and FeO(OH) distribute at 109.4, 708.2, 710.9 and 711.3 eV, respectively, in the standard spectrum. The XPS patterns of Ni 2p, Fe 2p, Si 2p, and C 1s regions for the fresh RHC Ni-Fe are depicted in Fig. 2.14A. Of the two peaks of Fe 2p, the Fe 2p3/2 peak is narrower and stronger than the Fe 2p1/2 peak and the area of Fe 2p3/2 peak is larger than that of Fe 2p1/2 because in spin-orbit (j-j) coupling; Fe 2p3/2 has degeneracy of four states whilst Fe 2p1/2 has only two [2-32]. The fresh RHC Ni-Fe showed that the Ni 2p3/2 binding energy at 856.7 eV identified as the peak of $Ni(OH)_2$, and the Fe 2p3/2 binding energy at 711.1 eV identified as the peak of FeO(OH) or other substances between Fe_2O_3 and FeO(OH). The Fe 2p3/2 peak also has associated

satellite peaks indicating the presence of Fe^{2+} and Fe^{3+}, which is located approximately 8 eV higher than the main Fe 2p3/2 peak (Fig. 2.14A). Indeed, Fe_2O_3 and Fe_3O_4 existed in the fresh RHC Ni-Fe, in agreement with the XRD data. After the reaction (Fig. 2.14B), all the characteristic peaks of Fe 2p3/2, Fe 2p1/2, Ni 2p3/2 and Ni 2p1/2 shifted substantially to the left. The reason may be ascribed to the enhancement of carbon adsorption due to the crystal structure change of the carbon material. Without calcination, the carbon loss peak cannot be observed in the RHC Ni-Fe. Moreover, the C 1s peak was attributed to the presence of other organic functional groups (i.e., C=O, C-H, C-C, C-OH, COOH), which may be ascribed to coke deposition on the char surface. Besides, it can be observed that the metallic state of nickel (Ni^0) was *in-situ* generated in the RHC Ni-Fe after the reaction, which was further characterized by the Ni 2p3/2 peak at 852.7 eV. Consequently, the chemical state of the RHC-supported Ni-Fe catalyst can be changed as illustrated in Scheme 2.3.

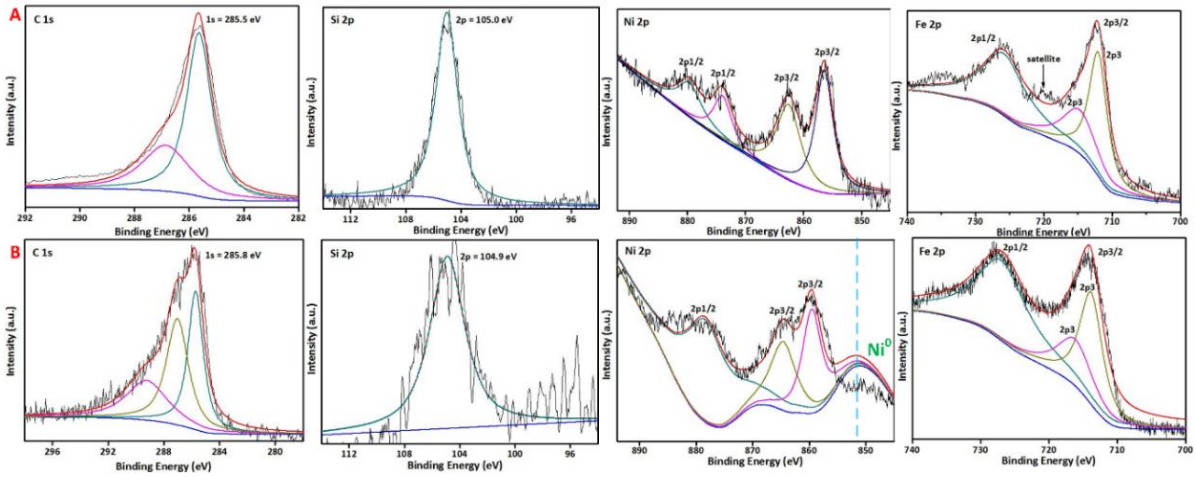

Figure 2.14 XPS patterns of RHC Ni-Fe catalyst before and after the reaction

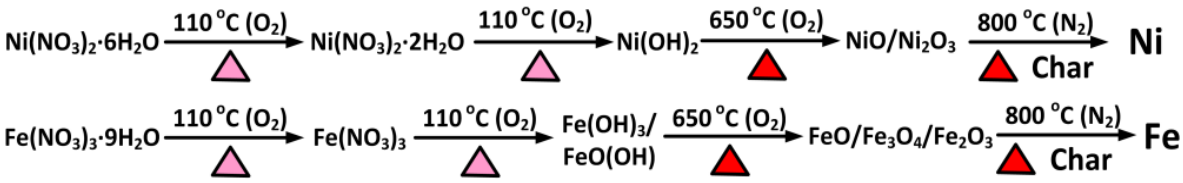

Scheme 2.3 Chemical state changes of char-supported Ni and Fe catalysts

2.3.7 Tar Catalytic Conversion Mechanisms

The mechanisms of the biomass gasification process along with tar reforming could be expressed

by the partial combustion reactions, the heterogeneous and homogenous reactions, followed by (R6)-(R17) in Table 2.5. Catalytic reforming reactions can cleave the C-C and C-H bonds of the carbohydrate backbone to yield a combination of CO and H_2 (R8-R10) [2-33]. If steam (H_2O) is in presence, CO_2 could be formed via the WGS reaction to generate more H_2 (R17). The aqueous-phase reforming by bimetallic catalysts can produce H_2 and CO_2 starting with sugars and sugar alcohols [2-34]. The selectivity towards hydrogen could be controlled using catalysts with different metals (*e.g., Pt*) and metal-alloys (*e.g., Raney Ni-Sn*) [2-35]. Abu El-Rub et al. [2-36] thought that tars can be adsorbed on the active sites of char particles. The adsorbed tars and cokes can be catalytically reformed to CO and H_2 through the steam and dry thermochemical reactions. Meanwhile, free radicals that enter polymerization reactions and coke on char surfaces can be formed from tar decomposition. The gasification reactions of coke cannot increase CO and H_2 in syngas, but refresh the active surface area of char at the temperature above 800 °C [2-36]. These reactions may explain the increasing trend of CO followed by the temperature increase because more CO than H_2 is produced. As char is utilized as a catalyst support, char may react with CO_2 to produce extra CO and CH_4 without additional steam and oxygenated compounds (R11 and R12).

Table 2.5 Chemical Reactions Occurring in the Biomass Pyrolysis/Gasification Process

Reactions	Simplified Expressions	
gasification/pyrolysis	$C_xH_yO_z \rightarrow H_2 + CO + CO_2 + CH_4 + C2 + Tar + Char$	(R6)
tar cracking	$Tars \rightarrow C + C_nH_m + gases$	(R7)
dry reforming (*major*)	$C_nH_m + n\ CO_2 \rightarrow 2n\ CO + (m/2)\ H_2 + Q$	(R8)
steam reforming (*minor*)	$C_nH_m + n\ H_2O \rightarrow n\ CO + (n+m/2)\ H_2 + Q$	(R9)
	$C_nH_m + 2n\ H_2O \rightarrow n\ CO_2 + (m/2+2n)\ H_2 + Q$	(R10)
methanation	$CH_4 + H_2O \leftrightarrow CO + 3\ H_2$	(R11)
	$CO_2 + 4\ H_2 \leftrightarrow CH_4 + 2\ H_2O$	(R12)

	$C + 2\ H_2 \leftrightarrow CH_4$	(R13)
Boudouard reaction	$C + CO_2 \rightarrow 2\ CO$	(R14)
water gas reaction	$C + H_2O \rightarrow CO + H_2$	(R15)
	$C + 2\ H_2O \rightarrow CO_2 + 2\ H_2$	(R16)
water-gas-shift (WGS)	$CO + H_2O \leftrightarrow CO_2 + H_2$	(R17)
carbothermal reduction	$C + Me^{2+} \rightarrow Me + C^{2+}$	(R18)
	$n\ C + Me_mO_n \rightarrow m\ Me + n\ CO$	(R19)
	$n\ CO + Me_mO_n \rightarrow m\ Me + n\ CO_2$	(R21)
hydrogenation reduction	$n\ H_2 + Me_mO_n \rightarrow m\ Me + n\ H_2O$	(R20)

Note: Me^{2+} and Me_mO_n refer to metal ions and metallic oxides, respectively.

In the current work, the monometallic nickel catalysts exhibited much higher reforming activity of hydrocarbons than the monometallic iron catalysts. This property is caused by the high activation ability of C–H and C–C bond in the hydrocarbon molecules on the surface of metal actives. Consequently, it seems that the additive effect of iron is the increase of the number of active Ni surface, but the characterization results on the particle size and surface enrichment of Fe on the Ni-Fe bimetallic particles did not support the increase of the surface of nickel actives. Another possible reason is that iron has a synergistically catalytic effect. Since iron has high oxygen affinity than that of nickel, the addition of iron to nickel catalysts can increase the coverage of oxygen atoms during the cracking/reforming reactions. The catalytic reactivity of RHC/RHA supported Ni-Fe catalysts for tar conversion can be concluded in the following order: RHA Ni > RHC Ni-Fe > RHA Ni-Fe > RHA Fe > RHC. The carbothermal reduction and the hydorgenation reduction can interact between the char, reducing gas and metal oxides during biomass pyrolysis, which reduced partial metal oxides into the metallic states (R18-R21) to promote tar catalytic conversion.

Fig. 2.15 illustrated tar *in-situ* conversion mechanism by the RHC supported Ni-Fe catalysts. In the pyrolyzer, biomass was initially decomposed to the small molecular gases, tar, char and water by

means of the thermochemical reactions. The formed tar was cracked and reformed simultaneously by co-pyrolysis with the RHC supported Ni-Fe catalysts at high temperatures. After that, a part of the RHC supported catalysts were converted to the silica-based catalysts due to the char conversion. In summary, RHC can play two significant roles during the process of biomass pyrolysis. On one hand, it provides the carbon atom to reduce the metal oxides into the low-valent metal state via the carbothermal reduction; on the other hand, it is considered as an adsorptive-support to adsorb metal ions and tar. It is well known that the sublimation temperatures of nickel and iron can reach up to 2732.0 °C and 1535 °C, respectively. Thus, the metal species can stably maintain in the solid residues to be further activated via the thermal regeneration or the direct catalytic gasification to be converted into the additional syngas.

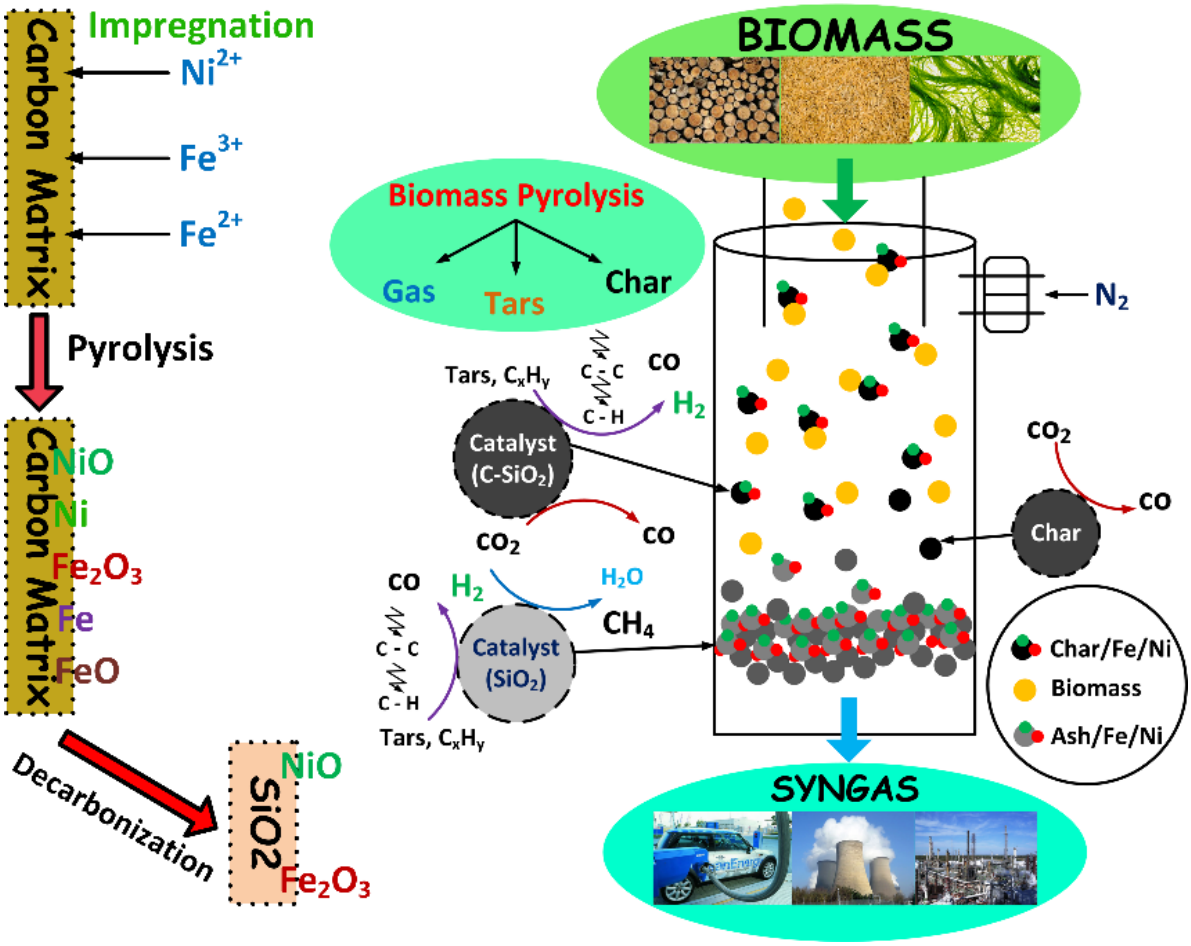

Figure 2.15 Mechanism illustration of *in-situ* tar conversion by char catalysts for biomass gasification

2.3.8 Mixing-simulation in Fluidized Bed Gasifier (FBG)

Gasification of biomass and wastes in FBG has advantages, since FBGs are capable of being used in the pilot and large scales, overcoming limitations found in smaller scale, fixed-bed gasifiers. On the other hand, the bed temperature is limited to avoid the bed agglomeration and the gasification efficiency of a fluidized bed (FB) may be limited if part of the fuel energy remains in unconverted char. Meanwhile, if the temperature is not high enough in the gasifier, tar in the producer gas can make the process unsuitable from a technical and economical points of view. Models can be helpful for designing gasifiers, for predicting operation behavior and emissions during normal conditions, startup, shutdown, changes of fuel and load. The modeling can be carried out from preliminary design of an industrial process to complex simulation of a unit. Experiments, especially at large scale facilities, are usually expensive and complicated. Nevertheless, modeling is economical and convenient and it can support the preparation and optimization of experiments to be conducted in a real system [2-37]. The tools available for modeling of the FBG reactors are the more or less simplified equations for conservation of mass, energy and momentum, which complemented by boundary conditions, constitutive relationships, and terms expressing the sources and sinks of the system. To determine the latter, rate laws for the chemical or physical conversion processes are required. The thermodynamic data are considerable to estimate properties and thermal data as well as the reaction products by the equilibrium assumptions.

Fig. 2.16 schematically presents the processes of each process occurring in an FBG including the bed level with bubble and emulsion phases, the particle level with gases release and char gasification, and the gas phase reactions where water gas shift reaction plays a significant role. Some processes strongly interact between one level and another. For instance, the heat and mass transport to a particle takes place on the particle level, while their rates are determined by the fluid dynamics of the bed (reactor level) and by fuel reactivity, both in the case of the devolatilization and the char

conversion. Moreover, these processes are included in source terms of the conservation equations treated by the sub-models during the execution of numerical calculations. The description on the particle level is composed of the particle size and biomass properties, such as the density and the thermal conductivity, which affect the devolatilization time and the volatiles composition. On the reactor level, various factors are considered: the residence time (mass inventory in an FB), the boundary conditions, just like the fuel feed points and the feed rate, the freeboard size, the fluidization velocity, and their effects on solids elutriation, solids and gas mixing, segregation, etc. [2-37]

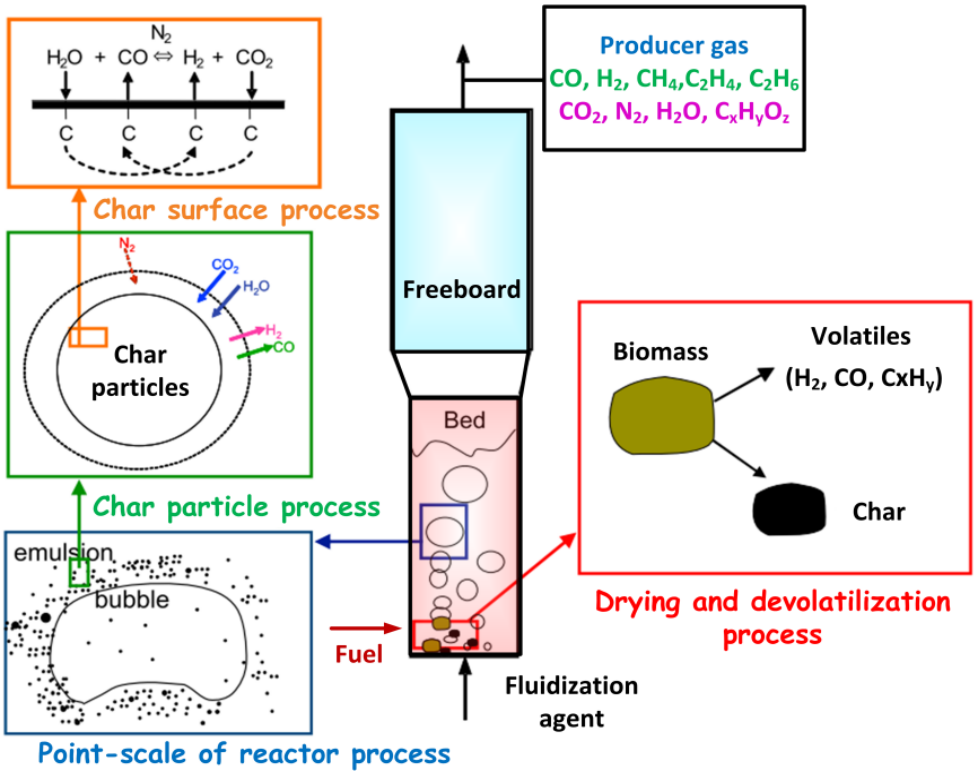

Figure 2.16 Description of processes in an FBG [2-37]

The performance of FBG, including the carbon conversion efficiency and the tar content, may significantly depend on the movement of solids and gas in the bed and the freeboard. For instance, in a pilot circulating FBG (CFBG), reactor conditions resulting in the lack of contact between char/oxygen and tar/catalyst and an unfavorable consumption of oxygen by the devolatilization gases were identified, resulting in lower char conversion and higher tar content in the product gas.

Modeling of solids and gas mixing could identify the best arrangement for design and operation of the gasifier. Particularly, the solid-solid mixing simulation could optimize the operation parameter of solid particles (i.e., biomass, catalyst, bed material) in FBG.

In theory, the solid-solid mixing of species *i* could be determined by the expression E9, applied for the transport of solid (*index s*) in an isothermal system. The closest representation of the real process is a balance on the transported variables formulated and solved for each phase *k* (gas and solids and their *i* components): the density, the momentum, and the enthalpy (ρ_k, $\rho_{k,i}$, μ_k, and $\hbar_k$, in general terms, ϕ). The balance of the conserved variables φ over a fixed element (*eulerian formulation*) of the reactor volume can be expressed in the following form (somewhat simplified, in the case of momentum), applicable to any reactor types: the accumulation of ϕ is due to the net difference between the rates of change by convection and dispersion or by generation and consumption, S, per unit volume.

$$\frac{\partial \varphi_k}{\partial t} + div(u_k\, \varphi_k) = div(D \varphi_k\, grad \varphi_k) + S_{\varphi,k} \qquad \text{(E9)}$$

$$\frac{\partial c_{si}}{\partial t} + div(u_s\, c_{si}) = div(D_{sV/H,i}\, grad\, c_{si}) + S_{si} \qquad \text{(E10)}$$

The solids movement in an FB is often described by the simple version of the expression E9, in which diffusion and convection are lumped into one term, called dispersion and expressed by the fine particles and deep beds, i.e., chemical reactors, where the small-scale mixing mechanisms are dominant. In the FB, besides the inert bed material or solid catalyst, there is a distribution of fuel and char particles in the bed. Therefore, the movement of solids in the vessel should be described by accounting for three or more solids types. Nevertheless, qualitatively the motion of biofuel particles could be visualized as the movement of flotsam particles in a jetsam-rich bubbling FB (BFB). A high superficial velocity might improve the mixing behavior, but biomass particles with lower density and larger size than bed material particles are still non-uniformly distributed. At a given

fluidization velocity, char particles are most likely to be elutriated from the bed or to sink from the bed surface than devolatilizing particles. The reason is that the jet force from escaping volatile matters tends to keep them floating. A key issue in modeling FBG is whether the fuel particles keep floating, once they have reached the bed surface or if they are compelled to descend. This depends much on the segregation behavior of a few flotsam particles in a bed of many jetsam particles. Thereby, segregation should be avoided to preserve the bed from sintering or excessive tar emission in an FBG. Segregation is most likely to occur if the ratio is equal to or below 0.5. A mixing ratio between 0.5 and 1 is desirable for avoiding the segregation problems [2-37]. However, Fermoso et al. [2-38] also investigated a sorption enhanced catalytic steam gasification of biomass in a combined downdraft FB and fixed bed reactor. The solids feed was composed of 15 wt% of raw biomass and 85 wt% of a mixture of sorbent and catalyst particles (sorbent/catalyst = 9 g/g) with the aim of producing high purity hydrogen (>99.9 vol.%). It could be indicated that the mixing ratio of biomass and catalyst is, in a great extent, determined by practical demands.

Fluidization mainly depends on the bed pressure drop and the fluidization velocity. As shown in Fig. 2.17, when the fluid velocity is too small, the solid particles will remain on the bed. The phase between A and B is the fixed bed phase. When the gas velocity exceeds to the B phase, the bed pressure drop decreases slightly attributed to the loose arrangement of solid particles. Subsequently, the gas velocity continues to increase, whilst the pressure drop keeps constant and the bed height increases gradually. In this moment, the solid particles can float in the fluid and roll up and down with the gas movement, which is called the fluidized bed phase. When the gas velocity is higher than the E point, the fluid can take away the whole bed; consequently, the solid particles form the dilute phase in the state of suspension and are blown out. After the E phase, the normal fluidization state is broken, and the bed pressure drop decreases rapidly. Thus, the gas velocity in the point E is referred as the terminal or maximum fluidization velocity u_t.

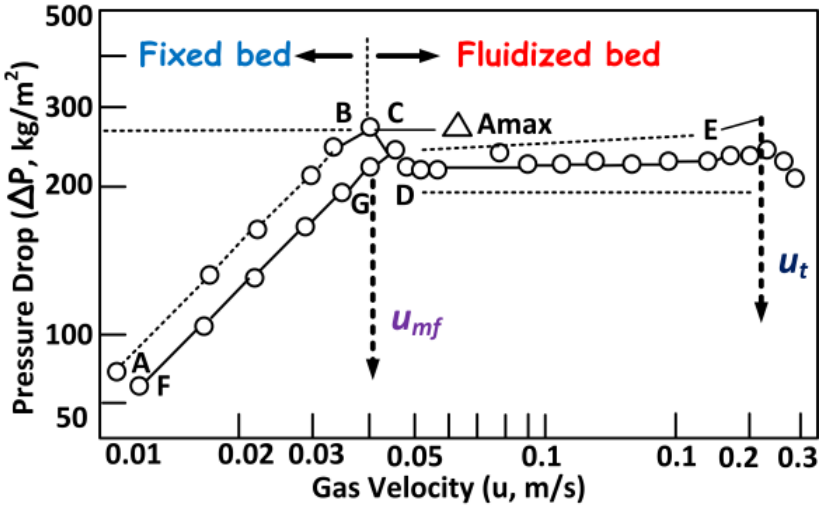

Figure 2.17 Effect of the gas velocity on the pressure drop in FBG

Qualitatively judging, the tendency of a particle to be carried away can be made by calculating the terminal velocity of a single particle u_t.

$$\phi = \frac{s}{S} \qquad \text{(E11)}$$

Where ϕ is the particle sphericity to account for particle shape, s is the surface of a sphere having the same volume as the particle and S is the actual surface area of the particle. In the previous study, a simple general correlation for predicting terminal velocities for isometric particles, given information on the particles and physical properties of the fluid, can be defined as the expressions E12-E15 [2-39].

$$u_t^* = \left[\frac{18}{(d_p^*)^2} + \frac{(2.335 - 1.744\phi)}{(d_p^*)^{0.5}} \right]^{-1} \qquad (0.5 \le \phi \le 1) \qquad \text{(E12)}$$

$$u_t^* = u_t \left[\frac{\rho_g^{\,2}}{g\mu_g(\rho_s - \rho_g)} \right]^{1/3} = \frac{\mathrm{Re}_{p,t}}{Ar^{1/3}} \qquad \text{(E13)}$$

$$d_p^* = d_p \left[\frac{g\rho_g(\rho_s - \rho_g)}{\mu_g^{\,2}} \right]^{1/3} = Ar^{1/3} \qquad \text{(E14)}$$

$$\mathrm{Re}_{p,t} = \frac{\rho_g d_p u_t}{\mu_g} \qquad \text{(E15)}$$

Where u_t is the terminal velocity of a particle in fluid (m/s), u_t* is the dimensionless particle velocity (m/s), d_p is the solid equivalent particle diameter (m), d_p* is the dimensionless particle diameter (m), $Re_{p,t}$ is the *Reynolds* number based on the equivalent spherical diameter of particle, ρ_g is the density of gas (kg/m^3), ρ_s is the density of solid particle (kg/m^3), μ_g is the viscosity of gas [kg/(m·s)], g is the acceleration due to gravity (9.81 m/s^2), and *Ar* is the *Archimedes* number.

If the fluidizing medium was dry air and the measurements were conducted at a temperature of 20±1 °C and the ambient pressure, the density and the dynamic viscosity of air could be estimated from the expressions E16 and E17 [2-40].

$$\rho_{\mathrm{g}} = 3.485\frac{P}{T} \qquad \text{(E16)}$$

$$\mu_g = 1.81\times10^{-5}(\frac{T}{293})^{0.66} \qquad \text{(E17)}$$

In general, the terminal fluidized velocity u_t can be calculated by the semi-empirical expressions E18-E20, if the *Reynolds* number is estimated. Additionally, the superficial gas velocity u_{mf} (m/s) at the minimum fluidization can be calculated by the empirical expression E21.

$$u_t = \frac{g{d_p}^2(\rho_s-\rho_g)}{18\mu},\ \mathrm{Re}_{p,t} \le 0.4 \qquad \text{(E18)}$$

$$u_t = [\frac{4}{225}\frac{g(\rho_s-\rho_g)^2}{\rho_g\mu}]^{\frac{1}{3}}d_p,\ 0.4 \le \mathrm{Re}_{p,t} \le 500 \qquad \text{(E19)}$$

$$u_t = [\frac{3.1gd_p(\rho_s-\rho_g)}{\rho_g}]^{\frac{1}{2}},\ \mathrm{Re}_{p,t} \ge 500 \qquad \text{(E20)}$$

$$u_{mf} = 0.695\frac{{d_p}^{1.82}(\rho_s-\rho_g)^{0.94}}{\mu^{0.88}{\rho_g}^{0.06}} \qquad \text{(E21)}$$

Mixtures of solid particles of different size and density tend to separate in the vertical direction

under the fluidized conditions. The non-uniform distribution of the different solid components is caused by a competitive action of mixing and segregation mechanisms. RH has very low bulk density (96-160 kg/m^3) with a very low terminal velocity u_t (1.0-1.4 m/s based on its physical properties) [2-41]. The fluidization characteristics of single RH could be observed from Fig. 2.18. When the superficial gas velocity u_g is smaller, the pressure drop increases with the increase of the superficial gas velocity u_g. However, the pressure drop decreases due to gas block caused by the formation of channeling and cavitas, when the superficial gas velocity u_g is increased to 0.27 m/s. Although the gas flow increases, most of bed materials keep stationary. Meanwhile, small amounts of RH particles are entrained from channeling to bed by gas, and thus the cavitas and channeling continue caving and forming. Even if the pressure drop trends to be keeping constant, the single RH particles cannot perform the fluidization behavior in the whole process.

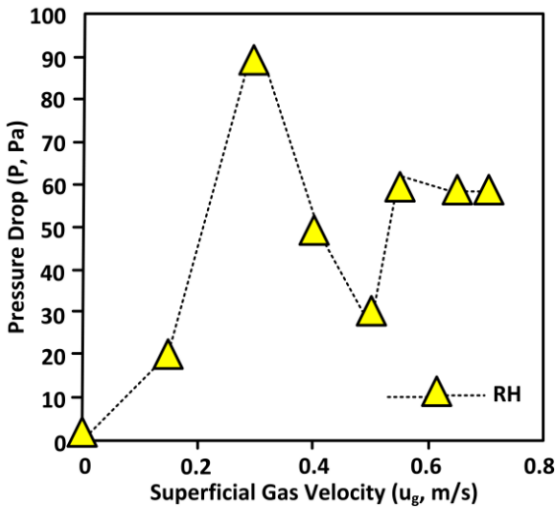

Figure 2.18 Characteristic curve of fluidization of single RH with the particle density of 950 kg/m^3 and the particle diameter of 2 mm

Rao and Ram [2-42] proved that it is difficult to fluidize single RH, and its fluidization behavior is improved by mixing with other solid particles (i.e., sand). The biomass constituted 2%, 5%, 10% and 15% determined by weight of the mixtures. The minimum fluidization velocity u_{mf} increased with the increase of the biomass mass fraction, as well as with increasing the sand density and the

particle size. It can be also observed in Fig. 2.19A that the bed pressure drop versus the superficial gas velocities is plotted with the aim of determining the minimum fluidization velocity u_{mf} of mixture, which is obtained from the intersecting point of the curve of a fixed bed at defluidization with the constant pressure line at the flow condition. Moreover, the minimum fluidization velocity u_{mf} can increase with the increase of the averaged mass fraction of RH, and decreases with the decrease of the sand particle size (Fig. 2.19B). The equivalent diameter of a sphere RH particle $d_{r,av}$ can be obtained by solving the *Ergun* equation (E22) at a given superficial gas velocity u_g [2-43]. Therefore, the appropriate particle size of RH can be obtained by measuring the pressure drop, in which the calculated equivalent diameter of RH particles is 1.54 mm.

$$\frac{\Delta P}{H} = 150\frac{(1-\varepsilon_g)^2 \mu_g u_g}{\varepsilon^3_g d^2_{r,av}} + 1.75\frac{1-\varepsilon_g}{\varepsilon^3_g}\frac{\rho_g}{d_{r,av}}u^2_g \qquad \text{(E22)}$$

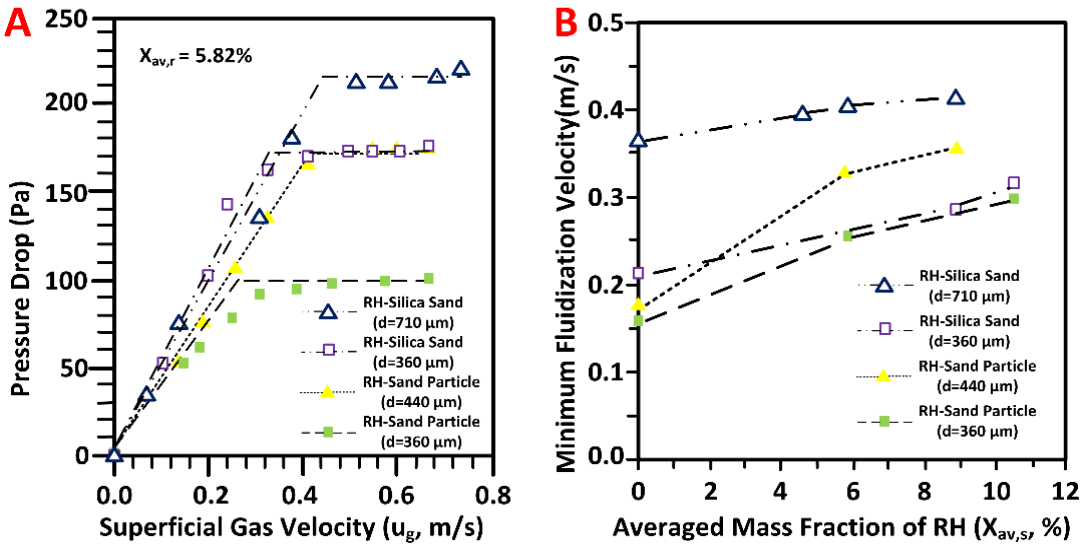

Figure 2.19 (A) Pressure drop of RH-sand and RH-silica sand binary mixture as a function of the superficial gas velocity; (B) Minimum fluidization velocity as a function of the mass fraction of RH particles. The density sand particles is 2600 kg/m^3 with the average diameters of 360 and 440 µm; the density of silica sand particles is 2700 kg/m^3 with the average diameters of 360 and 710 µm; the density of RH particles is 950 kg/m^3 with the average dimension of 10×2×1 mm.

As shown in Table 2.5, although the bulk density ρ_b of the mixed RHC/RHA is still low, its particle density ρ_p and particle diameter d_p are comparable to the sand particles. Moreover, the particle size of the RHA supported catalysts could be modified easier than sand particles. It is most likely that mixing with the RHA supported catalysts can improve RH fluidization behavior in FBG. Therefore, with the aim of implementing a fluidized state, it is necessary to simulate the particle sizes of RH and RHA in a static system of binary mixture. In this case, the fluidizing medium is assumed as dry air, carrying out at a temperature of 20 ± 1 °C under the ambient pressure, the gas density ρ_g and the dynamic viscosity μ_g could be estimated as 1.2 kg/m^3 and 4.26×10^{-5} kg/(m·s). In the BFB, when the biomass and inert particles are blended relatively homogeneous in a good fluidization state, the particle diameter along with the density of mixture can be normally calculated by the expressions E23 and E24, respectively. Consequently, the minimum fluidization velocity u_{mf} in the binary mixture of RH and RHA could be estimated by the expression E20. As shown in Fig. 2.20, it was found that decrease of both the mass fraction and the particle diameter of RH could increase the minimum fluidization velocity u_{mf} of the mixture, thereby improving the RH fluidization behavior. When the mass fraction of RH is increased to 0.5, the minimum fluidization velocity u_{mf} is increased dramatically (Fig. 2.20A). In contrast, when the particle size of RH exceeds 0.5 mm, the increasing trend of the minimum fluidization velocity u_{mf} declines (Fig. 2.20B). If the particle sizes of two components have large differences, the mixture could achieve a higher minimum fluidization velocity u_{mf} due to the strong segregation effect. Accordingly, when the superficial gas velocity u_g is too small, the high-density deposits (*i.e., RHA, sand*) would keep stable on the bed; whilst the low-density of RH can keep fluidization state. Therefore, the particle diameters of RH and RHA should employ the approximate sizes. Moreover, according to the experimental and simulated results, the mass fraction of 0.5 and the particle diameter of 0.5 mm can be selected for RH in this binary mixture, where the u_{mf} is 0.48 m/s.

$$\rho_P = \left[\frac{x_1}{\rho_{p,1}} + \frac{x_2}{\rho_{P,2}}\right]^{-1}, \quad x_1 = 1 - x_2 \qquad \text{(E23)}$$

$$d_P = \frac{x_1\rho_{P,2} + x_2\rho_{P,1}}{x_1\rho_{P,2}d_{P,2} + x_2\rho_{P,1}d_{P,1}} d_{P,1}d_{P,2} \qquad \text{(E24)}$$

Table 2.5 Properties of RH, RHA and sand

Properties		RH	RHA	Sand (250-595 µm)
Density (kg/m^3)	Bulk (ρ_b)	100	120-140	1460
	Particle (ρ_p)	950	2000	2430
Average particle diameter ($d_{av,r,}$ mm)		2	0.108	0.342
Bed voidage (ε)	1-(ρ_b/ρ_p)	0.9	0.93-0.94	0.40
Sphericity (ϕ)	Theoretical calculation	0.19	0.23-0.25	0.92
Minimum fludization velocity (u_{mf}, m/s)	Experimental (pressure drop plot)	-	0.06	0.09

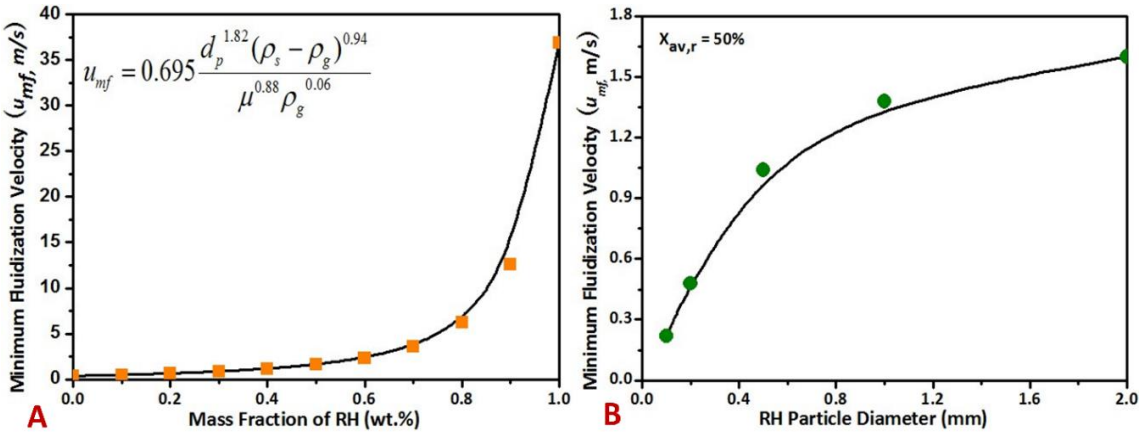

Figure 2.20 Effect of (A) mass fraction (RH particle diameter: 2 mm) and (B) particle diameter (RH mass fraction: 0.5) on the minimum fluidization velocity in the modeled binary mixture of RH and RHC

In summary, when the binary cocktail of RH and RHA supported catalysts was studied by the solid mixing-simulation, some hidden factors were not considered. In the instance, the metal or metal oxides in RHA were ignored, which contributes to the increase of the particle density; and the real

RH or RHA particles were non-uniform. Besides, the density of the solid particle was assumed that it would not change with the change of the particle diameter. In the actual situation, the density of a single particle should be calculated as the sum of all the discrete densities that are produced from the discretisation of the particle as it is illustrated in Fig. 2.21. The particle radius is discretised to N number of grid points numbered from k=0 to k=N, where 0 is the center of the particle, generating N discrete volumes. The density distribution along the particle radius is calculated by the discrete masses of the solid phases (i.e., biomass and char) corresponding to the specific discrete volume. The discrete masses of the solid phases are calculated using a linear approximation between two neighboring points that form a discrete volume, according to the mass fraction (ψ) in time of the specific phase. The discrete volumes (dV_k) and discrete mass (dm_k) are calculated by the equation (E25) and (E26), respectively.

$$dV_k = \frac{4}{3}\pi(r_k^{\,3} - r_{k-1}^{\,3}) \quad k = 1..., N \qquad \text{(E25), where } r_{k-1} = r_k - d_r$$

$$dm_k = \frac{(\psi_{k_w} + \psi_{k-1_w}) + (\psi_{k_c} + \psi_{k-1_c})}{2}\frac{m_p}{N} \quad k = 1..., N \qquad \text{(E26)}$$

Consequently, the discrete particle densities ($d\rho_{Pk}$) along with its radius and the total average particle density (ρ_{Pav}) are given by the equation (E27) and (E28), respectively. It can infer that the constant ρ_{Pav} changes with the change of V_p *and* m_p simultaneously. Herein, the above assumption of ρ_p versus d_p is rational. Furthermore, it is necessary to combine the experimental results in the large scale FBG with the simulated results to analyze in details these influencing factors. In addition, the ternary mixture of biomass, in terms of RHA and other solid particles (e.g., sand, dolomite), should be studied in order to cut down the expense of catalysts and bed materials.

$$d\rho_{P_K} = \frac{dm_k}{dV_k} \qquad \text{(E27)}$$

$$\rho_{P_{av}} = \frac{1}{N}\sum_{k=1}^{N} d\rho_{P_k} \qquad \text{(E28)}$$

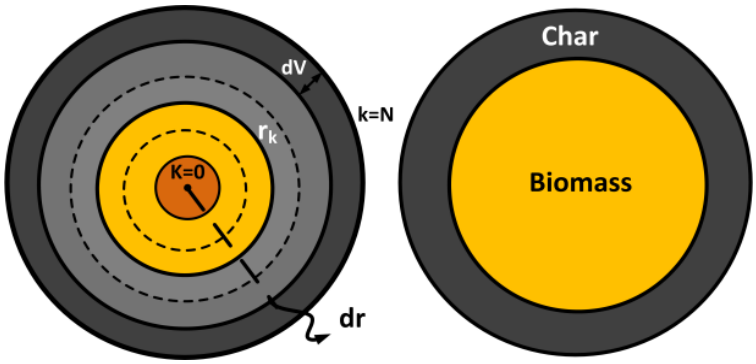

Figure 2.21 Schematic illustration of particle discretisation and discrete volume generation (left) and char formation during biomass pyrolysis (right)

2.4 Conclusions

A novel *in-situ* catalytic conversion of tar has been developed for biomass gasification. By means of co-pyrolysis with the RHC or RHA supported Ni-Fe catalysts, the tar yield and the CO_2 concentration significantly decreased in biomass gasification. In particular, the tar conversion efficiency could reach about 92.3% by co-pyroysis with the RHC Ni-Fe; accordingly, the light tar along with three- and four-ring aromatic organic compounds could significantly be transformed into single-ring organic compounds or smaller gas molecules. It is worth pointing out that partial metal oxides were transformed into metallic states via carbon and gas *in-situ* thermal reduction, thereby enhancing the catalytic activity, in terms of tar catalytic conversion. Meanwhile, a higher gas yield of 2.11 L/g could be achieved by co-pyrolysis with the RHC Ni-Fe attributed to char further devolatilization and tar conversion. Although the bimetallic RHC/RHA supported catalysts (i.e., RHA Ni-Fe, RHC Ni-Fe) exhibited a lower tar conversion efficiency compared to the monometallic RHA Ni, the expense of catalyst synthesis was much cheaper due to the low-concentration Ni used. Moreover, omitting the calcination step, the preparation procedure of catalysts became much convenient and energy saving. Without steam, the synergetic effects between the activation of tar on the nickel species and the oxygen atom supplied to the carbonaceous intermediate from neighboring iron atoms was not

displayed in the dry reforming. The char-supported catalyst (i.e., RHC Ni-Fe) is recommended to be employed for biomass gasification process in the absence or low oxygen. Reacting with enough oxygen agents at high temperatures, the char-supported catalysts could be easily consumed and deactivated, thereby possibly reducing their service life and increasing the CO_2 concentration in syngas. Nevertheless, the deactivated RHC Ni could be directly catalytically gasified to the additional syngas. Furthermore, by optimizing the operation parameters (e.g., particle size, mass fraction) in the mode of FBG, mixing with some solid particles (e.g., sand, RHA Ni) could improve the RH fluidization behavior. Consequently, the RH mass fraction of 0.5 and the particle diameter of 0.5 mm can be employed in the mixture of RH and RHA catalysts. Tar and char are the unexpected products in the process of biomass pyrolysis/gasification. Although activated chars are extensively applied as carbon-based adsorbents to deal with various pollutants such as heavy metal wastewaters, they have been rarely fabricated into the catalysts or supports for tar conversion. Subsequently, an integrated concept of sustainable route is proposed (Fig. 2.22) that chars including coal chars and biochars could be fabricated to the carbonaceous adsorbents for heavy metal wastewater/sludge treatment, accompanied by the production of char-supported catalysts for tar conversion.

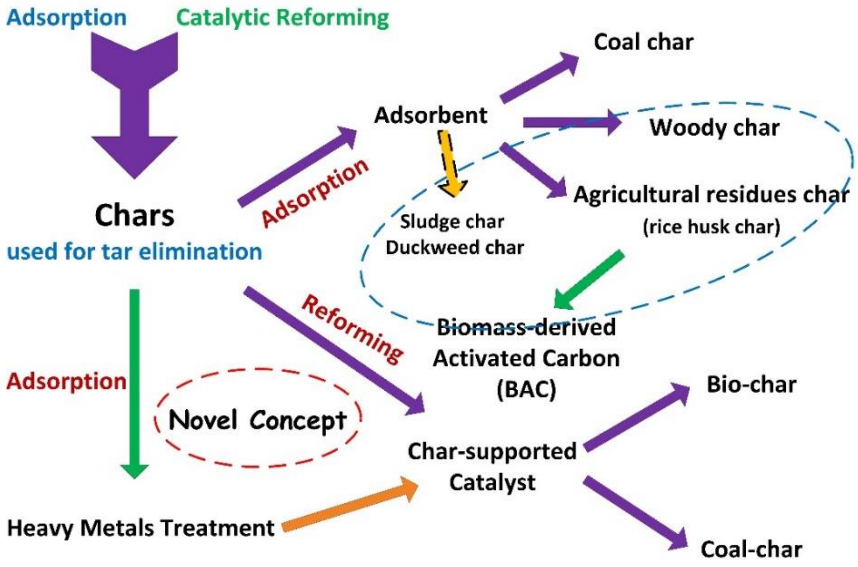

Figure 2.22 an integrated concept of chars used for adsorption and catalytic reforming of tar

References

[2-1] T. Matsuhara, S. Hosokai, K. Norinaga, K. Matsuoka, C-Z. Li, J-I. Hayashi, Rapid gasification of nascent char in steam atmosphere during the pyrolysis of Na- and Ca-ion-exchanged brown coals in a drop-tube reactor. *Energy Fuel* 2009, 24, 76-83.

[2-2] Z. Min, P. Yimsiri, M. Asadullah, S. Zhang, C-Z. Li, Catalytic reforming of tar during gasification. Part II. Char as a catalyst or as a catalyst support for tar reforming. *Fuel* 2011, 90, 2545-2552.

[2-3] Z. Min, S. Zhang, P. Yimsiri, Y. Wang, M. Asadullah, C-Z. Li, Catalytic reforming of tar during gasification. Part IV. Changes in the structure of char in the char-supported iron catalyst during reforming. *Fuel* 2013, 106, 858-863.

[2-4] Z. Min, M. Asadullah, P. Yimsiri, S. Zhang, H. Wu, C-Z. Li, Catalytic reforming of tar during gasification. Part I. Steam reforming of biomass tar using ilmenite as a catalyst. *Fuel* 2011, 90, 1847-1854.

[2-5] A. Uddin, H. Tsuda, S. Wu, E. Sasaoka, Catalytic decomposition of biomass tars with iron oxide catalysts. *Fuel* 2008, 87, 451-459.

[2-6] C. Li, K. Suzuki, Tar property, analysis, reforming mechanism and model for biomass gasification - An overview. *Renewable & Sustainable Energy Reviews* 2009, 13, 594-604.

[2-7] I. Narváez, J. Corella, A. Orío, Fresh tar (from a biomass gasifier) elimination over a commercial steam-reforming catalyst. Kinetics and effect of different variables of operation. *Industrial & Engineering Chemistry Research* 1997, 36, 317-327.

[2-8] D.M. Quyn, H. Wu, J-I. Hayashi, C-Z. Li, Volatilisation and catalytic effects of alkali and alkaline earth metallic species during the pyrolysis and gasification of Victorian brown coal. Part IV. Catalytic effects of NaCl and ion-exchangeable Na in coal on char reactivity. *Fuel* 2003, 82, 587-593.

[2-9] H. Wu, J-I. Hayashi, T. Chiba, T. Takarada, C-Z. Li, Volatilisation and catalytic effects of alkali and alkaline earth metallic species during the pyrolysis and gasification of Victorian brown coal. Part V. Combined effects of Na concentration and char structure on char reactivity. *Fuel* 2004, 83, 23-30.

[2-10] J. Schwan, S. Ulrich, V. Batori, H. Ehrhardt, S. Silva, Raman spectroscopy on amorphous carbon films. *Journal of Applied Physics* 1996, 80, 440.

[2-11] M. He, B. Xiao, Z. Hu, S. Liu, X. Guo, S. Luo, Syngas production from catalytic gasification of waste polyethylene: Influence of temperature on gas yield and composition. *International Journal of Hydrogen Energy* 2009, 34, 1342-1348.

[2-12] D. Li, Y. Nakagawa, K. Tomishige, Development of Ni-based catalysts for steam reforming of

tar derived from biomass pyrolysis. *Chinese Journal of Catalysis* 2012, 33, 583-594.

[2-13] C. Li, D. Hirabayashi, K. Suzuki, A crucial role of O_2 and O_2^{2-} on mayenite structure for biomass tar steam reforming over $Ni/Ca_{12}Al_{14}O_{33}$. *Applied Catalysis, B: Environmental* 2009, 88, 351-360.

[2-14] D. Wang, W. Yuan, W. Ji, Char and char-supported nickel catalysts for secondary syngas cleanup and conditioning. *Applied Energy* 2011, 88, 1656-1663.

[2-15] S. Dutta, C. Wen, R. Belt, *Industrial & Engineering Chemistry Process Design and Development* 1977, 16, 20-30.

[2-16] J.J. Pis, M. Mahamud, J.A. Pajares, J.B. Parra, R.C. Bansal, Preparation of active carbons from coal: Part III: Activation of char. *Fuel Processing Technology* 1998, 57, 149-161.

[2-17] S.V.B. van Paasen, Guideline for sampling and analysis of tar and particles in biomass producer gas, ECN-C-02-090, November 2002.

[2-18] Y. Chen, Y.C. Zhu, Z.C. Wang, Y. Li, L.L. Wang, L.L. Ding, et al. Application studies of activated carbon derived from rice husks produced by chemical-thermal process – A review. *Advances in Colloid and Interface Science* 2011, 163, 39-52.

[2-19] A. Karera, S. Nargis, S. Patel, M. Patel, Silicon-based materials from rice husk. *Journal of Scientific and Industrial Research* 1986, 45, 441.

[2-20] S. Chandrasekhar, P.N. Pramada, Rice husk ash as an adsorbent for methylene blue – effect of ashing temperature. *Adsorption* 2006, 12, 27-43.

[2-21] A. Paethanom, K. Yoshikawa, Influence of Pyrolysis Temperature on Rice Husk Char Characteristics and Its Tar Adsorption Capability. *Energies* 2012, 5, 4941-4951.

[2-22] Y.D. Yeboah, J.P. Longwell, J.B. Howard, W.A. Peters, Effect of Calcined Dolomite on the Fluidized Bed Pyrolysis of Coal. *Industrial & Engineering Chemistry Process Design and Development* 1980, 19, 646-653.

[2-23] C. Palma Font, A model for biomass gasification including tar formation and evolution. *Energy Fuels* 2013, 27, 2693-2702.

[2-24] C. Palma Font, Modeling of tar formation and evolution for biomass gasification: A review. *Applied Energy* 2013, 111, 129-141.

[2-25] C. Wu, P.T. Williams, Nickel-based catalysts for tar reduction in biomass gasification. *Biofuels* 2011, 2(4), 451-464.

[2-26] G. Guan, G. Chen, Y. Kasai, E.W.C. Lim, X. Hao, M. Kaewpanha, A. Abuliti, C. Fushimi, A. Tsutsumi, Catalytic steam reforming of biomass tar over iron- or nickel-based catalyst supported on calcined scallop shell. *Applied Catalysis B: Environmental* 2012, 115-116, 159-168.

[2-27] H. Liu, T. Chen, D. Chang, D. Chen, H. He, R.L. Frost, Catalytic cracking of tar derived from rice hull gasification over palygorskite-supported Fe and Ni. *Journal of Molecular Catalysis A: Chemical* 2012, 363-364, 304-310.

[2-28] H.P. Kuo, S.M. Pan, H.T. Hsu, Comparisons of the hydrogen-rich syngas compositions from wet rice husk slurry steam reforming reactions using different catalysts. *Biomass Bioenergy* 2011, 35, 3025-3031.

[2-29] Q. Xie, S. Kong, Y. Liu, H. Zeng, Syngas production by two-stage method of biomass catalytic pyrolysis and gasification. *Bioresource Technology* 2012, 110,603-609.

[2-30] F. Chang, M. Kuo, M. Tsay, M. Hsieh, Hydrogenation of CO_2 over nickel catalysts on rice husk ash-alumina prepared by incipient wetness impregnation. *Applied Catalysis A: General* 2003, 247, 309-320.

[2-31] J.D. Atkinson, M.E. Fortunato, S.A. Dastgheib, M. Rostam-Abadi, M.J. Rood, K.S. Suslick, Synthesis and characterization of iron-impregnated porous carbon spheres prepared by ultrasonic spray pyrolysis. *Carbon* 2011, 49, 587-598.

[2-32] T. Yamashita, P. Hayes, Analysis of XPS spectra of Fe^{2+} and Fe^{3+} ions in oxide materials. *Applied Surface Science* 2008, 254, 2441-2449.

[2-33] E.L. Kunkes, D.A. Simonetti, R.M. West, J.C. Serrano-Ruiz, C.A. Gärtner, J.A. Dumesic, Catalytic conversion of biomass to monofunctional hydrocarbons and targeted liquid-fuel classes. *Science* 2008, 322, 417-421.

[2-34] R. Cortright, R. Davda, J. Dumesic, Hydrogen from catalytic reforming of biomass-derived hydrocarbons in liquid water. *Nature* 2002, 418, 964-967.

[2-35] G.W. Huber, J. Shabaker, J. Dumesic, Raney Ni-Sn catalyst for H_2 production from biomass-derived hydrocarbons. *Science* 2003, 300, 2075-2077.

[2-36] Z. Abu El-Rub, E.A. Bramer, G. Brem, Experimental comparison of biomass chars with other catalysts for tar reduction. *Fuel* 2008, 87, 2243-2252.

[2-37] A. Gómez-Barea, B. Leckner, Modelling of biomass gasification in fluidized bed. *Progress in Energy and Combustion Science* 2010, 36, 444-509.

[2-38] J. Fermoso, F. Rubiera and D. Chen, Sorption enhanced catalytic steam gasification process: a direct route from lignocellulosic biomass to high purity hydrogen. *Energy & Environmental Science* 2012, 5, 6358-6367.

[2-39] A. Haider, O.Levenspiel, Drag coefficient and terminal velocity of spherical and nonspherical particles. *Powder Technology* 1989, 58, 63-70.

[2-40] M. Hartman, O. Trnka, K. Svoboda, Fluidization characteristics of dolomite and calcined dolomite particles. *Chemical Engineering Science* 2000, 55, 6269-6274.

[2-41] M. Rozainee, S.P. Ngo, A.A. Salema, K.G. Tan, M. Ariffin, Z.N. Zainura, Effect of fluidising velocity on the combustion of rice husk in a bench-scale fluidised bed combustor for the production of amorphous rice husk ash. *Bioresource Technology* 2008, 99, 703-713.

[2-42] T.R. Rao, J.V. Ram, Minimum fluidization velocities of mixtures of biomass and sands. *Energy*

2001, 26, 633-644.

[2-43] Q. Sun, H. Lu, Y. He, L. Yang, D. Gidaspow, Simulation and experiment of segregating/mixing of rice husk-sand mixture in a bubbling fluidized bed. *Fuel* 2005, 84, 1739-1748.

Chapter 3

Nickel Nanoparticles Generated in the Carbon Matrix of Rice Husk Char for *in Situ* Catalytic Conversion of Tar Derived from Biomass Gasification

3.1 Introduction

Biomass is an abundant and infinite source of chemically diverse macromolecules, including polysaccharides, polypeptides, and polyaromatics. Many of biopolymers are highly evolved for the specific functions via optimized chain length, functionalization, and monomer sequence. As biopolymers are a chemical source, much current effort has been focused on the breakdown of these molecules into fuels or platform chemicals. However, there is growing interest in using biopolymers directly to create functional materials [3-1]. Recently, some researchers found that the functionalized carbonaceous materials could be formed in the pyrolysis of lignocellulosic biomass by adjusting the pyrolysis temperature [3-2], [3-3]. It is envisioned that a conceptually method can be developed for *in situ* growth of carbon fibers by catalytically reducing and depositing certain volatile low-molecular-weight organic compounds on the carbonaceous skeletons. Besides, the morphology and properties of as-prepared carbon composites could be tunable via deliberated adjustment of temperature and selection of catalysts. Subsequently, Liu et al. [3-4] proposed a new approach to synthesize the magnetic nanofiber/mesoporous carbon composites in one-pot by catalysis of lignocellulosic biomass with $FeCl_3$. The schematic and mechanism are illustrated in Fig. 3.1.

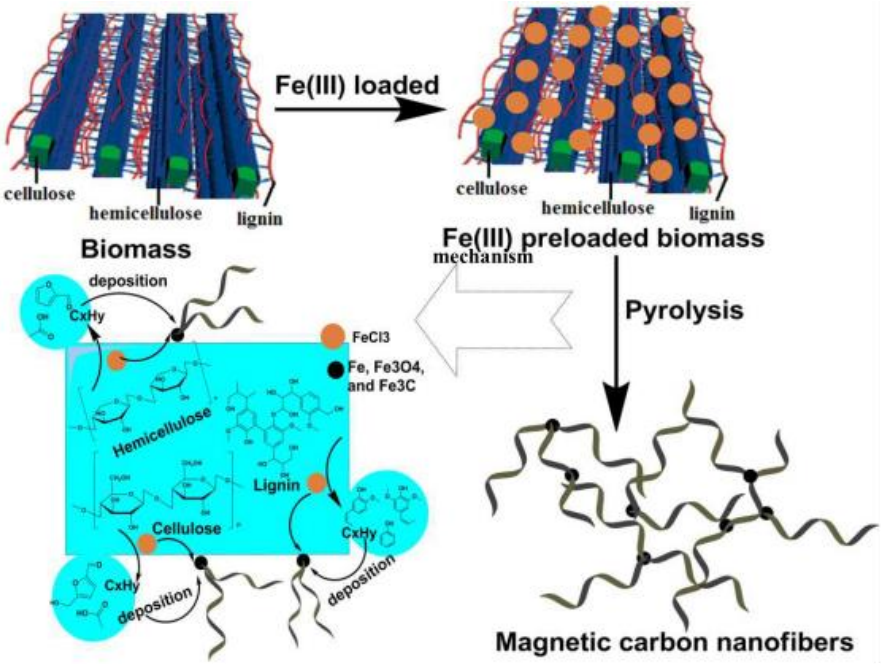

Figure 3.1 Schematic and mechanism illustration of the synthesis of the magnetic carbon nanofiber from the lignocellulosic biomass [3-4]

Many fundamental works have been studied on the addition of metallic species to biomass by impregnation with metal salts solutions, which could explain the role of minerals during biomass pyrolysis [3-5], [3-6], [3-7], [3-8], [3-9], [3-10], modify the primary pyrolysis and increase the selectivity towards one or more specific products [3-7], [3-8], [3-9], [3-10], [3-11], [3-12], [3-13], [3-14], [3-15]. It is well known that the presence of inorganic species dispersed in the biomass, can influence pyrolysis behavior and the distribution of pyrolysis products. Additionally, the type of nickel-biomass interactions with the nickel species evolution during biomass pyrolysis in relation to the extent of primary and secondary pyrolysis reactions are thus of great importance in the final catalytic results of biomass pyrolysis in the presence of a nickel salt as a catalyst precursor [3-16]. In the last chapter, it has been proved that partial metal oxides in the biochar can be reduced into the metallic state by co-pyrolysis with biomass. The purpose of the current work is to provide a thorough fundamental understanding of the nanoscale complex physicochemical and catalytic mechanisms involved in a novel integrated biomass catalytic gasification process. Consequently, the metal nickel

nanoparticles could be *in situ* generated in the carbon matrix of rice husk char, which is further studied for tar catalytic conversion in the following-up biomass gasification. Additionally, rice husk as s sustainable biomass source presents the mircoporous structure. In this study, rice husk would be directly employed as a carbon source for rice husk char supported catalysts preparation via one-step pyrolysis.

3.2 Experimental

3.2.1 Properties of Raw and Pre-treated Rice Husk (RH) Samples

RH was pre-impregnated with the nickel nitrate solutions [$Ni(NO_3)_2{\cdot}6H_2O$, *Wako, Ltd., Japan*] as the nickel precursor. It can be concluded that the increase of the nitrogen content was attributed to the adsorption of $Ni(NO_3)^+$ and ammonium NH_4^+ cations present in the solution, along with the possible adsorption of NO_3^- anions. Besides, the hydrogen content in the nickel impregnated RH decreased possibly due to the deprotonation of the oxygenated surface groups necessary for the adsorption of the Ni^{2+} species [3-16], while the slight increase of the hydrogen content was attributed to the hydrogenation by the strong reducing property of BH_4^- or H_2 actives from $NaBH_4$ hydrolysis. Fig. 3.2 illustrates the biomass pretreatment by the incipient wetness impregnation of nickel nitride with $NaBH_4$ modification. It could be observed that $NaBH_4$ was hydrolyzed rapidly, when it was added into the nickel solution (Fig. 3.2B). Large amounts of generated gas bubbles might contribute to the more pores formation (i.e., mesopores, micropores), thereby enhancing the adsorption performance of RH for Ni^{2+} according to the chemical reactions (R1-R9). After impregnation and isothermally drying at 105 °C, the pretreated RH samples (i.e., RH, RH Ni and RH Ni-B) were dry-stored for further use. In addition, the organic functional groups of RH samples were investigated by the fourier transform infrared spectroscopy (*FT-IR, JIR-SPX200, JEOL, Japan*) before and after the pyrolysis. Subsequently, the residual chars derived from RHs pyrolysis were characterized by the X-ray diffraction (*XRD, D8*

Discover, Bruker AXS, Germany), the X-ray photoelectron spectroscopy (*XPS, Physical Electronics, USA*) and the transmission electron microscopy coupled with the energy dispersive spectroscopy (*TEM-EDS, JEM-2010F, JEOL, Japan*), respectively.

$5Ni(NO_3)_2 + 24H_2O \rightarrow Ni^{2+} + 4[Ni(H_2O)_6]^{2+} + 10NO_3^-$	(R1)
$[Ni(H_2O)_6]^{2+} \rightarrow Ni(OH)_2 + 2H_3O^+ + 2H_2O$ (*thermal decomposition)*	(R2)
$Ni(OH)_2 \rightarrow NiO + H_2O$	(R3)
$BH_4^- + x\ Ni^{2+} \rightarrow Ni_xB\ (x = 1\text{-}3) + 2H_2\uparrow$	(R4)
$BH_4^- + 2Ni^{2+} \rightarrow Ni_2B\downarrow$ (*black precipitate*) $+ 2H_2\uparrow$	(R5)
$BH_4^- + 2H_2O \rightarrow BO_2^- + 4H_2\uparrow$ (*Ni_2B catalytic hydrolysis*)	(R6)
$Ni^{2+} + 2BO_2^- \rightarrow Ni(BO_2)_2$	(R7)
$3Ni(BO_2)_2 + 2Ni_2B \rightarrow 7Ni^0$ (*polymolecularity*) $+ 4B_2O_3$	(R8)
$Ni^{2+} + H_2 \rightarrow Ni^0 + 2H^+$ (*Ni_2B catalytic hydrogenation*)	(R9)

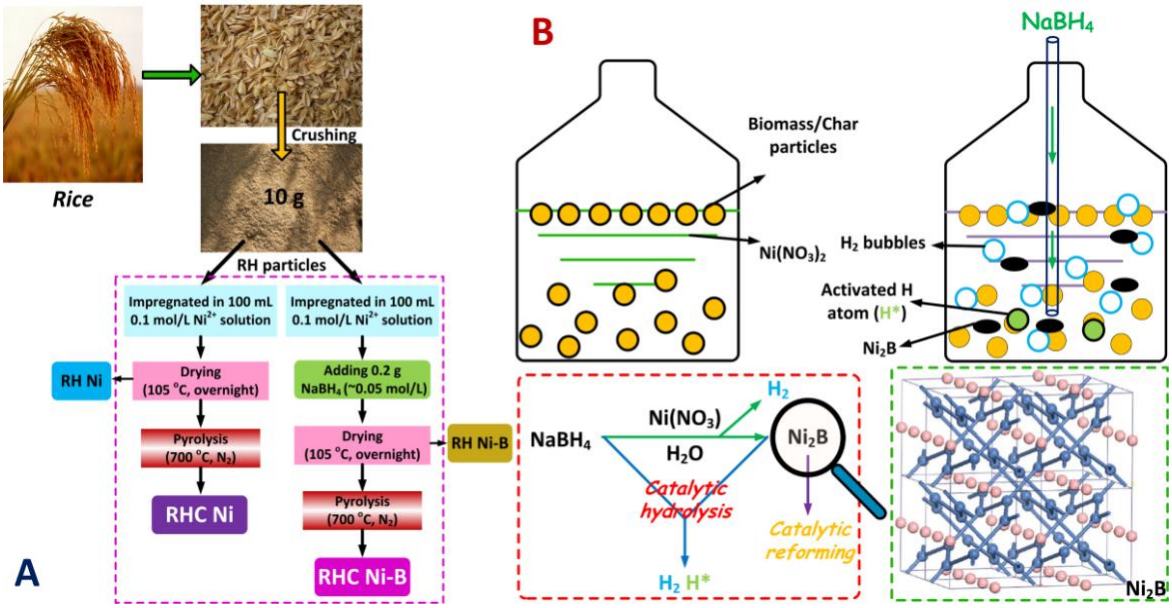

Figure 3.2 Schematic diagrams of (A) RH impregnated with $Ni(NO_3)_2$ and (B) pre-treated by $NaBH_4$

3.2.2 RHC Ni Catalysts Preparation

RHC was prepared by the pyrolysis at 700 °C in the nitrogen atmosphere. The procedures of catalysts preparation are illustrated in Fig. 3.3. In general, RHC Ni catalysts were prepared by the incipient wetness impregnation with one-step pyrolysis using $Ni(NO_3)_2 \cdot 6H_2O$ as a nickel precursor. Initially, the RH was impregnated with nickel ions under the atmospheric pressure and isothermally dried at 105 °C. Then, the dry-based RH Ni was completely pyrolyzed at 700 °C in the inert gas (e.g., N_2). Subsequently, the RHC Ni1 and the RHC Ni2 can be obtained by collecting the solid residues (i.e., biochar). The RHC Ni3 and the RHC Ni4 can be directly obtained via the nickel ions wet-impregnation and drying of RHC. It is noted that the RHC Ni2 and RHC Ni4 catalysts were treated by $NaBH_4$ before drying. After impregnated and dried in an oven at 105 °C, the dry RHC-supported catalysts were prepared and stored for further use. The metal ions adsorption capacity of char mainly depends on the preparation methods and conditions, such as char surface characteristics (e.g., surface area, pore size), impregnation temperature, metal ion type. As shown in Table 3.1, the total amounts of nickel contents are different among these RHC Ni catalysts, which correspond to the BET surface areas and pore volumes. In addition, the average crystallite diameter of nickel nanoparticles was around 2 nm.

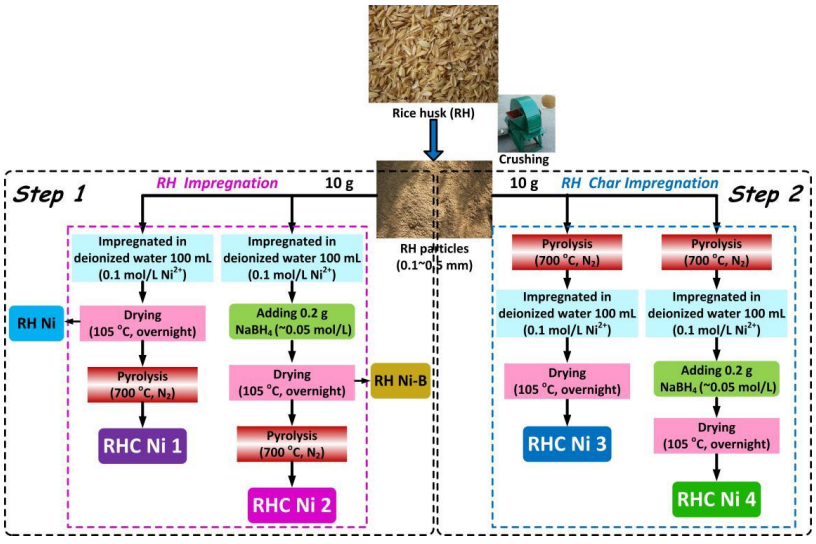

Figure 3.3 Different procedures of RHC Ni catalysts preparation

Table 3.1 Characteristics of the As-prepared RHC Ni Catalysts

Catalysts	S_{BET} (m^2/g)	Ni content (mg/g)	d_{XRD} [a] (nm)	Pore Volume (cm^3/g)
RHC Ni1	135	51.90	1.50	0.46
RHC Ni2	218	49.37	2.14	0.53
RHC Ni3	87	55.20	1.72	0.43
RHC Ni4	62	54.68	2.14	0.50

[a] Average crystallite size calculated by *Scherrer equation* according to the Ni (111).

3.2.3 Biomass Pyrolysis

The experimental setup is illustrated in the section 2.2.3. The feedstock of RH was prepared by crushing and sieving with the particle size below 5.0 mm.

Experiment 1:

Initially, the reactor temperature was heated up to 700 °C. Then, the inert carrier gas (i.e., N_2) with a flow rate of 1.0 L/min was continuously injected into the reactor to blow away the residual gases in the entire system. As 10 g of the pre-treated biomass sample (i.e., RH, RH Ni) was fed into the pyrolyzer, the volatile matters of it could be rapidly released in the forms of syngas and tar. By means of the heat in the gasification zone, biomass tar could be *in-situ* catalytically cracked and transformed into the small-molecular gases by the thermochemical reactions.

Experiment 2:

In this study, biomass (RH, 10 g) mixed with the fresh catalyst (RHC Ni, 1-10 g) was co-pyrolyzed in the reactor for tar *in-situ* conversion. Before starting the gasification experiment, the reactor was heated up to 800 °C. As the prepared RH sample is fed into the pyrolyzer, the volatile matters were released in the forms of gases and nascent tars. Tar could be cracked into the small molecular gases by co-pyrolysis with the RHC Ni catalysts.

3.2.4 Sampling and Analysis

The sampling and analytical methods were performed according to the section 2.2.4.

3.3 Results and Discussions

3.3.1 Products from the Untreated and Treated RH Pyrolysis

The product yields of RHs pyrolysis are shown in Table 3.2. The increase of the yield of solid residues (i.e., char) can be ascribed to the decrease of volatiles and the increase of nickel cation. In addition, high conversion efficiency of the condensable tar could be achieved by 96.9% (RH Ni) and 98.6% (RH Ni-B) via the pretreatment by nickel nitrate impregnation and sodium borohydride modification, respectively, corresponding to the color appearances of the condensates. It should be noted that the condensable tar is transformed into the non-condensable tar, improving the fuel characteristics (e.g., heating value) of producer gas in favor of the power generation systems. However, compared to the raw RH and RH Ni-B, RH Ni can yield more syngas after pyrolysis. The reason is most likely that, on one hand, the removed tar was converted into the additional gases by thermochemical reactions (i.e., cracking, reforming) with the catalytic effect of nickel; on the other hand, the nickel catalyst could enhance the pyrolysis efficiency and restrain the formation of macromolecular tar due to the polymerization. Furthermore, the syngas properties got improved by nickel impregnation and $NaBH_4$ modification. H_2 volume concentration was remarkably increased from 17.3% to 47.6%; accordingly, the volume concentration ratio of H_2 and CO (i.e., H_2/CO) increased from 0.44 to 1.28. Moreover, the slight decrease of CH_4 and CO_2 might be attributed to the heterogeneous and the homogeneous reactions (R10-R22) via nickel catalysis [3-17], [3-18]. Without injecting steam (H_2O), the water gas shift (WGS) reaction (R16) was not effective, so the ratio of H_2/CO was still lower for chemical synthesis. Besides, the low heating value (LHV) of syngas was estimated by the empirical expression increasing from 10.25 to 11.32 MJ/m^3. It suggests that the nickel nitrate impregnation

and $NaBH_4$ modification is an effective pretreatment route to achieve tar *in-situ* catalytic conversion in biomass gasification.

Biomass → $CO + H_2 + CO_2 + CH_4 + H_2O + C_nH_m$ + Tar (C_xH_y, $C_xH_yO_z$) + Char	(R10)
$C_nH_m \rightarrow nCO + (m/2)H_2$	(R11)
$C_nH_m + nH_2O \rightarrow nCO + (m+2n)/2H_2$	(R12)
$C_nH_m + nCO_2 \rightarrow 2nCO + m/2H_2$	(R13)
$C_nH_m \rightarrow nCO + (m/2)\ H_2$	(R14)
$CH_4 + 0.5O_2 \rightarrow CO + 2H_2$ ΔH = -36 kJ/mol	(R15)
$CO + H_2O \rightarrow CO_2 + H_2$ ΔH = -41 kJ/mol	(R16)
$CH_4 \rightarrow C + 2H_2$ ΔH = +75 kJ/mol	(R17)
$C_nH_m \rightarrow nC + (m/2)H_2$ ($2 \leqslant n \leqslant 4$)	(R18)
$C + H_2O \rightarrow CO + H_2$ ΔH = +131 kJ/mol	(R19)
$C + CO_2 \rightarrow 2CO$ ΔH = +172 kJ/mol	(R20)
$CH_4 + H_2O \rightarrow CO + 3H_2$ ΔH = +206 kJ/mol	(R21)
$CH_4 + CO_2 \rightarrow 2CO + 2H_2$ ΔH = +247 kJ/mol	(R22)

Table 3.2 Products from RH, RH Ni and RH Ni-B Pyrolysis at 700 °C

	RH	RH Ni	RH Ni-B
Pyrolysis Products Yields (mg/g)			
Char	325.3	368.3	392.0
Tar [a]	86.5	2.7	1.2
Gas [b]	588.2	629.0	606.8
Syngas Composition (vol.%)			
CO	39.5	34.2	37.1
H_2	17.3	38.6	47.6
CH_4	9.5	6.4	4.2
CO_2	25.0	18.4	10.3
≥C2 [c]	8.7	2.4	0.8
H_2/CO	0.44	1.13	1.28
LHV (MJ/m^3) [d]	10.25	10.77	11.32

[a] The condensable tar derived from RH pyrolysis at 700 °C. [b] The producer gas estimated by the difference includes the non-condensable tar and other impurities. [c] By difference.

[d] $\mathrm{LHV}(kJ/m^3) = [30(CO) + 25.7(H_2) + 85.4(CH_4)] \times 4.2$

3.3.2 Characterization of RHs

3.3.2.1 Thermogravimetric (TG) analysis

TG analysis of three RH samples (~10 mg) was investigated at the 20 °C/min heating rate to a final temperature of 800 °C with a hold time of 10 min, using nitrogen as a carrier gas. With the rise in temperature, the weight loss of the sample was continuously recorded. This raw data was used to calculate TG and differential TG (DTG) curves as shown in Fig. 3.4A. Obviously, the main weight loss occurs between 250 and 550 °C due to the devolatilization, especially in terms of mass loss around 300 °C according with the decomposition of cellulose/hemicellulose/lignin, while the mass loss in a temperature range of 350-550 °C corresponds to the biochar decomposition [3-19]. Compared to RH Ni and RH Ni-B, the RH initially tended to decompose at a lower temperature with a relatively lower rate, most likely producing more condensable tar. When the heating temperature increased to 500 °C or above, the pyrolysis efficiency can be improved by adding $NaBH_4$. From the DTG curves,

it is clearly observed that the maximal devolatilization rate could be decreased through the nickel nitrate impregnation. However, $NaBH_4$ modification can improve the maximal devolatilization rate compared to the onefold nickel used. Fig. 3.4B shows the TG and DTG curves of the solid RHC samples (i.e., RHC, RHC Ni and RHC Ni-B) derived from RHs pyrolysis at 700 ^{o}C. When the heating temperature was below 400 ^{o}C, RHC can be kept much stable. The higher moisture content of RHC indicated that it can easily adsorb water from the surroundings because of its hydrophily. Thereby, it means that the temperature range of 400-500 ^{o}C could be chosen for thermal regeneration of the RHC Ni catalysts using the waste heat in the pyrolyzer. After that, the weights of them were slightly reduced with a constant rate. RH Ni and RH Ni-B showed a similar decomposition rate, which is higher than the decomposition rate of raw RH in the range of 600-800 ^{o}C (Fig. 3.4C). It might be caused by the further decomposition of residual volatiles and the carbon reaction of char (e.g., *Boudouard reaction*). When the heating temperature increased up to 800 ^{o}C, the weight of RHC can keep constant. The lower weight loss ratio of RHC Ni-B can be ascribed to the high devolatilization efficiency in the primary pyrolysis phase. The devolatilization rate can also be enhanced by the nickel impregnation. Thus, it means that the addition of sodium borohydride might modify the chemical structures of organic functional groups in biomass, improving the gasification efficiency.

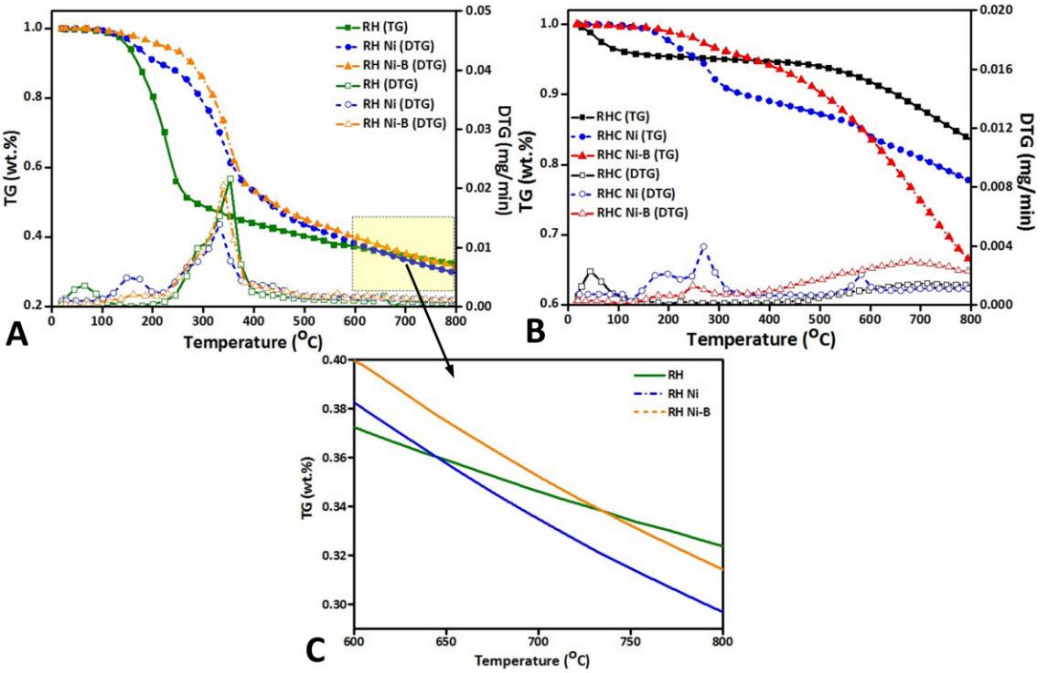

Figure 3.4 TG and DTG curves of (A) RHs and (B) RHCs under the nitrogen condition

3.3.2.2 FTIR analysis

The FTIR spectra of three RHs are shown in Fig. 3.5. It is well known that the typical components of biomass are cellulose, hemicellulose and lignin, so their typical functional groups and the IR signal with the possible compounds are similar [3-20], [3-21]. It can be observed that three RH samples are composed of acid, methanol, alkyl, aliphatics, aromatics and ketone with different oxygenated functional groups, e.g., O-H (3500-3200 cm^{-1}), -C=O (1735-1727 cm^{-1}, 1670-1630 cm^{-1}), COO^- groups in carboxylate (1400-1310 cm^{-1}), C-O-C (1250-1270 cm^{-1}, 1170 cm^{-1}), and C-O-(H) (1050 cm^{-1}), etc. The oxygen-free organic functional groups (e.g., hydrocarbons), such as $-CH_3/-CH_2-$ (2990-2850 cm^{-1}), O=C=O (2410-2280 cm^{-1}), benzene rings in the aromatic organic compounds (1515-1485 cm^{-1}), benzene derivatives (890-805 cm^{-1}, 580-420 cm^{-1}) can also be detected in RHs (Fig. 3.5A). After pre-treated by Ni and Ni-B, the absorption peaks assigned to some organic functional groups in RH were changed obviously, such as COO^- groups in carboxylic acid salts (1400-1310 cm^{-1}, symmetrical strech), Si-O-Si (1100-1000 cm^{-1}, anti-symmetrical strech), while majority of the organic functional groups had small changes (Fig. 3.5B), which indicated that the pretreatment mildly destroyed the chemical

structures of macromolecular organic functional groups in RHs. Significantly, the absorption peaks of several organic functional groups in RH, e.g., C-N-C in amines (407 cm^{-1}), rings in the benzene derivatives (580, 569, 558 and 520 cm^{-1}), disappeared after pretreatment by $NaBH_4$. In addition, the disappeared peaks of the sulfur-containing functional groups in RH, such as C-S (600 cm^{-1}, strech) (Fig. 3.5C), most likely were caused by the reductive sulfur removal due to the strong reducibility of $NaBH_4$ [3-22]. It can imply that the $NaBH_4$ modification is considerable to treat the high-sulfur fuels, thereby inhibiting the catalysts sulfur deactivation [3-23]. However, the IR absorption peak of C-OH in alcohol (669 cm^{-1}, bending) was enhanced probably due to the partial hydrolysis of lignin, etc. Organic functional groups in RHs mainly distribute in the range of 2000-400 cm^{-1}. In particular, Fig. 3.5D reveals some obvious changes in the range of 1800 and 1200 cm^{-1}. These spectra modifications mainly concerned the C=O and C-O bonds associated with the carboxyl function of the 4-O-methy-glucuronic the acid units of xylan (decreased intensities of the stretching bands for C=O bond in aldehydes at ~1735 cm^{-1} and -OH bond in carboxylic acids at ~1423 cm^{-1}, and increased intensities of the symmetrical (υ_s) and anti-symmetrical (υ_{as}) stretching bands for $(O\text{-}C\text{=}O)^-$ bond of the carboxylic acid salts at ~1385 and 1342 cm^{-1}). The stretching bands for $(O\text{-}C\text{=}O)^-$ bond of the carboxylate seemed to increase proportionally with the nickel content, which effectively confirmed that these bands were associated with the presence of nickel in RH. Furthermore, the $\Delta\upsilon$ between the two stretching modes υ_s and υ_{as} (< 43 cm^{-1}) suggested intense coordination of the bidentate chelate type between the nickel and the carboxylate group [3-16]. Therefore, it clearly shows that the carboxylic acid functions of the hemicelluloses can play the role of ligands in the forming the coordination complexes bonded with the nickel cation. In general, the adsorbed nickel cation in the pretreated biomass exists mainly in the two forms. On one hand, the nickel cations disperse at the outer surface of the lignocellulosic matrix by the hydrogen-bond interaction under the atmospheric impregnation; on the other hand, the nickel cations present in the inner sphere by the bidentate chelate interaction (Fig. 3.6)

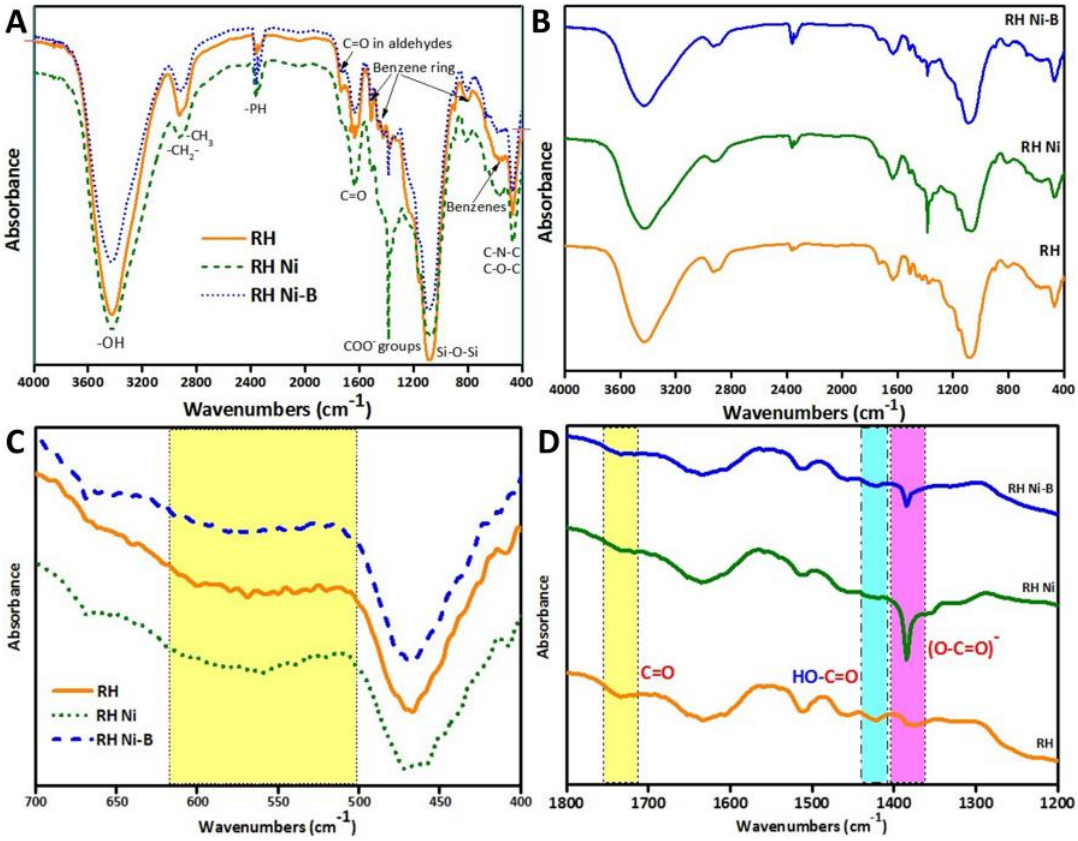

Figure 3.5 FTIR spectra of RH, RH Ni and RH Ni-B

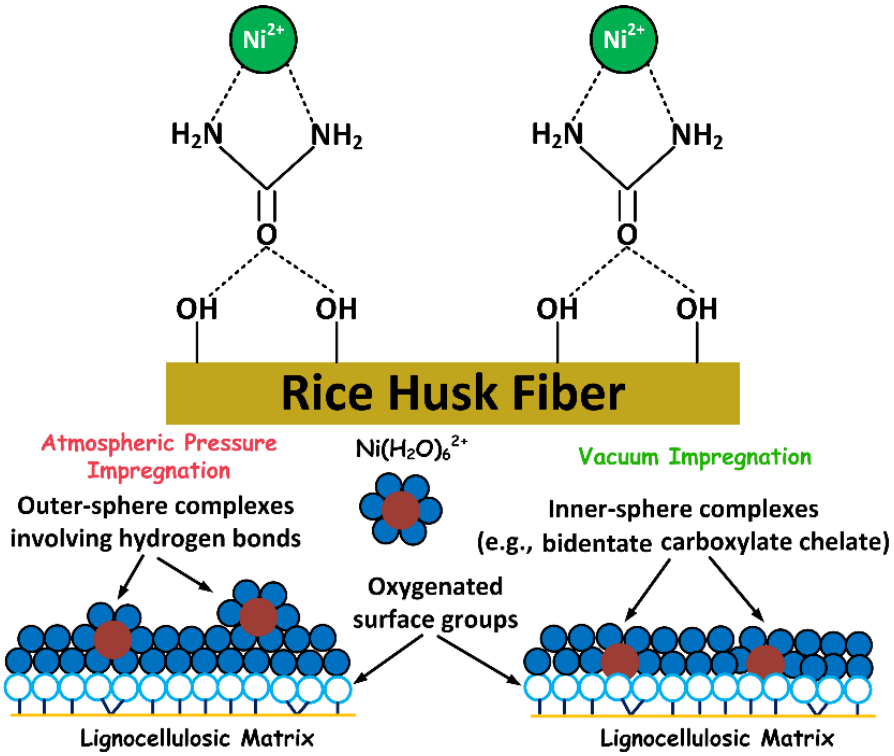

Figure 3.6 Two modes of nickel cation in the lignocellulosic matrix of biomass

Besides, biomass pretreatment by means of nickel nitrate impregnation and $NaBH_4$ modification has other functions, such as ion exchange, deoxygenation, hydrogenolysis and carbon chains formation. As shown in Fig. 3.7, the IR adsorption peaks of $-(CH_2)_n-$ in hydrocarbons bands between 740-720 cm^{-1} appeared by adding the $NaBH_4$. It means that $NaBH_4$ modification can mildly break the carbon structures of macromolecular organic hydrocarbon compounds (e.g., cellulose, hemicellulose, lignin) into the $-(CH_2)_n-$ rocking in the long chains at the hot alkaline condition [3-24]. However, the hydrolysis is not thoroughly without enzymatic saccharification [3-25]. Therefore, the formation mechanism of long hydrocarbon chains by $NaBH_4$ modification can be proposed as follows (Fig. 3.7). These long-chain hydrocarbons were unstable and easily decomposed through the thermochemical reactions contributing to the improvement of the devolatilization efficiency. It should be noted that the polymolecularity Ni^0 could be generated possibly due to the disproportionated reaction and the strong reducing property of $NaBH_4$ (R6 and R7).

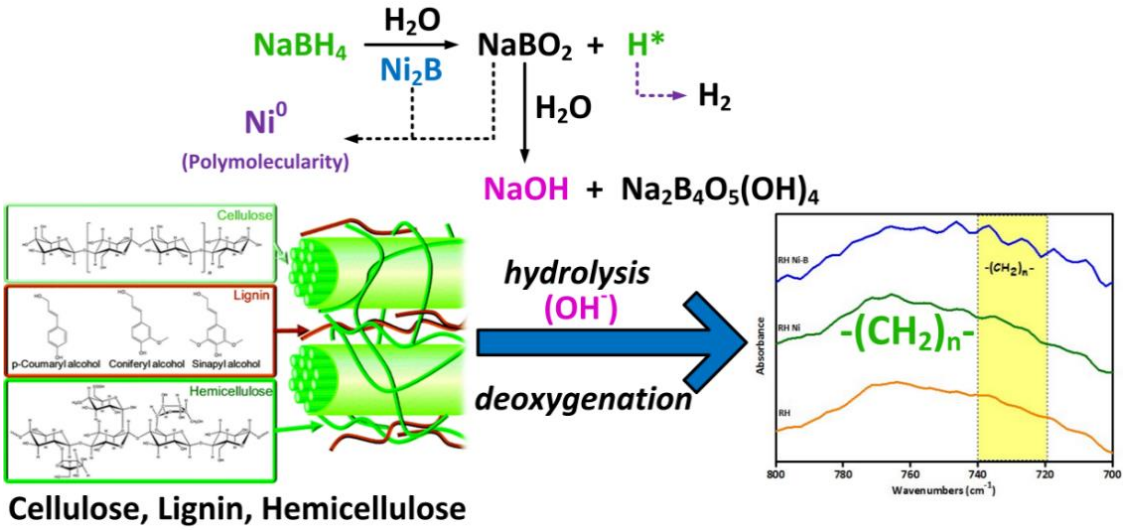

Figure 3.7 Possible mechanism of long-chain hydrocarbons formation by $NaBH_4$ modification

3.3.3 GC-MS Analysis of Tar

The most important and abundant organic compounds are styrene, phenol and naphthalene, which have been identified as the main tar compounds derived from pyrolysis of wood samples. Lu et al.

[3-26] also found that benzene derivatives, phenol derivatives, alkanes, cycloalkanes and aromatic hydrocarbons were the main compounds in the bio-oils from RH fast pyrolysis at lower temperature. In this research, the main organic compounds in the condensed tar from RH pyrolysis at 700 °C existed in the forms of 1- or 2-ring aromatic hydrocarbon compounds (i.e., benzene, naphthalene) and oxygenated aromatic compounds (i.e., phenols). In addition, only small amounts of PAHs, e.g., phenanthrene, had been detected. It is caused by the higher pyrolysis and reforming temperature without causing the polymerization reactions. It is noteworthy that with the nickel impregnation, the absorption peak intensities of tar compounds derived from RH pyrolysis significantly decreased or disappeared. As shown in Table 3.3, it could be found that after pyrolysis of RH Ni and RH Ni-B, the macromolecular aromatics (e.g., phenanthrene) significantly reduced in tar, mainly consisting of naphthalene and phenol derivates (e.g., 2-Ethyl-phenol). It can be concluded that these tar compounds were more difficult to be transformed compared to other tar compounds, such as phenol, indene, and benzene. In summary, this catalytic pyrolysis technology can greatly inhibit the small molecules polymerization, thereby reducing the follow-up macromolecular tar formation.

Table 3.3 Identified Organic Compounds in the Collected Tar from RHs Pyrolysis at 700 °C

Residence Time (min)	Main Identified Compounds	Molecular Formula	Concentration (%)		
			RH	RH Ni	RH Ni-B
3.483	5-(2-Amino-2-carboxyethyl)-2-hydroxybenzoic acid	$C_{10}H_{11}NO_5$	4.77	3.14	5.41
4.375	Naphthalene	$C_{10}H_8$	5.13	-	-
4.8	Benzene	C_6H_6	7.69	2.33	2.3
6.958	Naphthalene	$C_{10}H_8$	37.37	26.11	9.61
8.05	Phenol	C_6H_6O	5.45	-	-
8.758	3-Methyl-1,2-cyclopentanedione	$C_6H_8O_2$	7.72	26.59	12.16
9.342	Indene	C_9H_8	5.93	-	-
9.8	Methyl-phenol	C_7H_8O	1.9	-	1.53
10.283	Acenaphthalene	$C_{12}H_8$	3.07	-	-
10.717	Biphenylene	$C_{12}H_8$	3.34	-	-
10.808	2-Methyl-benzofuran	C_9H_8O	1.98	-	-
11.008	2-Ethyl-phenol	$C_8H_{10}O$	2.39	16.76	17.41
12.217	Methyl triacetic lactone	$C_7H_8O_3$	0.64	-	-
12.967	2,3,6-Trimethyl-phenol	$C_9H_{12}O$	1.91	-	-
13.025	4-Ethyl-2-methyl-phenol	$C_9H_{12}O$	1.62	7.84	8.02

14.508	3-Methyl-1,2-benzenediol	$C_7H_8O_2$	2.4	-	-
14.833	Indenol	C_9H_8O	5.45	3.18	2.48
17.208	Naphthalenol	$C_{10}H_8O$	2.15	2.24	1.8
19.7	Fluoranthene	$C_{16}H_{10}$	5.64	-	-
20.45	Trimethylsilyl 2,6-bis[(trimethylsilyl)oxy]benzoate	$C_{16}H_{30}O_4Si_3$	2.42	1.52	1.19
22.758	Phenanthrene	$C_{14}H_{10}$	3.32	1.32	-
24.3	3-Methylhenicosane	$C_{22}H_{46}$	1.77	-	-
24.475	Octadeamethyl-cyclononasiloxane	$C_{18}H_{54}O_9Si_9$	1.98	1.46	1.02
25.892	Benzoic acid, 2,6-bis[(trimethylsilyl)oxy]-, trimethylsilyl ester	$C_{16}H_{30}O_4Si_3$	1.91	0.93	3.12
26.65	Tetradecane	$C_{14}H_{30}$	4.8	-	-
27.108	N-Cholestan-4-ylacetamide	$C_{29}H_{51}NO$	2.4	0.86	-
28.367	Trimethylsilyl 2,6-bis[(trimethylsilyl)oxy]benzoate	$C_{16}H_{30}O_4Si_3$	2.46	-	-
29.958	Benzenamine	$C_{28}H_{43}N$	2.33	0.88	-

Note: - means undetected

3.3.4 Characterization of RHC Ni and RHC Ni-B

3.3.4.1 XRD analysis

RH is composed of a variety of components such as lignin (20-30%), cellulose (55-65%) and silica (15-20%). As above, lignin and cellulose can be transformed into the applicable energy products (e.g., syngas), whilst the silica in RHs has a potential for further research targeting more valuable applications (e.g., lithium battery anodes) [3-29]. The amorphous silica in RHs has developed the unique porous nanostructures through years of natural evolution [3-30]. It can be clearly observed that RHC exhibits a broad silica (SiO_2) at around $2\theta=22.5^o$, representing the characteristic peak of amorphous silica (Fig. 3.8A). In addition, the high-purity of silica (~94.64% in RHA) resulting from the thermal treatment alone is substantially higher than those of the other silica resources, such as quartz, zeolites, which are prepared by similar procedures. In this research, RHC produced from RH pyrolysis was further investigated as a carbon-based catalyst for tar conversion. Fig. 3.8B shows the X-ray diffraction (XRD) patterns of RHC Ni and RHC Ni-B. The characteristic peaks of amorphous silica (SiO_2) can be clearly observed. It is noteworthy that the main chemical states of nickel in RHC Ni was

mainly in the forms of nickel oxides (e.g., bunsenite) and metallic nickel (Ni^0) corresponding to the reactions (1)-(3). Initially, the Ni^{2+} cations in the aqueous solution were transformed to the relative stable form of $Ni(H_2O)_6^{2+}$ (i.e., octahedral water coordination complexes) [3-16], and subsequently decomposed into NiO by means of the thermochemical reactions. The partial metallic nickel (Ni^0) is preliminary generated through *in-situ* reduction by reducing gases (e.g., CO, H_2) and carbon sources (i.e., C) during the pyrolysis process (R23-R29) [3-31]. However, the characteristic peaks of NiO disappeared, whilst the chemical state of nickel was the metallic nickel (Ni^0) in the RHC Ni-B. It is suggested that $NaBH_4$ reduction can reduce NiO into the Ni^0, enhancing the tar conversion efficiency. Indeed, the active phase of the nickel-based catalysts for the hydrocarbon cracking (R28) and the reforming reactions (e.g., R29), particularly methane (CH_4) catalytic reforming, is the metallic nickel (i.e., Ni^0) [3-32]. Besides, it has been reported that the XRD peak shifting and broadening might indicate the changes of crystal structure, for instance, the enlargement or shrink of crystal cells, due to the interaction between crystals [3-33]. It can be seen that the characteristic peaks of amorphous SiO_2 in RHC slightly shifted to the left (lower angle) in both the RHC Ni and the RHC Ni-B; Likewise, the metallic nickel (Ni^0) characteristic peaks at 51.64° and 76.23° in the RHC Ni-B shifted to the left compared to the Ni^0 characteristic peaks at 51.67° and 76.52°, respectively, possibly indicating the enlargement of SiO_2 and Ni^0 crystal cells in RHC Ni. Conversely, the Ni^0 strong characteristic peak at 44.45° in RHC Ni-B slightly shifted to the right (higher angle) compared to the Ni^0 characteristic peak at 44.43° in RHC Ni, indicating the shrinkage of the Ni^0 crystal cells.

$Ni_xO_yH_z + xC \rightarrow Ni_x + (2x-y)CO + (y-x)CO_2 + (z/2)H_2$	(R23)
$Ni_xO_yH_z + xC \rightarrow Ni_x^0 + xCO_{(ads)} + (y-x)OH_{(ads)} + (z-y+x)H_{(ads)}$	(R24)
$NiO + C \rightarrow Ni + CO$	(R25)
$NiO + CO \rightarrow Ni + CO_2$	(R26)
$NiO + H_2 \rightarrow Ni + H_2O$	(R27)

$C_xH_yO_z \rightarrow zCO + (y/2)H_2 + (x\text{-}nz)C$	(R28)
$C_xH_yO_z + H_2O \rightarrow xCO + (x+y/2\text{-}z)H_2$	(R29)

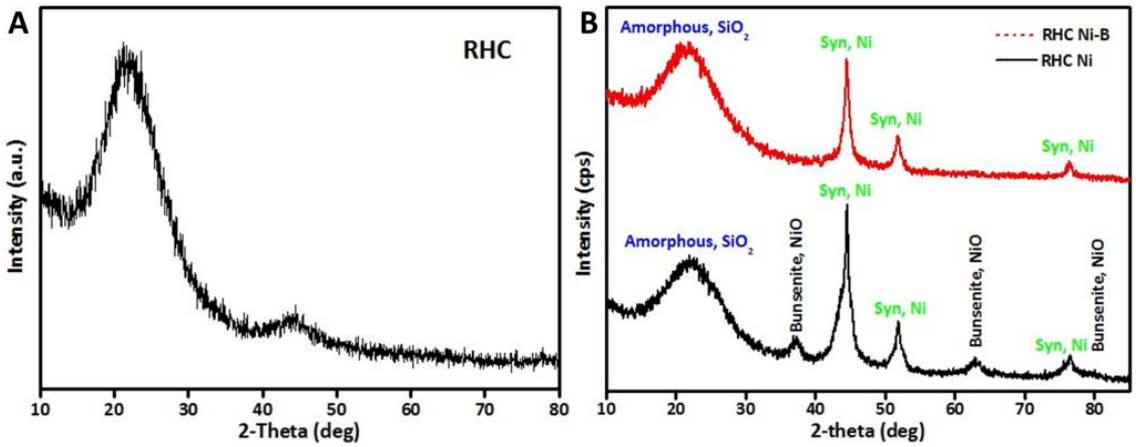

Figure 3.8 XRD curves of (A) raw RHC, (B) RHC Ni and Ni-B

3.3.4.2 TEM Analysis

It has been proved that the metallic nickel (Ni^0) nanoparticles, which were dispersed uniformly in the carbon matrix, were undetected in the wood char obtained at pyrolysis temperatures from 500 to 700 °C. However, the very wide dispersion of the monocrystalline metallic nickel (Ni^0) particles with the particle size of 2-4 nm could form at the pyrolysis temperatures from 400 to 500 °C and their nanometric size confirmed the highly dispersion of the metal precursor in the wood obtained after the process of impregnation [3-16]. Fig. 3.9 shows the TEM photographs of RHC Ni. It can be observed remarkably that most of metallic nickel (Ni^0) particles with the particle size of 10-20 nm dispersed uniformly, possibly attributed to the coagulation with the nanosized amorphous silica or the encapsulation in the carbon matrix. Ni^0 nanoparticles with smaller sizes can also be obtained probably by using an impregnation method favoring high dispersion of Ni^{2+} species on the carbon matrix of RHC. Furthermore, other elements distributed around the pointed nickel nanoparticle, such as Mg, Si, K, Ca, can be detected as similar as the chemical components in the ash. In addition, the TEM-EDS semi-quantitative result of RHC Ni is shown in Fig. 3.10. Undoubtedly, it can be found

that nickel, silicon and carbon were the main elements in the RHC Ni. It can be concluded that nickel nanoparticles may present in the form of polymolecularity Ni^0 or conglutinated with the crystalline silica in the carbon matrix of RHC.

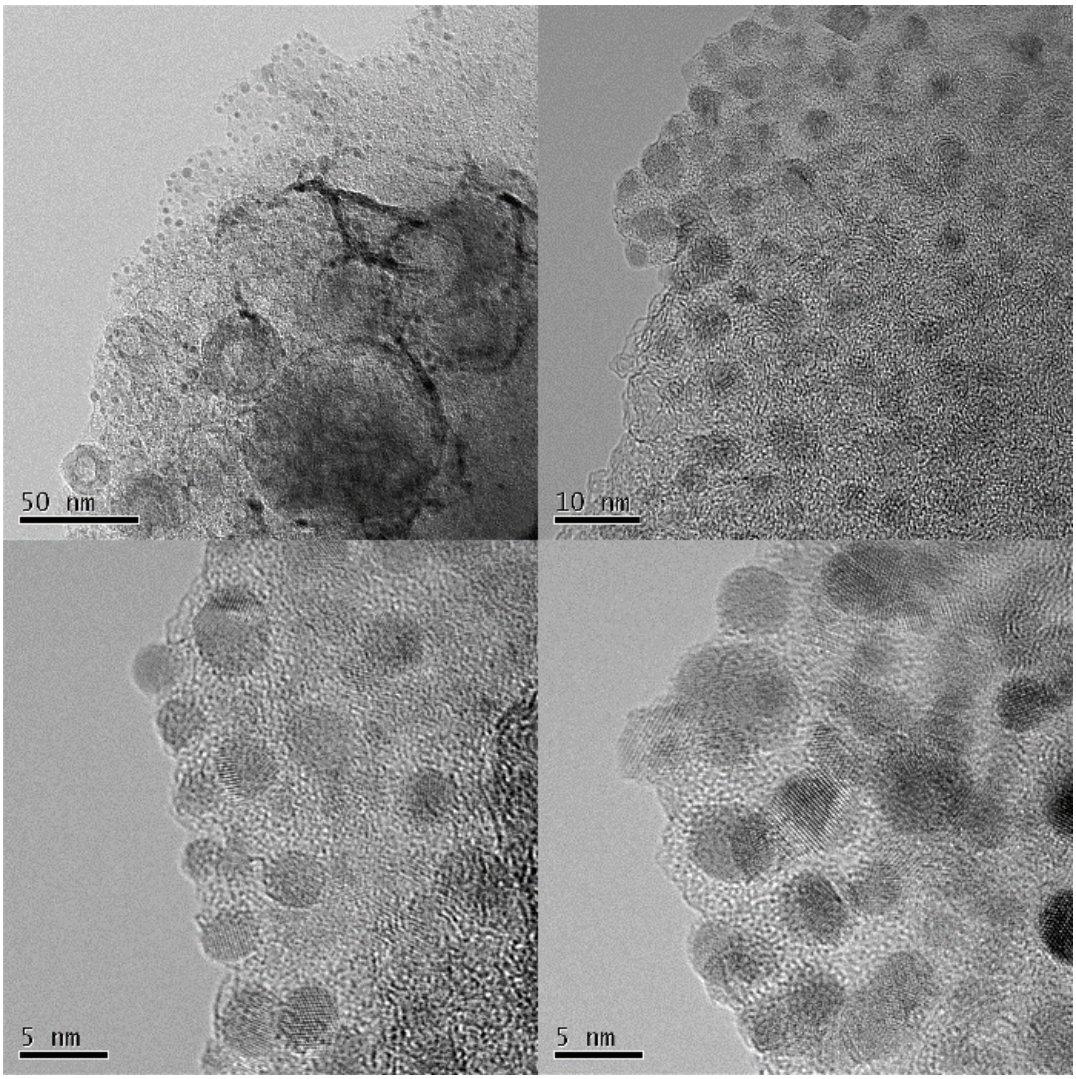

Figure 3.9 TEM photographs of RHC Ni with different magnification times

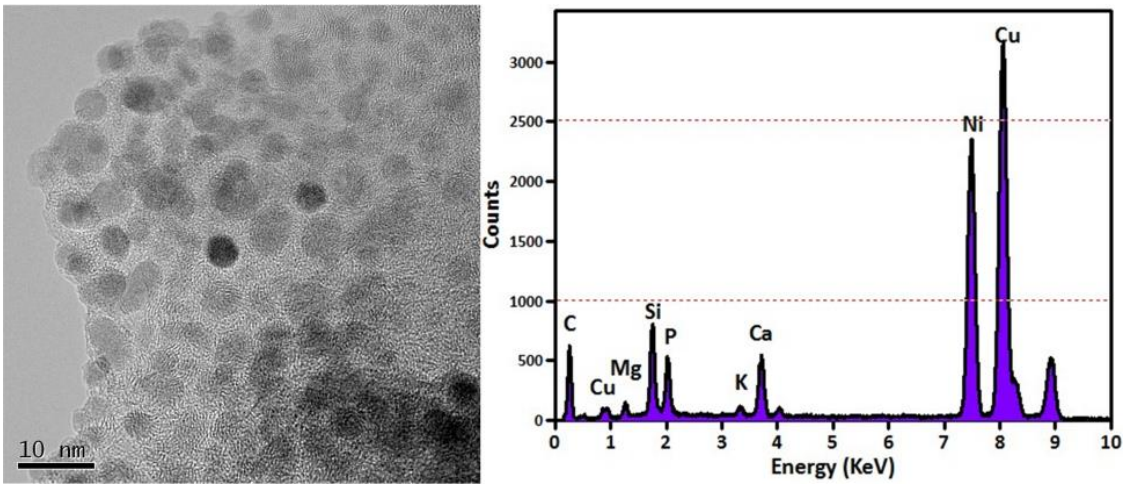

Figure 3.10 TEM image with the EDS analysis of RHC Ni at 200 kV

3.3.5 Catalytic Performances of RHC Ni and Ni-B

Biomass or biochar with porous structure could be employed in wastewater treatment for removing for heavy metal (e.g., Ni). Consequently, it is highly recommended to employ the pyrolytic biochar (i.e, RHC, RHC Ni, and RHC Ni-B) as a carbon-based catalyst for the tar conversion. In addition, the produced char-Ni^0 nanocomposite could be activated or be directly gasified into the applicable syngas. Fig. 3.11 shows the tar yields from RH co-pyrolysis with the RHC catalysts at 700 °C. It can be found that RHC itself showed catalytic activity for tar conversion. Klinghoffer et al. [3-34] proved the minerals and/or metals such as iron in the polar wood char are most likely playing a role in the hydrocarbons catalytic cracking reactions. After used for the catalytic reactions, carbon deposition would occur on the iron clusters and the pores of the char surface influencing the catalytic activity. Char derived from pyrolysis/gasification provides a high surface area support for ash, which is already impregnated in the char, thereby producing a supported metal catalyst. Thus, it has been proved that the char supported catalysts continuously generated on-site in the pyrolysis/gasification process, have a potential to replace expensive tar decomposition catalysts. If raw RH was mixed with the RHC Ni and RHC Ni-B, the condensable tar could be significantly removed by 96.5% and 92.6%, respectively. Nevertheless, the catalytic performance shows a slight decrease compared to the directly pyrolysis of RH Ni and RH Ni-B, implying that the addition of $NaBH_4$ can enhance the tar

conversion and upgrade the vapor during the RH Ni-B pyrolysis, but the solid residues of RHC Ni-B showed a slight inferior of catalytic performance, especially in terms of the tar conversion. One main reason may also be ascribed to the mass ratio decrease of nickel particles. It is noted that the RHC Ni exhibited a comparable tar conversion efficiency compared to the directly pyrolysis of RH Ni.

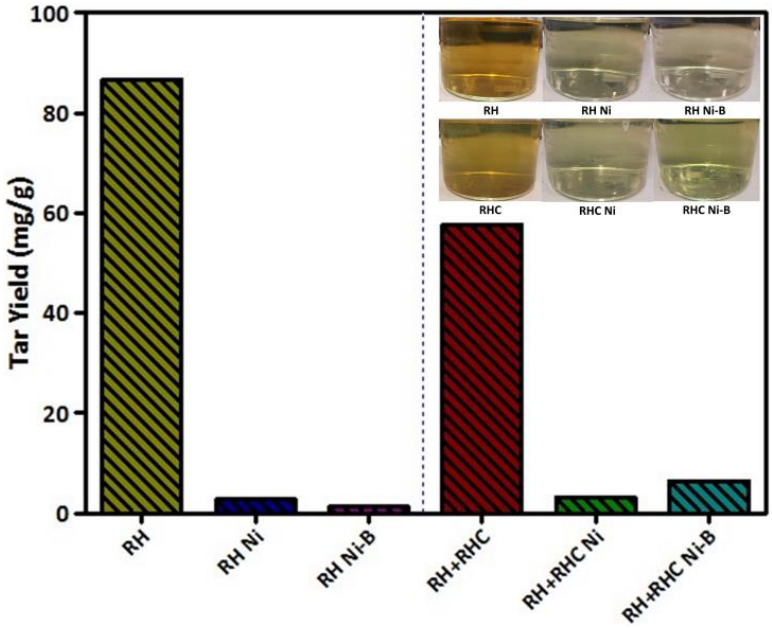

Figure 3.11 Tar yields from RH co-pyrolysis with RHC Ni and Ni-B (mass ratio: 1) at 700 ^{o}C

3.3.6 Characterization of RHC Ni Catalysts

3.3.6.1 Nitrogen adsorption-desorption isotherms

Fig. 3.12 shows the nitrogen adsorption-desorption isotherms of the RHC and RHC Ni catalysts. They present a combination of types I and IV according to the IUPAC classification [3-35], showing the characteristics of microporous and mesoporous structures. Raw RHC is characterized by the type IV adsorption isotherm, resulting from the surface coverage of mesoporous walls followed by pore filling associated with various hysteresis loops. At the relative lower pressure (P/P_0) values, the isotherms shape is analogous to the type II isotherm but at P/P_0 values above 0.4, pore condensation will be taking place, indicating porous structure of RHC. Similarly, at P/P_0 values above 0.4, the isotherms show the apparent hysteresis loops, possibly caused by a capillary condensation in the

mesoporous structures of the RHC Ni1, RHC Ni2 and RHC Ni4. However, the isotherm of RHC Ni3 displays a sharp knee at the P/P_0 value of 0.01, and the plateau is nearly horizontal. This adsorption behavior indicates that the pore structure of the RHC Ni3 is mainly microporous, with a narrow pore size distribution. It can be concluded that the nickel cations are easily adsorbed in the mesopores resulting in the main microporous structures of RHC Ni3. Moreover, the pretreatment and activation could change the pore structures and produce more new mesopores in the RHC, enhancing the adsorption performance, such as RHC Ni2 and RHC Ni4 treated by $NaBH_4$. It might be attributed to the RHC wet activation in the hot alkaline environment [3-36], corresponding to the reported works that the NaOH-treated RH can be transformed into mesoporous activated carbons [3-36], [3-37].

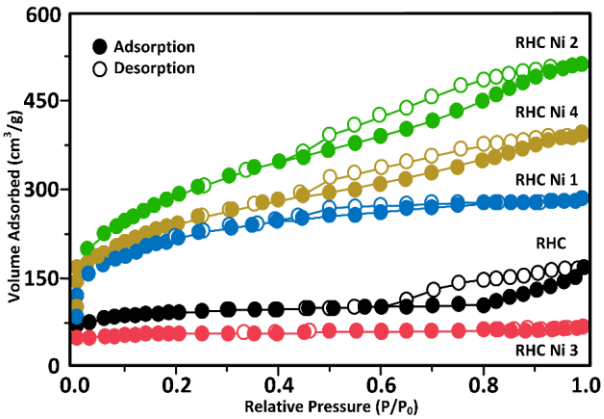

Figure 3.12 Nitrogen adsorption-desorption isotherms at 77 K of RHC and RHC Ni catalysts

3.3.6.2 TG analysis

TG analysis of the RH, RHC and RHC Ni catalysts (~10 mg) was investigated at the 20 °C/min heating rate to a final temperature of 800 °C with a hold time of 10 min, using nitrogen as a carrier gas. With the rise in the temperature, the mass loss of the sample was continuously recorded. This raw data was used to calculate TG as shown in Fig. 3.13A. It showed that the main mass loss occurs between 250 and 550 °C due to the further devolatilization, especially in terms of mass loss around 300 °C in accord with cellulose/holocellulose/lignin degradation, while the mass loss between 350-550 °C corresponds to the biochar further decomposition [3-19]. Compared with the RH Ni and RH Ni-B,

RH preliminary tended to decompose at a lower temperature, possibly resulting in more biomass tar formation. When the heating temperature increased to 500 °C or above, the pyrolysis efficiency of RH can be improved by adding small amounts of $NaBH_4$. TG data of the RHC and RHC Ni catalysts showed a continuous mass loss associated with increasing the temperature (Fig. 3.13B), which was ascribed to the breaking of chemical linkages and removal of volatile matters from biochar [3-38]. Moreover, the TG analyses of the RHC Ni catalysts were obviously different from the result of RHC, most likely due to promoting the catalytic effect of nickel on the char decomposition. Furthermore, as the temperature increased, the mass losses of RHC Ni3 and RHC Ni4 were higher than the RHC Ni1 and RHC Ni2. On one hand, RH Ni and RH Ni-B were significantly decomposed in the first stage, accordingly producing the RHC Ni1 and RHC Ni2. On the other hand, the chemical activity of metal cations (e.g., Ni^{2+}) encapsulated in the carbon matrix of char could chelate the oxygen-containing functional groups and change the thermal degradation process [3-38].

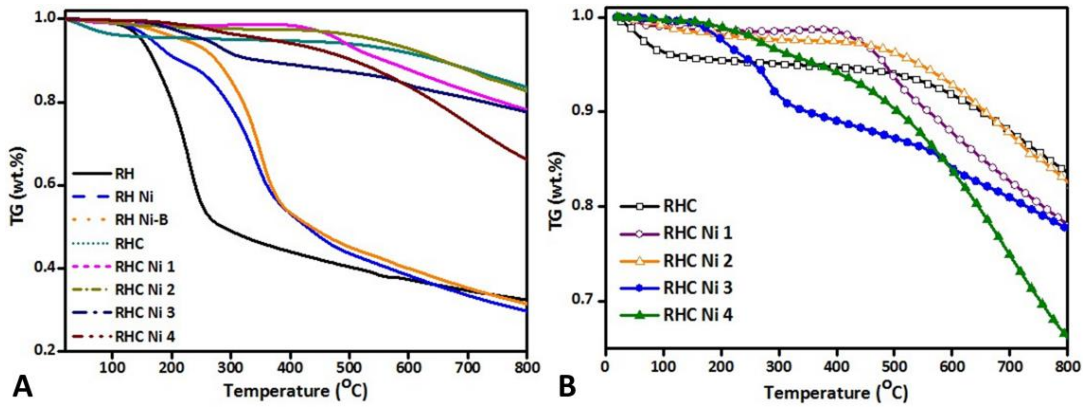

Figure 3.13 TG curves of (A) RHs and (B) RHC catalysts under the nitrogen condition

3.3.6.3 XRD analysis

The identification of crystal phases was performed by XRD using Rigaku D/Max 3400 powder diffraction system with Cu Kα radiation (λ = 0.1542 nm) at 45 kV and 200 mA with a scanning rate of 5°/min. Fig. 3.14 shows the XRD patterns of the RHC and RHC Ni catalysts. As shown in Fig. 3.14A, an obvious strong peak at 2θ = 22.5° appearing in RHC was a characteristic peak of amorphous silica

corresponding to the presence of cristobalite. Besides, a weak characteristic peak at 2θ = 44.3° normally indicated the formation of a turbostratic structure of amorphous carbon [3-39], [3-40]. The characteristic peaks of amorphous SiO_2 can be clearly observed as well in the RHC Ni catalysts. It suggests that RHC, indeed, could play as the role of a relatively stable catalyst support because of its high silica content (Fig. 3.14B). Table 3.4 lists the XRD characteristic peaks of the RHC Ni catalysts. The main chemical state of nickel in the RHC Ni1 catalysts were in the forms of nickel oxides (e.g., NiO, bunsenite) and metallic nickel (Ni^0). And the partial metallic nickel (Ni^0) in the RHC matrix may be generated via *in-situ* reduced by reducing gases (e.g., CO, H_2) or carbon atoms during the process of pyrolysis in the absence of oxygen [3-41], [3-42]. Since the co-pyrolysis was conducted with no additional oxygen source in the form of O_2 or H_2O, the Ni^0 and oxygen sources can be generated from the NiO deoxidization in RHC. Some metal oxides, such as nickel oxides, cerium oxides, and iron oxides, as the oxygen carriers have a potential to contribute to the partial gasification reactions as oxygen sources. Moreover, nickel oxides are the most reducible among them [3-42]. However, the characteristic peaks of bunsenite (NiO) disappeared, whilst the chemical status of nickel was in the form of Ni^0 (*syn.*) in the RHC Ni2 and RHC Ni4. It is concluded that $NaBH_4$ as a strong reducing agent could reduce the nickel oxides (e.g., NiO) into the metallic nickel (i.e., Ni^0), thus enhancing the catalytic activity of nickel on the tar reforming.

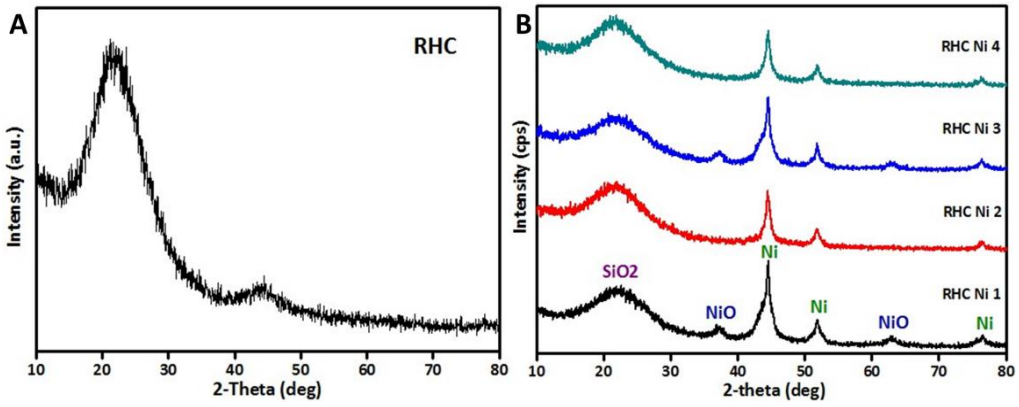

Figure 3.14 XRD curves of (A) RHC and (B) RHC Ni catalysts

Table 3.4 XRD Characteristic Peak Lists of RHC Ni Catalysts

No.	2-theta (deg)	d (ang.)	Height (cps)	FWHM (deg)	Int. I (cps deg)	Size (ang.)	Phase name
Peak list of RHC Ni 1							
1	22.37(13)	3.97(2)	149(12)	8.52(11)	1351(30)	9.93(12)	Amorphous SiO_2
2	37.21(18)	2.414(11)	30(5)	1.59(16)	54(12)	55(5)	Nickel Oxide(1,0,1), Bunsenite(1,1,1)
3	43.63(17)	2.073(8)	124(11)	2.45(10)	353(38)	36.5(15)	Nickel Oxide(0,1,2), Bunsenite(2,0,0)
4	44.43(2)	2.0373(9)	288(17)	0.46(6)	259(37)	195(24)	Nickel, syn(1,1,1)
5	51.67(3)	1.7677(9)	96(10)	1.06(4)	141(6)	87(3)	Nickel, syn(2,0,0)
6	62.76(14)	1.479(3)	36(6)	2.2(2)	159(7)	44(5)	Nickel Oxide(1,1,0), Bunsenite(2,2,0)
7	76.52(9)	1.2439(12)	38(6)	1.70(12)	92(5)	62(4)	Nickel, syn(2,2,0), Nickel Oxide(0,2,1), Bunsenite(3,1,1)
Peak list of RHC Ni 2							
1	21.44(10)	4.140(19)	191(14)	8.83(9)	1898(23)	9.56(10)	Amorphous SiO_2
2	44.45(2)	2.0366(11)	241(16)	0.75(4)	330(6)	119(6)	Nickel, syn(1,1,1)
3	51.64(2)	1.7685(7)	65(8)	0.97(6)	80(4)	95(6)	Nickel, syn(2,0,0)
4	76.23(14)	1.2480(19)	23(5)	0.84(11)	21(3)	126(16)	Nickel, syn(2,2,0)
Peak list of RHC Ni 3							
1	22.00(12)	4.04(2)	125(11)	8.11(10)	1102(18)	10.42(13)	Amorphous SiO_2
2	37.43(11)	2.401(7)	44(7)	1.43(13)	89(6)	61(5)	Bunsenite, syn(1,1,1)
3	43.46(13)	2.081(6)	109(10)	2.59(10)	346(24)	34.5(13)	Bunsenite, syn(2,0,0)
4	44.45(3)	2.0365(12)	264(16)	0.40(5)	206(22)	223(30)	Nickel, syn(1,1,1)
5	51.85(3)	1.7620(10)	103(10)	0.59(7)	121(5)	156(18)	Nickel, syn(2,0,0)
6	62.70(16)	1.481(3)	26(5)	1.72(17)	63(4)	56(6)	Bunsenite, syn(2,2,0)
7	76.27(6)	1.2474(8)	43(7)	0.79(12)	72(3)	133(21)	Nickel, syn(2,0,0), Bunsenite, syn(3,1,1)
Peak list of RHC Ni 4							
1	21.39(10)	4.150(18)	197(14)	8.62(8)	1924(22)	9.80(10)	Amorphous SiO_2
2	44.47(3)	2.0355(12)	226(15)	0.77(4)	306(6)	117(7)	Nickel, syn(1,1,1)
3	51.76(6)	1.765(2)	64(8)	1.03(6)	77(5)	90(5)	Nickel, syn(2,0,0)
4	76.43(15)	1.245(2)	25(5)	1.18(18)	40(4)	90(14)	Nickel, syn(2,2,0)

3.3.7 Catalytic performances of RHC Ni Catalysts

3.3.7.1 Effect of catalyst mass ratio

Catalysts have been placed in contact with the biomass inside the pyrolysis reactor, so the mass ratio of the catalyst and biomass has effects on the biomass devolatilization and the tar conversion efficiency. From Fig. 3.15, it can be found that the tar conversion efficiency increased with increasing the mass ratio of the RHC Ni catalysts. Obviously, the RHC Ni catalysts showed higher catalytic conversion efficiencies compared to the raw RHC because of excellent catalytic activity of nickel. In general, the tar conversion efficiency initially increased with the increase of the catalyst mass ratio; subsequently, the increasing trend became weakened. It indicated that when the mass ratio of catalyst was increased up to a constant value, it would not improve the tar conversion efficiency, possibly further influenced by other factors, e.g., the retention time, the pore structures, the char surface area and the metal chemical state. Consequently, the investigation of the catalyst mass ratio can economically optimize the reaction conditions of *in-situ* tar catalytic conversion during biomass pyrolysis. In addition, the RHC Ni catalysts combined with $NaBH_4$ modification (RHC Ni2, RHC Ni4) showed higher tar conversion efficiencies when the catalyst mass ratios were below 0.6. After that, the RHC Ni2 and RHC Ni4 can maintain the constant tar conversion efficiencies of about 93% and 91.5%, respectively, whilst the RHC Ni1 (without $NaBH_4$ modification) showed higher tar conversion efficiency up to 96.5%. It could be inferred that this result is ascribed to the following two main reasons. Firstly, the metallic nickel (Ni^0) contributed to the enhancement of the catalytic activity. As for the RHC Ni2 and RHC Ni4, the predominant chemical state of nickel is the metallic nickel (Ni^0). In addition, $NaBH_4$ hydrolysis can activate the pore formation and change the pore structure of RHC in the hot alkaline (i.e., NaOH), contributing to the increase of its specific surface areas, accordingly resulting in higher tar conversion efficiencies even at lower catalyst mass ratios.

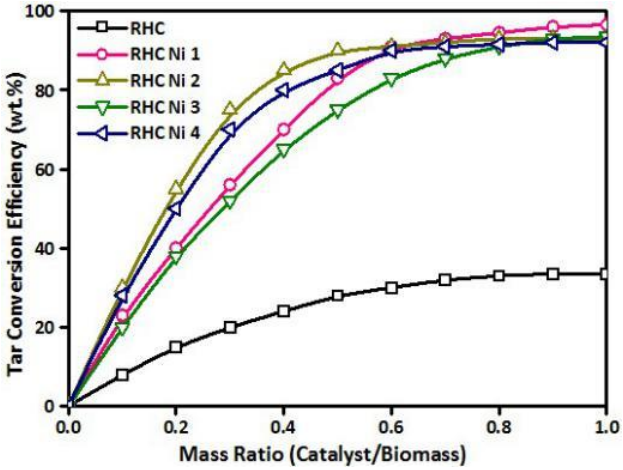

Figure 3.15 Effect of the catalyst mass ratio on in-situ tar conversion efficiency

3.3.7.2 Products from RH pyrolysis

The mass fraction of pyrolytic products (i.e., char, liquid and gas) can be estimated by the following expressions (1) and (2). Thereby, the volume fraction (*vol.%*) of the syngas yield and constituents (*H_2, CO, CO_2, CH_4, C_2H_4 and C_2H_6*) could be estimated by the expressions (3) and (4), respectively.

$$\text{Char } Yield\ (wt.\%) = \frac{Amount\ of\ solid\ residues\ (mg)}{Total\ amount\ of\ biomass\ and\ catalyst\ (mg)} \times 100\% \quad (1)$$

$$\text{Mass balance: } [\text{Char}] + [\text{Liquid}] + [\text{Gas}] = 100\% \quad (2)$$

$$\text{Gas } Yield\ (L/g) = \frac{Exit\ gas\ (L) - N_2\ \ flow\ rate\ (\text{L/min}) \times Time\ (\text{min})}{Amount\ of\ biomass\ (g)} \quad (3)$$

$$[\text{H}_2] + [CO] + [CO_2] + [CH_4] + [C_2H_4] + [C_2H_6] = 100\% \quad (4)$$

Fig. 3.16 shows the yields of products derived from RH co-pyrolysis with the RHC Ni catalysts. It can be observed that the main products derived from biomass pyrolysis at high temperatures are gases (including uncondensed tar), char and liquid, which corresponds to water and condensed tar [3-43]. In general, the mass fractions of gas, liquid and char from RH pyrolysis were about 30.3%, 37.2% and 32.5%, respectively. Obviously, mixing with the RHC or RHC Ni catalysts, the yield of product gases increased, while the liquid yield decreased (Fig. 3.16A). It is noted that the RHC Ni2 and RHC Ni4, showing the weak alkali properties due to $NaBH_4$ hydrolysis, can result in the low-yield liquid products along with higher tar conversion efficiency. Alkali catalysts have been widely used for tar

and methane reforming in the product gases via directly added into biomass by wet impregnation or dry mixing. Meanwhile, they can improve the rate of pyrolysis/gasification and tar reforming. Inherent in the ash of several biomass types are high concentrations of alkali metals. Ash is an effective catalyst for tar removal when it is blended with biomass. Alkali catalysts added to the biomass in a fluidized-bed gasifier are subject to particle agglomeration. Alkali metal catalysts are also active as secondary catalysts [3-44]. However, the alkali catalysts can react with the acidic sites resulting in poison and deactivation, whilst they enhance the ash production [3-45]. As shown in Fig. 3.16A, the yields of chars were slightly increased with the addition of RHC Ni2 and RHC Ni4.

Producer gas is the most significant product from biomass pyrolysis or gasification. The gases mass fraction and the yield increased by mixing with the RHC or RHC Ni catalysts (Fig. 3.16B). Accordingly, the increase of the syngas yield might be associated with the further devolatilization of biochar and the catalytic conversion of tar. Besides, the decrease of methane (CH_4) with the increases of CO and H_2 in syngas may be ascribed to the alkanes reforming. Biomass (i.e., RH) was initially decomposed by pyrolysis at 800 ^{o}C. Thereafter, the produced vapors including nascent tar molecules were *in-situ* cracked to the small-molecular gases by the catalytic reforming at a higher temperature. Accordingly, the RHC Ni1 showed good catalytic performances, in terms of both tar conversion efficiency and syngas upgrading.

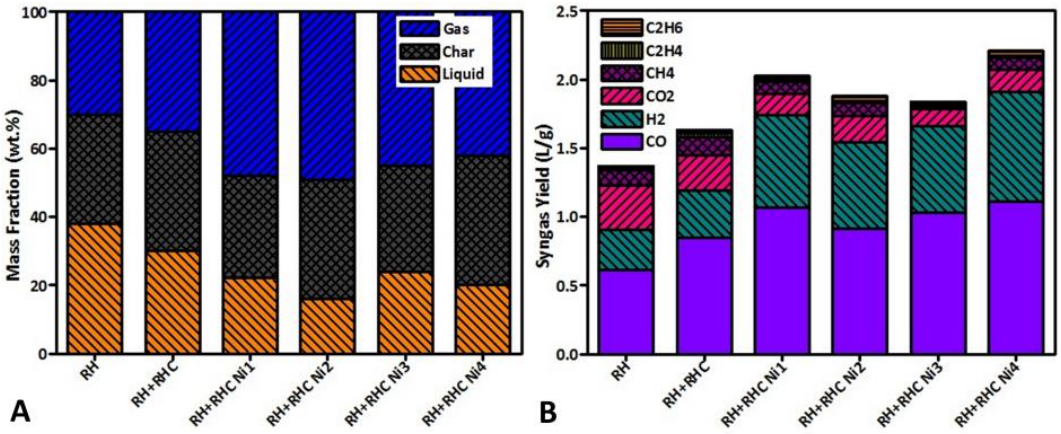

Figure 3.16 Products of RH co-pyrolysis with RHC and RHC Ni catalysts (mass ratio: 0.8)

3.3.7.3 Tar composition and evolution

Biomass tars, defined as condensable organic molecules (i.e., C_6 and greater) are pervasive in syngas derived from biomass pyrolysis or gasification, since the process is usually conducted at moderate temperatures (700-900 °C), where complete cracking of tars is hard and impossible [3-46]. Fig. 3.17 is the representative molecular species showing tars evolution in biomass catalytic pyrolysis. At lower temperatures, the primary pyrolysis products of the individual components of biomass (i.e., lignin, cellulose and hemicellulose) are formed, which have a significant amount of oxygen and have high molecular weights. As the temperature is increased, these products are cracked into the small pieces of organic compounds (e.g., benzene derivatives). These cracking reactions also result in the formation of the useful syngas components (e.g., CO and H_2). Eventually, some small hydrocarbon molecules and radicals could recombine as usual to form PAHs through the mechanisms that have been demonstrated in hydrocarbon combustion chemistry; these PAHs are prevalent in the tars that are observed during biomass pyrolysis/gasification [3-46]. Small hydrocarbon molecules and radicals might be cracked and transformed at sources into the additional syngas, restraining the formation of macromolecular organics due to polymerization.

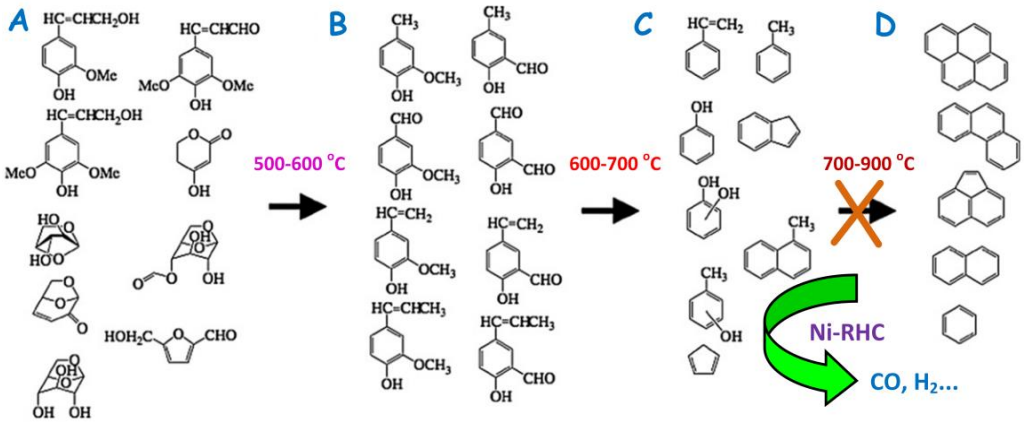

Figure 3.17 Representative molecular species showing tars evolution during catalytic pyrolysis of biomass. (A) Primary pyrolysis products are formed at low temperatures (500-600 °C); (B and C) these products can be cracked or catalytically reformed at intermediate temperatures (600-700 °C); (D) PAHs are formed at higher temperatures (700-900 °C).

GC-MS analysis has been often employed to identify the condensed tar compounds derived from biomass pyrolysis/gasification. The most important and abundant organic compounds identified are styrene, phenol and naphthalene, which were identified as the main organic components in the tar derived from pyrolysis of wood samples [3-47]. Lu et al. [3-26] also used GC-MS to analyze and found that benzene derivatives, phenol derivatives, alkanes, cycloalkanes and aromatic hydrocarbons were the main organic compounds in the bio-oils from RH pyrolysis at lower temperatures. In this research, nearly 30 peaks could be observed in the GC spectrum. Besides, MS spectra of these peaks were identified using the MS database. It can be found that the condensed tars, which were derived from the fast co-pyrolysis of RH and RHC Ni catalysts at 800 ^{o}C, existed mainly in the forms of single ring aromatic hydrocarbons (i.e., benzene, toluene) and oxygenated heterocyclic aromatic compounds (i.e., phenols), as illustrated in Fig. 3.17C, corresponding to the main identified tar compounds as shown in Table 3.5. It is noted that small amounts of other organic compounds were not shown here. The light PAHs such as two or three rings aromatic hydrocarbons (e.g., naphthalene, phenanthrene, and anthracene) can be formed during the pyrolysis of RH with RHC at 700-800 ^{o}C. However, less light PAHs in the form of two rings hydrocarbons (i.e., naphthalene, indene) were detected with the reduction of organic compound numbers in the condensed tar derived from RH co-pyrolysis with the RHC Ni catalysts. It suggested that the main compounds of biomass tar became simpler and easier to deal with when the RHC Ni catalysts were used in the gasification process. Among the condensed tar compounds, the benzene and naphthalene that can polymerize into the heavier tar molecules at high temperatures (>800 ^{o}C), were the most difficult to deal with even if the nickel catalyst was employed. Furthermore, *in-situ* catalytic conversion can significantly inhibit the polymerization of small molecular tar at sources, and reduce the follow-up macromolecular tar formation and condensation.

Table 3.5 Main Identified Organic Compounds in the Condensed Tar

RT (min)	main identified compounds	molecular formula	relative mass content (area, %)				
			RHC	RHC Ni 1	RHC Ni 2	RHC Ni 3	RHC Ni 4
3.812	Toluene	C_7H_8	5.13	2.38	-	2.60	-
4.8	Benzene	C_6H_6	8.86	3.05	2.10	5.71	2.33
6.958	Naphthalene	$C_{10}H_8$	33.85	28.50	13.64	31.02	21.16
8.05	Phenol	C_6H_6O	5.45	3.63	-	4.21	-
9.342	Indene	C_9H_8	5.93	-	-	2.82	-
9.8	Methyl-phenol	C_7H_8O	1.90	-	0.88	-	1.12
10.283	Acenaphthalene	$C_{12}H_8$	3.07	-	-	-	-
10.717	Biphenylene	$C_{12}H_8$	2.86	-	-	-	-
10.808	2-Methyl-benzofuran	C_9H_8O	1.98	-	-	-	-
11.008	2-Ethyl-phenol	$C_8H_{10}O$	6.73	15.20	17.18	11.69	13.80
13.025	4-Ethyl-2-methyl-phenol	$C_9H_{12}O$	2.50	10.60	11.88	8.87	9.52
14.833	Indenol	C_9H_8O	4.92	3.58	-	3.83	1.56
17.208	Naphthalenol	$C_{10}H_8O$	2.15	2.24	1.80	2.66	2.01
19.7	Fluoranthene	$C_{16}H_{10}$	1.64	-	-	-	-
21.267	Phenanthrene	$C_{14}H_{10}$	3.32	1.06	0.85	1.18	0.93
22.758	Anthracene	$C_{14}H_{10}$	2.77	-	-	-	-
26.65	Tetradecane	$C_{14}H_{30}$	4.80	-	-	1.52	-

Note: - not detected, RT - retention time.

3.3.8 FTIR Analysis of RHC Catalysts

Activated carbons or charcoals with highly porous textural structures, which were originated from biomass or coal, have been widely used as catalyst supports for hydrocarbons conversion and tar cracking. The reason is that their macro- and mesopores can not only greatly improve the dispersion of metal cations [3-48], but also facilitate transport of reactant molecules (e.g., toluene, 0.68 nm molecular size) into the internal surfaces of the catalyst, as illustrated in Fig. 3.18C. It has been proved that both activated carbon and activated char (e.g., RHC) have high affinity and adsorption selectivity to hydrocarbon compounds [3-48], [3-49], [3-50]. Particularly, the mesopores of activated carbon were considered to play an important role for effectively converting the heavy hydrocarbon

compounds into the light molecular fractions, and thereby inhibiting the coke formation [3-50]. Furthermore, the carbon-based catalysts with the neutral or weak base properties were found to be superior to the solid acid catalysts with respect to resistance to deactivation by deposition of coke and heavy metals [3-48], [3-50]. Fig. 3.18, A and B showed the FTIR spectra of the RH, RHC and RHC supported nickel catalysts (i.e., RHC Ni1, RHC Ni2) before and after use. The band at ~3432 cm^{-1} represents the O-H stretching vibration. The peaks at ~2925, 2879, 1428, and 1379 cm^{-1} are assigned to the $-CH_2$ groups. The band at ~1632 cm^{-1} and ~1737 cm^{-1} are assigned due to the C=C and C=O stretching, respectively [3-51], [3-52], [3-53]. The band at ~1514 cm^{-1} represents the C=C stretching vibration of lignin [3-53]. And the bands at ~1640 cm^{-1} and ~1054 cm^{-1} are assigned to the alcohol C-O and C-O-C of cellulose [3-53]. Thermal cracking can occur in the absence of oxygen, so all of these bands had different changes after pyrolysis at 800 ^{o}C (Fig. 3.18A). For instance, the peak intensity of -OH at ~3432 cm^{-1} decreased significantly, consistent with the dewatering process derived from the TG analysis. Under relative high temperatures (>500 ^{o}C), only the O-H (~3432 cm^{-1}) and aromatic C=C and C=O (~1625 cm^{-1}) can be preserved. It can be observed that the fresh RHC and RHC Ni catalysts still contained less organic functional groups, corresponding to the TG results, such as benzene derivatives (890-805, 580-420 cm^{-1} in IR spectra) (Fig. 3.18A). High-temperature biochars are carbonized more completely, containing more aromatic matter and less aliphatic matter, and show higher aromaticity and lower polarity [3-51], [3-54]. Meanwhile, at the high temperature ranges, the amorphous carbon could be turned into the turbostratic crystallites [3-53], [3-55], corresponding to a turbostratic structure of the amorphous carbon in the XRD curve. FTIR spectra also displayed the silicon-containing group vibration absorptions at ~1098, 797 and ~467 cm^{-1} that are assigned to the Si-O-Si group, which became less intense implying the formation of silicon crystal at a high temperature [3-53], [3-56]. Subsequently, the IR absorption peaks of these organic functional groups in RHC and RHC-supported catalysts were weakened or disappeared after co-pyrolysis with RH (Fig. 3.18B). Tar molecules might be initially adsorbed in the pore frameworks

of RHC, and they were released and decomposed via the further catalytic pyrolysis. Concerning the RHC Ni, a weak IR adsorption peak appearing at ~575 cm^{-1} indicated the benzene derivates, possibly ascribed to tar adsorption performance. It has been reported that the pyrolysis process can lead to the development of porous structure of the biomass and in changes in its surface chemistry [3-57]. The RH and RHC can increase the tar adsorption capacity, possessing relatively low adsorption capacity at a higher temperature exceeding 700 ^{o}C, which is explained by: (i) mass reduction of the activated carbon at the expense of SiO_2 phase; (ii) increase in the bulk density of the sample resulting in the annealing effect [3-58]. More importantly, the experimental results indicated that tars reduction was principally performed by *in-situ* catalytic conversion over the RHC and the RHC Ni catalysts, while biochar adsorption exhibited a minor effect on tar removal at high temperatures. Besides, the surface areas and pore structures of char can influence some significant parameters on catalytic reactions, such as metal catalysts distribution in RHC and residence time. As shown in Fig. 3.18D, the BET surface areas of the RHC Ni catalysts had obvious changes before and after use. Commonly, the BET surface area of catalyst might be decreased by pores blocking caused by the carbon deposition or other reasons. Due to $NaBH_4$ treatment, the fresh RHC Ni2 and RHC Ni4 catalysts showed much higher BET surface areas than other catalysts. Nevertheless, they were decreased after the first-round co-pyrolysis. In addition, the BET surface areas of the RHC, RHC Ni1 and RHC Ni3 were slightly increased after use. The further decomposition of RHC might result in the pores expansion and the structure changes of biochar. Consequently, the surface characteristics of the RHC Ni (e.g., pore structure and specific surface area) could take effects on the catalytic reactivity of tar conversion in consideration of the carbon-based catalysts, which should be studied in detail in the further work. In general, the RHC with high specific surface area is favored by metal cations and light tar adsorption efficiency at lower temperatures [3-49], [3-54], but high BET surface area of the RHC supported catalysts possessing the micro- and meso-porous structures extend the retention time of tar cracking, thereby enhancing the tar reforming activity. Furthermore, the C=C

stretch (1620-1680 cm^{-1}) appeared in the RHC and RHC Ni catalysts before and after co-pyrolysis with RH (Fig. 3.19), while minor amounts of carbonyl (C=O) groups existed in the used RHC Ni catalysts (Fig. 3.19B), indicating the efficiency of oxygen removal in the catalytic pyrolysis and the dominance of a different mechanism producing the catalytic coke. The fast heating rate enhanced the catalytic effect in pyrolysis, thus favoring catalytic coke formation. In addition, the diminished C=O reveals the carbonyl groups contained mostly in the char instead of coke [3-59].

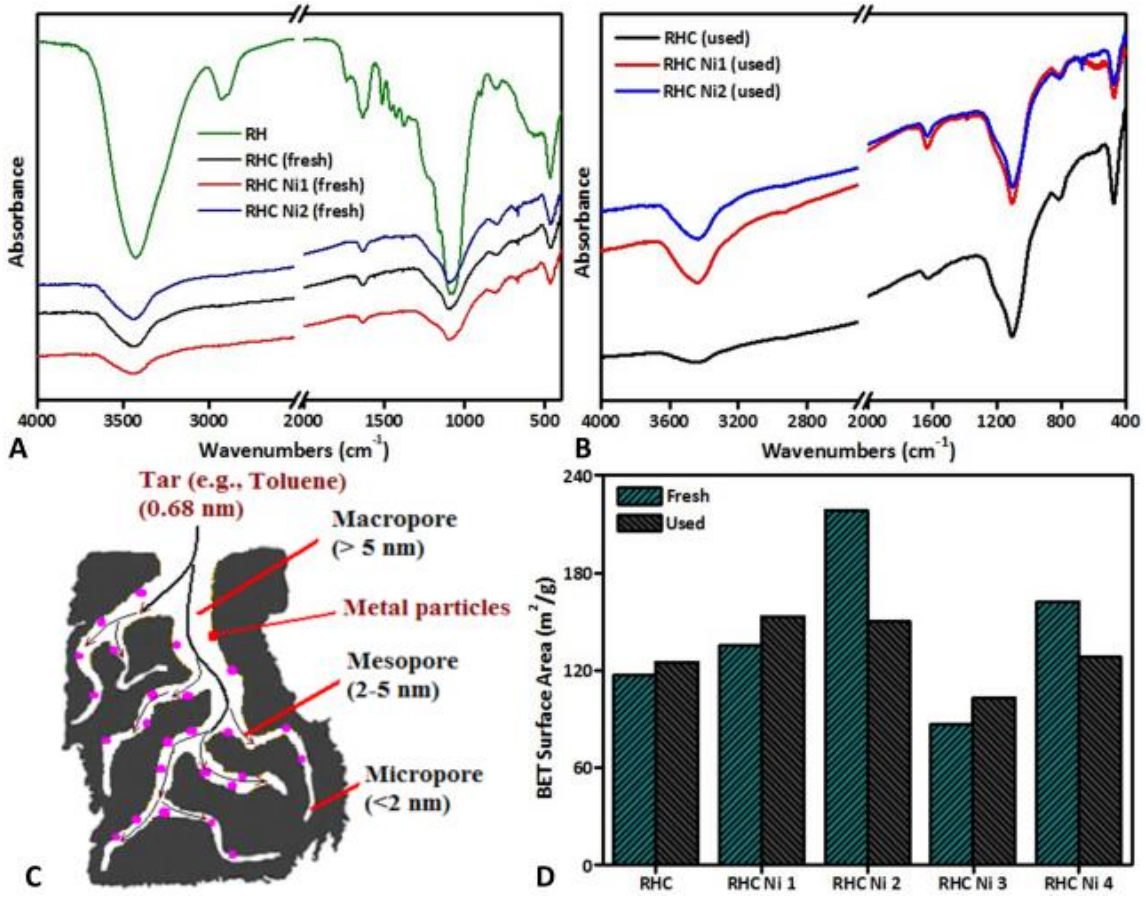

Figure 3.18 FTIR spectra of RHC and RHC Ni catalysts before (A) and after (B) co-pyrolysis with RH, (C) possible mechanism of tar conversion over activated char supported metal particles and (D) BET surface areas of the fresh and used RHC supported catalysts

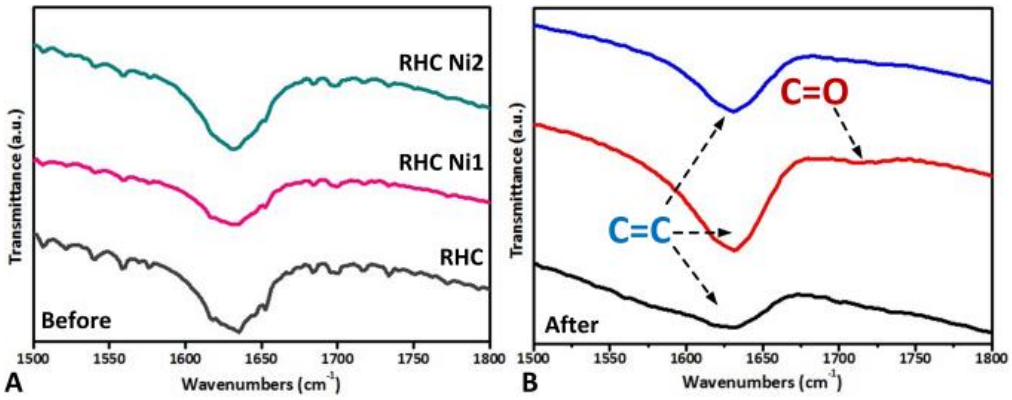

Figure 3.19 FTIR spectra of RHC and RHC Ni before (A) and after (B) co-pyrolysis with RH

3.3.9 XPS Analysis of C 1s in RHC Ni

Fig. 3.20 shows the XPS spectra of the C 1s peaks of RHC Ni before and after use at 800 ^{o}C pyrolysis temperature. In general, charging effects were corrected by adjusting the binding energy of C 1s to 284.6 eV. It can be observed that the main carbon peak at ~286 eV showed a strong decrease of intensity and shifted to the high binding energy zone, whilst the intensity of carbon loss peak increased in the used RHC Ni (Fig. 3.20A). However, it has been identified that there was no carbon energy loss peak in RHC. It is known that the "shake-up" peak of C 1s (conjugate electronic: $\pi \rightarrow \pi^{*}$) in organics is associated with the aromatics and the unsaturated structures. On one hand, co-pyrolysis of the RH and RHC Ni can produce tar compounds with these aromatic functional groups, which had an inevitable interaction with the RHC Ni catalysts (e.g., physicochemical adsorption, carbon deposition) resulting in the carbon energy loss. Meanwhile, the energy loss of carbon (C 1s) was caused by the unstable and easily electrolytic dissociated adsorbates, which was decomposed into the stable substances covered on the surface of biochar (e.g., $C_xH_y \rightarrow xC + y/2H_2$). On the other hand, the energy loss peak of C 1s might indicate that carbon atoms in RHC became more stable in the presence of Ni, and the stability of RHC Ni was enhanced by increasing the pyrolysis time. Meanwhile, the C 1s in RHC Ni exhibited a similar result that the tail between 286 and 290 eV is due to CO groups and energy loss "shake-up" features [3-60]. As shown in Fig. 3.20B, the functional

groups of organic carbon in RHC Ni existed in the main forms of C-C, C-H, and C-O with a strong decrease of intensity, while the unsaturated C=O groups were appeared after co-pyrolysis with RH (Fig. 3.20C). Besides, the amorphous carbon deposited on the surface of Ni^0 nanoparticles could be eliminated by nickel-catalyzed gasification or reforming in water vapor or CO_2, which are abundantly produced during pyrolysis. It has been reported that a carbon deposit on the surface of the Ni^0 nanoparticles during biomass pyrolysis at ~700 ^oC resulted in the formation of larger crystallites [3-16]. Furthermore, the XPS curves of the RHC supported nickel catalysts became coarse and rough after use which is ascribed to the strong interaction of carbon and other substances generating the more stable chemical bonds.

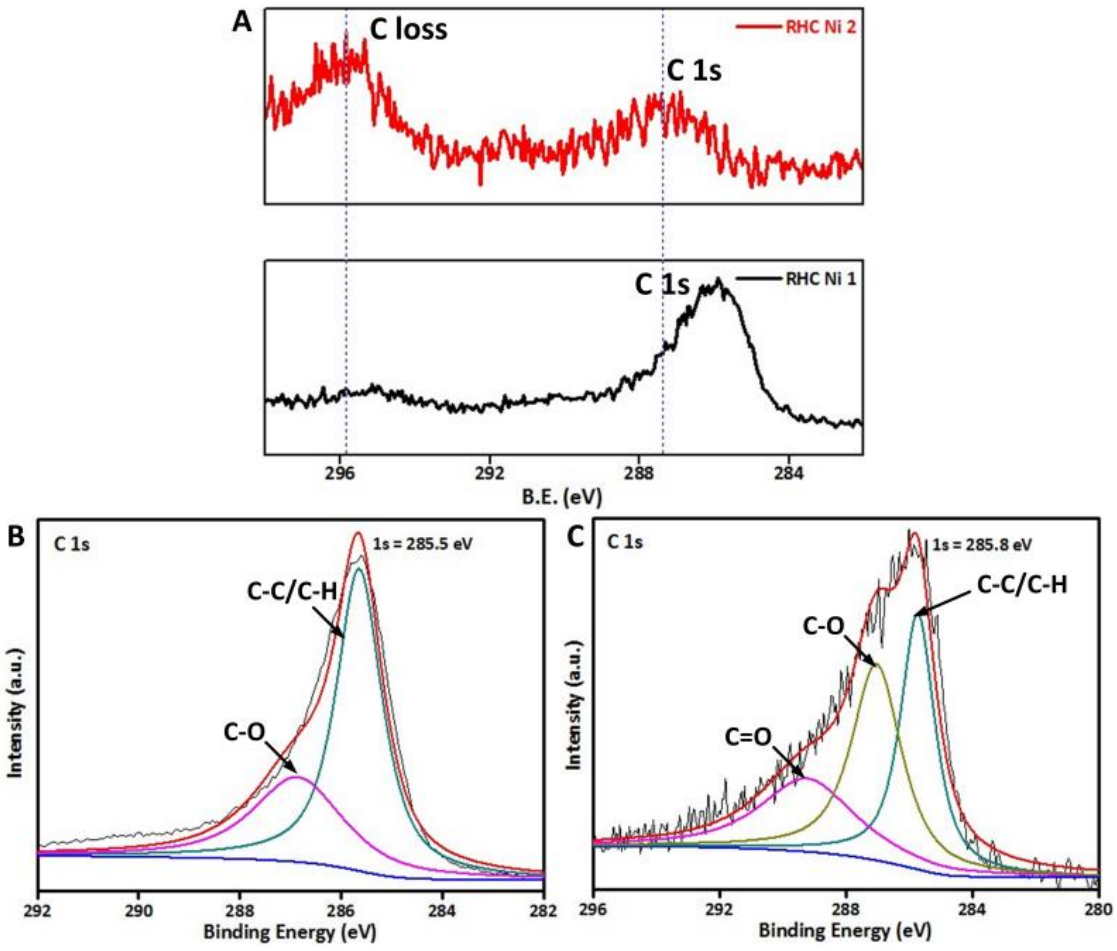

Figure 3.20 XPS spectra of the C_{1s} peaks in RHC Ni before and after use

3.4 Conclusions

An integrated concept of *in-situ* tar conversion and vapor upgrading technology has been proposed for pyrolysis of biomass, which is impregnated by nickel nitrate and treated by sodium borohydride ($NaBH_4$). Significantly, it is a potential approach for *in-situ* generation of nickel nanoparticle catalysts. The ultra-low tar yield can be obtained by RH Ni and RH Ni-B pyrolysis, especially in terms of high removal efficiencies of 96.9% and 98.6%, respectively, compared to the raw RH pyrolysis. On one hand, the removed tar was converted into the extra gases by the thermochemical reactions (i.e., cracking, reforming) with Ni catalysis effect; on the other hand, the Ni catalyst could enhance the pyrolysis efficiency and restrain at source the formation of condensable tar due to polymerization. In addition, the condensed tar existed mainly in the forms of mononuclear and oxygenated aromatic compounds. The condensable tar could be catalytically transformed into the non-condensable tar or small molecule gases. In this study, the metallic nickel species coexisted with some nickel oxides caused by the partial reduction by the carbon atoms or reducing gas (e.g., H_2, CO). The generated polymolecularity Ni^0 might be caused by the disproportionated reaction and strong reducibility of $NaBH_4$. Compared to the conventional catalysts preparation methods through the hydrogenation reduction at the severe conditions (e.g., high temperature and pressure), this approach is much convenient and energy-saving. The condensable tar derived from RH pyrolysis could be significantly removed up to 96.5% and 92.6%, by co-pyrolysis with the RHC Ni and RHC Ni-B, respectively. Herein, a novel concept (as illustrated in Fig. 3.21) can be proposed that tar-free syngas and char supported catalysts are produced by metal wastewater recycle integrated with biomass catalytic pyrolysis.

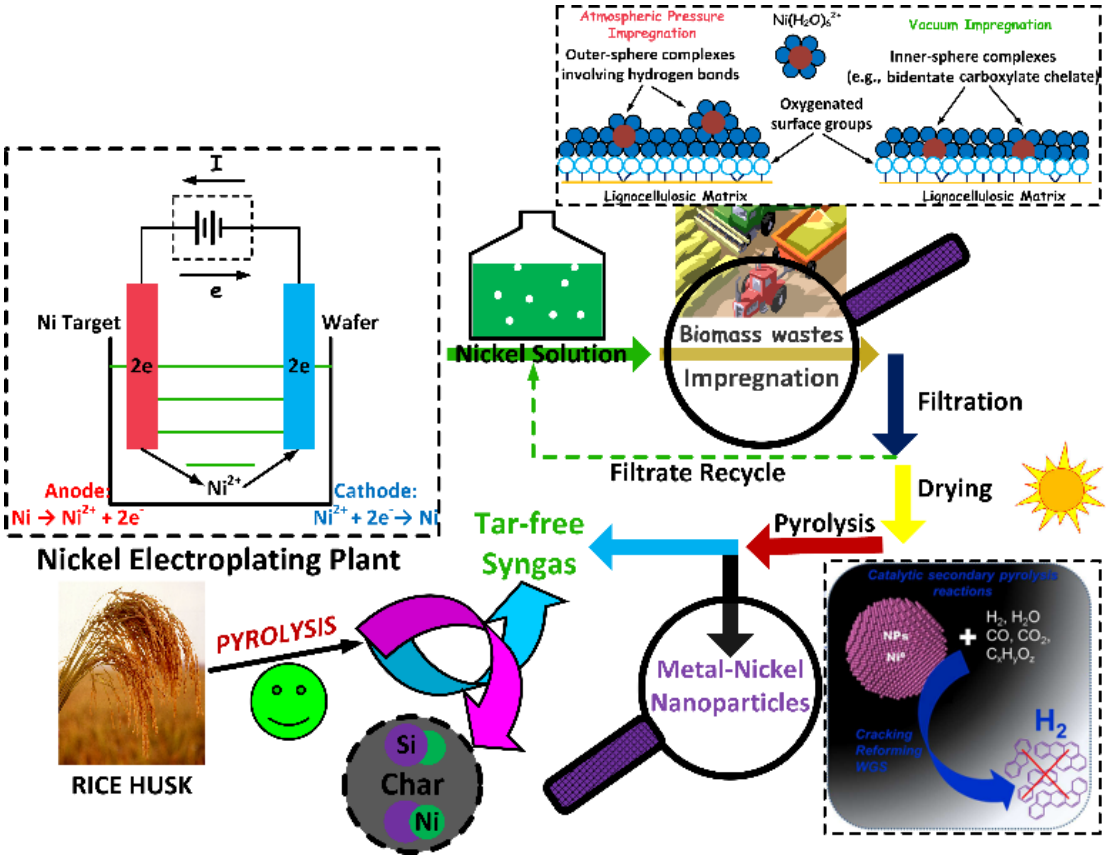

Figure 3.21 Integrated concept of wastewater recycling containing heavy metal with biomass waste catalytic pyrolysis

The synthesized RHC Ni catalysts exhibited high catalytic performances on *in-situ* tar conversion and vapor upgrading via co-pyrolysis with biomass, especially in terms of the tar conversion efficiency up to 96.5% by RHC Ni1. Meanwhile, the yield of gas increased along with syngas upgrading, which is associated with further devolatilization of biochar and biomass tar catalytic conversion. Only small amounts of PAHs in the form of two-ring hydrocarbons (i.e., naphthalene) existed in the condensed tar derived from RH co-pyrolysis with the RHC Ni catalysts. It proved that the main compounds of tar became easier to deal with when the RHC Ni catalysts were used in the gasification process. Thus, *in-situ* catalytic conversion can significantly inhibit the small-molecular tars polymerization and eliminate the macromolecular tar formation. In addition, it has been proved that RHC with high specific surface area can be favored by metal cations and light tar adsorption at lower temperatures,

but high specific surface areas of the RHC Ni catalysts with micro- and meso-porous structures can extend the residence time of tar cracking, thereby enhancing tar reforming activity. Nevertheless, the surface characteristics of the RHC Ni (e.g., pore structure and surface area) have influences on the catalytic reactivity of tar conversion in consideration of the carbon-based catalysts, which should be studied in detail. It is expected that more metallic nickel nanoparticles can be formed, if the time of carbothermal reduction is prolonged. Moreover, the RHC Ni has a potential to be used for *ex-situ* reforming of tar derived from biomass gasification.

References

[3-1] Z. Schnepp, Biopolymers as a flexible resource for nanochemistry. *Angewandte Chemie International Edition* 2013, 52, 1096-1108.

[3-2] W.J. Liu, H. Jiang, K. Tian, Y.W. Ding, H.Q. Yu, Mesoporous carbon stabilized MgO nanoparticles synthesized by pyrolysis of $MgCl_2$ preloaded waste biomass for highly efficient CO_2 capture. *Environmental Science & Technology* 2013, 47, 9397-9403.

[3-3] W.J. Liu, K. Tian, H. Jiang, H.Q. Yu, Harvest of Cu NPs anchored magnetic carbon materials from Fe/Cu preloaded biomass: Pyrolysis, characterization, and catalytic activity on aqueous reduction of 4-nitrophenol. *Green Chemistry* 2014, 16, 4198-4205.

[3-4] W.J. Liu, K. Tian, Y.R. He, H. Jiang, H.Q. Yu, High-yield harvest of nanofibers/mesoporous carbon composite by pyrolysis of waste biomass and its application for high durability electrochemical energy storage. *Environmental Science & Technology* 2014, 48(23), 13951-13959.

[3-5] W.P. Pan, G.N. Richards, Influence of metal ions on volatile products of pyrolysis of wood. *Journal of Analytical and Applied Pyrolysis* 1989, 16, 117-126.

[3-6] D.J. Nowakowski, J.M. Jones, Uncatalysed and potassium-catalysed pyrolysis of the cell-wall constituents of biomass and their model compounds. *Journal of Analytical and Applied Pyrolysis* 2008, 83, 12-25.

[3-7] J.G. Lee, E-J. Shin, R.A. Pavelka, M.S. Kirchner, D. Dounas-Frazer, B.D. McCloskey, et al. Effect of metal doping on the initial pyrolysis chemistry of cellulose chars. *Energy Fuel* 2008, 22, 2816-2825.

[3-8] A. Khelfa, G. Finqueneisel, M. Auber, J.V. Weber, Influence of some minerals on the cellulose thermal degradation mechanisms. *Journal of Thermal Analysis and Calorimetry* 2008, 92, 795-799.

[3-9] C. Couhert, J-M. Commandre, S. Salvador, Is it possible to predict gas yields of any biomass after rapid pyrolysis at high temperature from its composition in cellulose, hemicellulose and lignin? *Fuel* 2009, 88, 408-417.

[3-10] P.R. Patwardhan, J.A. Satrio, R.C. Brown, B.H. Shanks, Influence of inorganic salts on the primary pyrolysis products of cellulose. *Bioresource Technology* 2010, 101, 4646-4655.

[3-11] C.A. Zaror, I.S. Hutchings, D.L. Pyle, H.N. Stiles, R. Kandiyoti, Secondary char formation in the catalytic pyrolysis of biomass. *Fuel* 1985, 64, 990-994.

[3-12] A. Demirbas, Combustion characteristics of different biomass fuels. *Progress in Energy and Combustion Science* 2004, 30, 219-230.

[3-13] G. Dobele, G. Rossinskaja, T. Dizhbite, G. Telysheva, D. Meier, O. Faix, Application of catalysts for obtaining 1,6-anhydrosaccharides from cellulose and wood by fast pyrolysis. *Journal of Analytical and Applied Pyrolysis* 2005, 74, 401-405.

[3-14] K. Suzuki, T. Suzuki, Y. Takahashi, M. Okimoto, T. Yamada, N. Okazaki, et al. Nickel-catalyzed carbonization of wood for coproduction of functional carbon and fluid fuels II: improved fuel quality of oil fraction and increased heating value of gas fraction. *Journal of Wood Science* 2009, 55, 60-68.

[3-15] C.D. Blasi, C. Branca, A. Galgano, Products and global weight loss rates of wood decomposition catalyzed by zinc chloride. *Energy Fuel* 2007, 22, 663-670.

[3-16] Y. Richardson, J. Motuzas, A. Julbe, G. Volle, J. Blin, Catalytic investigation of in situ generated Ni metal nanoparticles for tar conversion during biomass pyrolysis. *Journal of Physical Chemistry C* 2013, 117, 23812-23831.

[3-17] J. Ni, L. Chen, J. Lin, S. Kawi, Carbon deposition on borated alumina supported nano-sized Ni catalysts for dry reforming of CH_4. *Nano Energy* 2012, 1, 674-686.

[3-18] J.C.S. Wu, H.C. Chou, Bimetallic Rh-Ni/BN catalyst for methane reforming with CO_2. *Chemical Engineering Journal* 2009, 148, 539-545.

[3-19] W. Wang, J.C. Martin, N. Zhang, C. Ma, A. Han, L. Sun, Harvesting silica nanoparticles from rice husks. *Journal of Nanoparticle Research* 2011, 13, 6981-6990.

[3-20] H. Yang, R. Yan, H. Chen, D.H. Lee, C. Zheng, Characteristics of hemicellulose, cellulose and lignin pyrolysis. *Fuel* 2007, 86, 1781-1788.

[3-21] A. Meng, H. Zhou, L. Qin, Y. Zhang, Q. Li, Quantitative and kinetic TG-FTIR investigation on three kinds of biomass pyrolysis. *Journal of Analytical and Applied Pyrolysis* 2013, 104, 28-37.

[3-22] Y. Shen, T. Sun, J. Jia, Novel desulfurization method of sodium borohydride reduction for coal water slurry. *Energy Fuels* 2011, 25, 2963-2967.

[3-23] G. Garbarino, E. Finocchio, A. Lagazzo, I. Valsamakis, P. Riani, V.S. Escribano, G. Busca, Steam reforming of ethanol-phenol mixture on Ni/Al_2O_3: effect of magnesium and boron on catalytic activity in the presence and absence of sulfur. *Applied Catalysis B: Environmental* 2014, 147, 813-826.

[3-24] M. Liu, H. Wang, J. Han, Y. Niu, Enhanced hydrogenolysis conversion of cellulose to C2-C3 polyols via alkaline pretreatment. *Carbohydrate Polymers* 2012, 89, 607-612.

[3-25] Y. Copur, A. Tozluoglu, O. Ozyurek, Sodium borohydride ($NaBH_4$) pretreatment for efficient enzymatic saccharification of wheat straw. *Bioresource Technology* 2012, 107, 258-266.

[3-26] R. Lu, G.P. Sheng, Y.Y. Hu, P. Zheng, H. Jiang, Y. Tang, H.Q. Yu, Fractional characterization of a bio-oil derived from rice husk. *Biomass Bioenergy* 2011, 671-678.

[3-27] R.M. Baldwin, K.A. Magrini-Bair, M.R. Nimlos, P. Pepiot, B.S. Donohoe, J.E. Hensley, S.D. Philips, Current research on thermochemical conversion of biomass at the National Renewable Energy Laboratory. *Applied Catalysis, B: Environmental* 2012, 115-116, 320-329.

[3-28] A. Paethanom, S. Nakahara, M. Kobayashi, P. Prawisudha, K. Yoshikawa, Performance of tar removal by absorption and adsorption for biomass gasification. *Fuel Processing Technology* 2012, 104, 144-154.

[3-29] N. Liu, K. Huo, M.T. McDowell, J. Zhao, Y. Cui, Rice husks as a sustainable source of nanostructured silicon for high performance Li-ion battery anodes. *Scientific Report* 2013, 3, 1919.

[3-30] D.S. Jung, M.H. Ryou, Y.J. Sung, S.B. Park, J.W. Choi, Recycling rice husks for high-capacity lithium battery anode. *Proc. Natl. Acad. Sci. U.S.A.* 2013, 110, 12229-12234.

[3-31] Y. Richardson, J. Blin, G. Volle, J. Motuzas, A. Julbe, In situ generation of Ni metal nanoparticles as catalyst for H_2-rich syngas production from biomass gasification. *Applied Catalysis, A: General* 2010, 382, 220-230.

[3-32] W. Torres, S.S. Pansare, J.G. Goodwin, Hot gas removal of tars, ammonia, and hydrogen sulfide from biomass gasification gas. *Catalysis Reviews: Science and Engineering* 2007, 49, 407-456.

[3-33] N. Yuzer, Z. Cinar, F. Akoz, H. Biricik, Y.Y. Gurkan, N. Kabay, A.B. Kizilkanat, Influence of raw rice husk addition on structure and properties of concrete. *Construction and Building Materials* 2013,

44, 54-62.

[3-34] N.B. Klinghoffer, M. J. Castaldi and A. Nzihou, Catalyst properties and catalytic performance of char from biomass gasification. *Industrial & Engineering Chemistry Research* 2012, 51, 13113-13122.

[3-35] S.J. Gregg, K.S.W. Sing, *Adsorption, Surface Area and Porosity*, Second ed., Academic Press, London, 1982.

[3-36] L. Lin, S.R. Zhai, Z.Y. Xiao, Y. Song, Q.D. An, X.W. Song, Dye adsorption of mesoporous activated carbons produced from NaOH-pretreated rice husks. *Bioresource Technology* 2013, *136*, 437-443.

[3-37] Y. Chen, Y. Zhu, Z. Wang, Y. Li, L. Ding, X. Gao, Y. Ma, Y. Guo, Application studies of activated carbon derived from rice husks produced by chemical-thermal process - A review. *Advanced Colloid and Interface Science* 2011, *163*, 39-52.

[3-38] Q. Yan, C. Wan, J. Liu, J. Gao, F. Yu, J. Zhang, Z. Cai, Iron nanoparticles in situ encapsulated in biochar-based carbon as an effective catalyst for the conversion of biomass-derived syngas to liquid hydrocarbons. *Green Chemistry* 2013, *15*, 1631-1640.

[3-39] T.H. Liou, Development of mesoporous structure and high adsorption capacity of biomass-based activated carbon by phosphoric acid and zinc chloride activation. *Chemical Engineering Journal* 2010, *158*, 129.

[3-40] X. Song, Y. Zhang, C. Chang, Novel method for preparing activated carbons with high specific surface area from rice husk. *Industrial & Engineering Chemistry Research* 2012, *51*, 15075-15081.

[3-41] Y. Shen, P. Zhao, Q. Shao, D. Ma, F. Takahashi, K. Yoshikawa, In-situ catalytic conversion of tar using rice husk char-supported nickel-iron catalysts for biomass pyrolysis/gasification. *Applied Catalysis, B: Environmental* 2014, *152-153*, 140-151.

[3-42] S. Cheah, K.R. Gaston, Y.O. Parent, M.W. Jarvis, T.B. Vinzant, K.M. Smith, et al. Nickel cerium olivine catalyst for catalytic gasification of biomass. *Applied Catalysis, B: Environmental* 2013, *134-135*, 34-45.

[3-43] F.X. Collard, J. Blin, A. Bensakhria, J. Valette, Influence of Impregnated Metal on the Pyrolysis Conversion of Biomass Constitutes. *Journal of Analytical and Applied Pyrolysis* 2012, *95*, 213-226.

[3-44] D. Sutton, B. Kelleher, J.R.H. Ross, Review of literature on catalysts for biomass gasification. *Fuel Processing Technology* 2001, *73*, 155-173.

[3-45] Z. Abu El-Rub, E.A. Bramer, G. Brem, Review of catalysts for tar elimination in biomass gasification process. *Industrial & Engineering Chemistry Research* 2004, *43*, 6911-6919.

[3-46] R.M. Baldwin, K.A. Magrini-Bair, M.R. Nimlos, P. Pepiot, B.S. Donohoe, J.E. Hensley, S.D. Phillips, Current research on thermochemical conversion of biomass at the National Renewable Energy Laboratory. *Applied Catalysis, B: Environmental* 2012, *115-116*, 320-329.

[3-47] C. Wu, L. Wang, P.Y. Williams, J. Shi, J. Huang, Hydrogen production from biomass gasification with Ni/MCM-41 catalysts: Influence of Ni content. *Applied Catalysis, B: Environmental* 2011, *108*, 6-13.

[3-48] C. Xu, J. Donald, E. Byambajav, Y. Ohtsuka, Recent advances in catalysts for hot-gas removal of tar and NH_3 from biomass gasification. *Fuel* 2010, *89*, 1784-1795.

[3-49] A. Paethanom, S. Nakahara, M. Kobayashi, P. Prawisudha, K. Yoshikawa, Performance of tar removal by absorption and adsorption for biomass gasification. *Fuel Processing Technology* 2012, *104*, 144-154.

[3-50] C. Xu, S. Hamilton, M. Ghosh, Hydro-conversion of Athabasca vacuum tower bottoms in supercritical toluene with highly porous biomass-derived activated carbon and metal-carbon composite. *Fuel* 2009, *88*, 2097-2105.

[3-51] B. Chen, D. Zhou, L. Zhu, Transitional adsorption and partition of nonpolar and polar aromatic contaminants by biochars of pine needles with different pyrolytic temperatures. *Environmental Science & Technology* 2008, *42*, 5137-5143.

[3-52] Z. Chen, B. Chen, C.T. Chiou, Fast and slow rates of naphthalene sorption to biochars produced at different temperatures. *Environmental Science & Technology* 2012, *38*, 4649-4655.

[3-53] X. Xiao, B. Chen, L. Zhu, Transformation, morphology and dissolution of silicon and carbon in rice straw-derived biochars under different pyrolytic temperatures. *Environmental Science & Technology* 2014, *68*, 3411-3419.

[3-54] Z. Chen, B. Chen, D. Zhou, W. Chen, Bisolute sorption and thermodynamic behavior of organic pollutants to biomass-derived biochars at two pyrolytic temperatures. *Environmental Science & Technology* 2012, *46*, 12476-12483.

[3-55] M. Keiluweit, P.S. Nico, M.G. Johnson, M. Kleber, Dynamic molecular structure of plant biomass-derived black carbon (biochar). *Environmental Science & Technology* 2010, *44*, 1247-1253.

[3-56] L. Qian, B. Chen, Dual role of biochars as adsorbents for aluminum: the effects of oxygen-containing organic components and the scattering of silicate particles. *Environmental Science & Technology* 2013, *47*, 8759-8768.

[3-57] I. Uzunov, S. Uzunova, D. Angelova, A. Gigova, Effect of the pyrolysis process on the oil sorption capacity of rice husk. *Journal of Analytical and Applied Pyrolysis* 2012, *98*, 166-176.

[3-58] D. Angelova, I. Uzunov, S. Uzunova, A. Gigova, L. Minchev, Kinetics of oil and oil products adsorption by carbonized rice husks. *Chemical Engineering Journal* 2011, *172*, 306-311.

[3-59] S. Du, J.A. Valla, G.M. Bollas, Characteristics and origin of char and coke from fast and slow, catalytic and thermal pyrolysis of biomass and relevant model compounds. *Green Chemistry* 2013, *15*, 3214-3229.

[3-60] Y. Zhu, S. Murali, M.D. Stoller, K.J. Ganesh, W. Cai, P.J. Ferreira, et al. Carbon-based supercapacitors produced by activation of graphene. *Science* 2011, *332*, 1537-1541.

Chapter 4

Ex Situ Catalytic Reforming of Tar and Syngas over the Metallic Nickel Nanoparticles Embedded in the Carbon Matrix of Rice Husk Char for Biomass Gasification

4.1 Introduction

Pyrolysis-reforming has been proved to be effective for thermochemical conversion of biomass to improve the gas yield, reduce tar contents, and enhance conversion rates [4-1], [4-2], [4-3], [4-4], [4-5]. In the two stage process, biomass can be decomposed in the first stage, and then the derived vapors and tar are reformed in the second stage at higher temperatures (T ≥800 °C) (as illustrated in Fig.4-1). The addition of different catalysts with/without steam in the second stage has shown a positive effect on tar reduction and syngas reformation as well. In the previous work, it has been proved that rice husk char (RHC) supported nickel catalysts shows good catalytic performances on *in-situ* conversion of tar for biomass gasification [4-6], [4-7]. Catalysts placed in contact with the feedstock inside of the pyrolysis reactor (namely *in situ*) can improve the conversion of biomass, and adjust the distribution of volatilized products [4-8], [4-9], [4-10]. Meanwhile, it can inhibit the nascent tars polymerization, thereby reducing the macromolecular tar formation. However, the nickel nanoparticles embedded in the carbon matrix of RHC will be unfeasible to be frequently recycled from the solid residues. Likewise, catalysts can also be employed in the downstream of the primary reactor (*ex situ*) for tar conversion and vapors upgrading [4-11], [4-12]. Liu et al. [4-13] studied the intrinsic fundamentals of catalytic tar removal over *in situ* and *ex situ* coal chars in a

two-stage gasification of coal. It has been demonstrated that the *in-situ* char had better structural properties than the *ex-situ* char for tar cracking. Subsequently, Dabai et al. [4-14] also investigated the effect of reaction conditions on tar formation and destruction in a fixed-bed downdraft gasifier. The presence of char in the second stage decreased the tar yield to 0.2%. Among these researches, tar reforming was usually performed in the second stage at high temperatures above 1000 ^{o}C, so the coke deposited on the surface of the char results in the decrease of the specific surface area [4-13], [4-14], [4-15]. The key factor in gasification of biomass is the temperature. The temperature range of 800-900 ^{o}C is identified as the most common one in biomass gasification, considering the balance of the benefits and the drawbacks associated with the thermal level [4-16]. As a biomass waste, rice husk gasification can be conducted at a relative lower temperature range of 750-850 ^{o}C compared to the other solid fuels (e.g., wood, coal) [4-16]. Although *in situ* conversion shows some advantages such as tar reduction at sources. Moreover, if the rice husk ash supported catalysts are used as bed materials, it can enhance the feasibility to be used in the commercial plants. However, the ex situ catalytic conversion is much feasible to be used, because the catalysts can be much easily renewed and regenerated. In addition, the syngas could be upgraded in the reformer. The catalytic performances including reaction activity, cycle tests and deactivation of the RHC Ni catalysts could be preliminary studied for *ex situ* catalytic conversion of tar derived from biomass gasification.

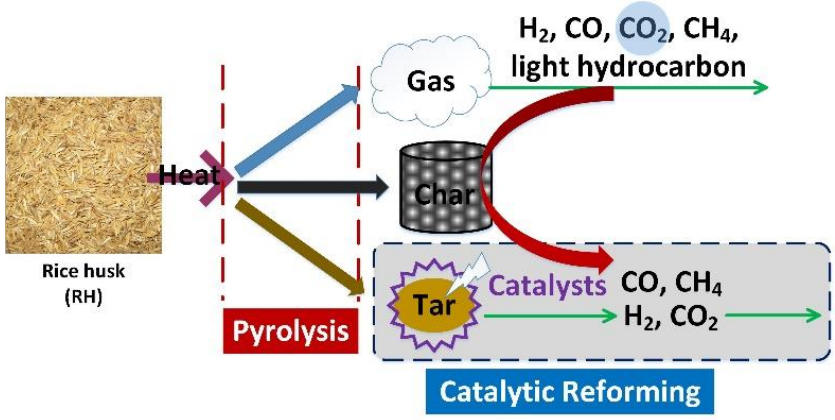

Figure 4-1 Pyrolysis-catalytic reforming of biomass for tar-free syngas production

4.2 Experimental

4.2.1 Biomass and Char Characterization

The properties of rice husk and rice hush char were shown in Table 2.1.

4.2.2 Catalysts Preparation

It has become an emerging area of using natural biopolymers as the templates to construct novel hierarchical inorganic materials because of their unique and complex microstructures [4-17]. Compared to the artificial templates, biomaterials as the natural biotemplates have the features of hierarchical, abundant, complex, renewable, and environmentally benignity [4-18]. Additionally, RH with a highly anisotropic cellular structure can be used as a natural biotemplate to generate the pyrolyzed char with micro-, meso-, and macro-porous. Herein, the metallic nickel nanoparticles can be generated in the carbon matrix of RHC by a one-step carbothermal pyrolysis (Fig. 4.2). Initially, biomass feedstock of RH (20g) was added into the Ni^{2+} solution (0.1 mol/L) using $Ni(NO_3)_2{\cdot}6H_2O$ as a nickel precursor under the atmospheric pressure and dried in an oven at 105 °C. Consideration of the economic efficiency, the nickel electroplating wastewater can be applied. Subsequently, the dry-based RH Ni was rapidly pyrolyzed at ~750 °C in an inert gas (e.g., N_2) for 10 min. After that, the RHC Ni (~10 wt.% Ni/RHC) was obtained by collecting the solid residues. The prepared RHC Ni was dry-stored for further use. It has been reported that high temperature can induce fast adsorption and high adsorption capacity at equilibrium [4-19]. In usual, the nickel ions (Ni^{2+}) adsorption on the RH or RHC is an endothermic process with a very low adsorption heat. Moreover, this adsorption process is primarily controlled by physical adsorption [4-19] and other adsorption mechanisms, e.g., ion exchange (R1) [4-20]. In summary, nickel cation in the bulk liquid should undergo three steps before it is adsorbed onto the active site of the pore surface of RHC: mass transfer of nickel cations from bulk liquid to the external surface of RHC, diffusion of the cations from external surface to the

interior of RHC through the pore and adsorption of nickel cations onto the pores surface [4-19]. The above method could promote the formation of the dispersed SiO_2 microspheres inside of RH or RHC. Moreover, the remaining residue mainly composed of holocellulose was easily transformed to chars under the relative low temperatures without the protection of silica coating on the organic matters. Ultimately, the activated carbons with easy-to-diffuse mesopores could be achieved [4-21]. The char adsorption capacity of metal cations depends on the preparation methods (e.g., atmospheric pressure, vacuum), the char surface characteristics (e.g., surface area, pore size), the impregnation temperature, the metal ion type, etc. It should be noted that most of nickel species were assumed to be totally transferred to the solid phase (char) during pyrolysis [4-22].

$Ni^{2+} + 2(\text{-SiOH}) \leftrightarrow Ni(\text{-SiO})_2 + 2H^+$	(R1)
$5Ni(NO_3)_2 + 24H_2O \rightarrow Ni^{2+} + 4[Ni(H_2O)_6]^{2+} + 10NO_3^-$	(R2)
$[Ni(H_2O)_6]^{2+} \rightarrow Ni(OH)_2 + 2H_3O^+ + 2H_2O$	(R3)
$Ni(OH)_2 \rightarrow NiO + H_2O$	(R4)

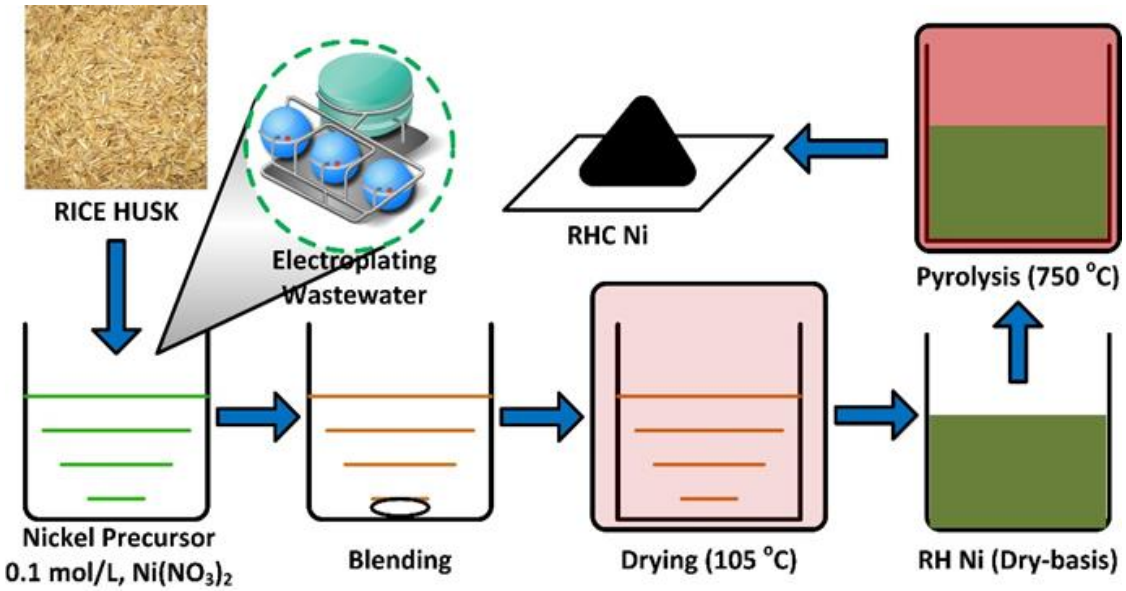

Figure 4.2 Schematic diagram of RHC Ni preparation

4.2.3 Biomass Pyrolysis and Tar Reforming System

The experimental setup is shown in Fig. 4.3, which is illustrated in the section 2.2.3. At first, RH feedstock was prepared by crushing and sieving with the particle size below 5.0 mm. Before adding the catalysts and biomass feedstock, the inert carrier gas (i.e., N_2) with a flow rate of ~1.0 L/min was continuously injected into the reactor to clear away the residual gases in the entire system. The pyrolyzer was heated up to 750 °C, whilst the temperature of the reformer was controlled in the range of 500-800 °C. The fresh RHC Ni catalyst was initially put in the reformer. After that, RH (20 g) could be fed into the pyrolyzer, and the volatile matters were released in the form of vapors, including the nascent tars. Biomass tar could be cracked and reformed into the small molecular gases over the RHC Ni by the thermochemical reactions. The tar was collected by cold isopropanol in the gas cleaning unit.

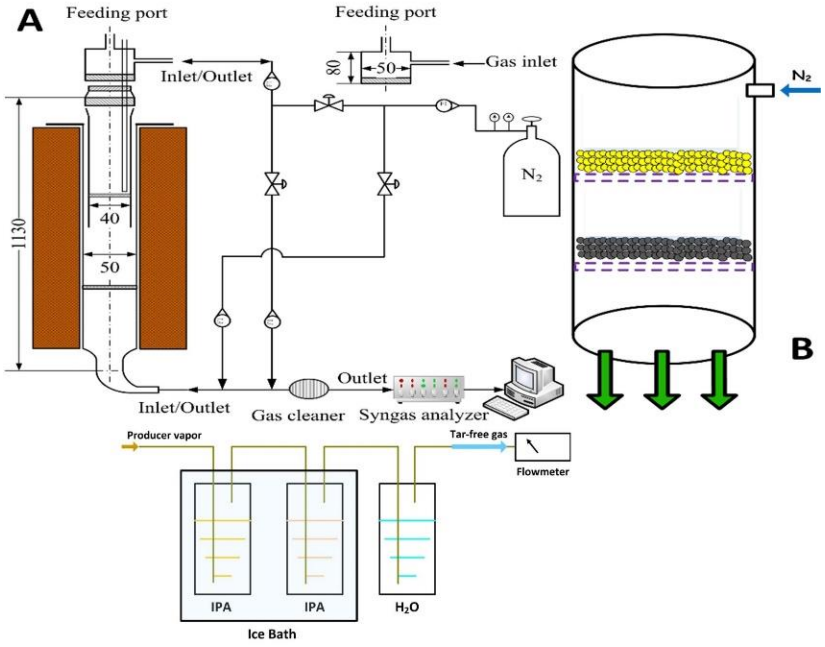

Figure 4.3 Schematic diagrams of experimental setup (A) and scheme (B) for biomass gasification

4.2.4 Sampling and Analysis

The sampling and analytical methods were performed according to the section 2.2.4. The fresh and used RHC Ni catalysts were characterized by the TG/DTG analysis, the X-ray diffraction analysis (*XRD*,

Rigaku, XRD-DSC II, Japan), the scanning electron microscopy (*SEM, JSM-6610, JEOL/EO, Japan*), and the transmission electron microscopy-energy dispersive spectroscopy (*TEM-EDS, JEM-2010F, JEOL, Japan*), respectively.

4.2.5 CO_2 Gasification of RHC and RHC Ni

The overall *in situ* catalytic gasification of carbon materials could be shown in Fig. 4.4, showing a simplified view of a cut of a porous grain with metal nanoparticles, which may start moving under the reaction conditions [4-23]. RHC Ni is a nickel-carbon composite consisting of Ni^0 nanoparticles highly dispersed in an amorphous carbon matrix. Char gasification reactions with CO_2 or H_2O are actually known to be highly endothermic and to occur at temperatures higher than 800 ^oC [4-24]. Thereby, char gasification is one of the most energy consuming step in the overall gasification process. It has been reported that the presence of alkali and transition metals can enhance the CO_2 gasification reactivity of biomass char [4-25]. The presence of nickel inside the char matrix might enhance the reactivity of CO_2 char gasification as well.

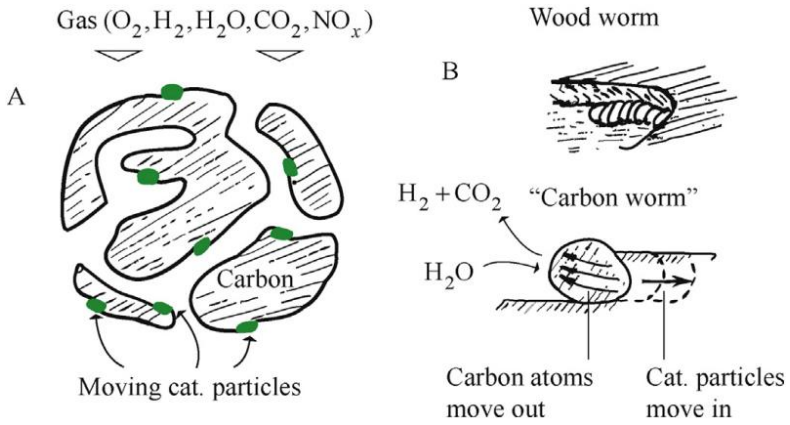

Figure 4.4 Catalytic carbon *in situ* gasification (A) Porous carbon cut showing catalyst nanoparticles (moving under reaction conditions); (B) Analogy with a woodworm and detail of a single "carbonworm" particle. It shows the diffusion of carbon atoms through the particle in one direction and the particle itself moving in the opposite direction and keeping tight contact with carbon (into a step, corresponding to a crystallographic a direction). [4-23]

CO_2 gasification experiments were carried out under the isothermal conditions in a TG analyzer and a packed bed reactor, respectively. In each TG experiment, char powder (~10 mg) was loaded in Al_2O_3 pan and heated (20 ^oC/min) in the N_2 atmosphere (150 ml/min) to the pre-set gasification temperature. In order to ensure that the mass loss of RHC in the isothermal CO_2 gasification process was only attributed to the char-gas reaction, the sample was kept at the gasification temperature under N_2 for 10 min. Subsequently, N_2 was switched to CO_2 (150 ml/min) to initiate the isothermal gasification. Furthermore, the mass loss of char sample was recorded continuously as a function of the gasification time. The carbon conversion (X_{TGA}) is calculated by the following equation [4-26], [4-27].

$$X_{TGA} = \frac{m_o - m_t}{m_o - m_c - m_{ash}} \times 100\%$$

Where m_0 represents the initial mass of the char at the onset gasification, m_t is the instantaneous mass of the char at time t, m_c is the mass of catalyst, and m_{ash} is the mass of ash after completion of gasification.

Based on the optimal conditions in TGA, the lab-scale CO_2 gasification of RHC Ni is conducted in a packed bed reactor as shown in Fig. 4.5, which is mainly composed of the gasifier and the gas analyzer. The char sample was heated up to the desired temperature under the N_2 condition (200 ml/min), then the gas was changed into CO_2 (200 ml/min) to perform the char gasification reaction under the isothermal condition. The carbon conversion (X_{PB}) is calculated by the following equation, and the evolution of CO via the *Boudouard* reaction was detected by analyzing the outlet gas stream.

Carbon conversion:

$$X_{PB} = \frac{moles\ of\ carbon\ in\ the\ product\ CO}{moles\ of\ carbon\ in\ the\ feed} \times 100\%$$

Reaction equation:

$$C + CO_2 \rightarrow 2CO \quad \begin{cases} 1C \rightarrow 1CO \\ 1\ CO_2 \rightarrow 1\ CO \end{cases}$$

Sample	RHC supported Ni catalyst
Amount of sample for each run	300mg
Temperature	800℃, 900℃
concentration of Ni loading	0%, 3%, 5%, 10%
Carrier gas	Ar (50 ml/min)
CO_2 flow rate	200 ml/min

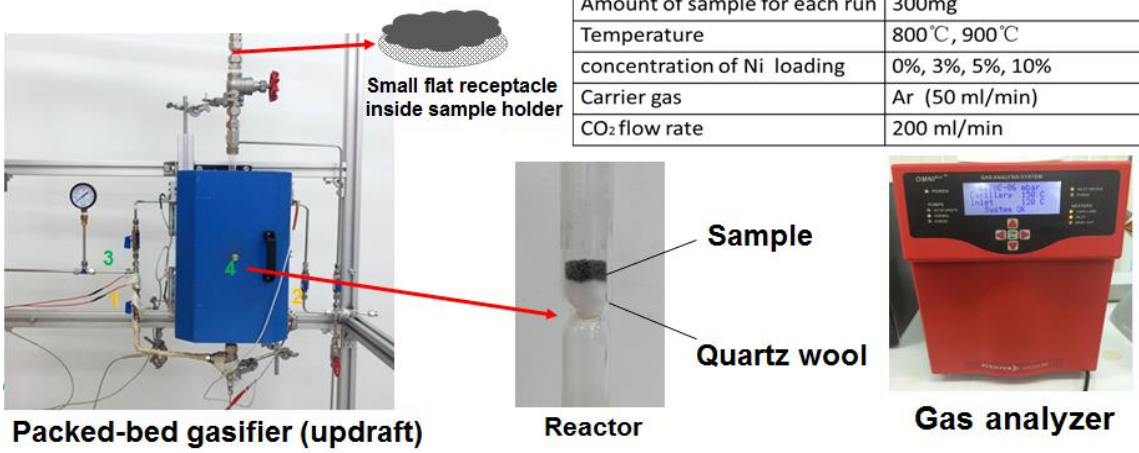

Figure 4.5 Snapshot of a lab-scale packed bed gasifier and the experimental conditions

4.3 Results and Discussions

4.3.1 Effect of Catalyst Weight

The weight of spent catalyst is an important parameter for the catalytic reforming of tar. If excessive catalysts are used, it is uneconomical for the tar catalytic reforming. Moreover, the gas percolation resistance to pass through the catalyst zone might be increased. In contrast, if insufficient catalysts are used, the tar reforming efficiency is lower. Moreover, the catalyst is easily deactivated due to the short retention time. In other word, the excessive catalyst can increase the contact frequency and reaction time of active sites with tar molecules, enhancing the catalytic performance. Fig. 4.6 shows the effect of the catalyst weight on the tar reforming efficiency at ~700 ^{o}C. The tar reforming efficiency was increased with the increase of the weight of used RHC Ni. The tar reforming efficiency

can reach about 50.1% by using 3 g of RHC Ni, while it was significantly increased, up to 90.5% and 99.8% by using 5 g and 10 g of RHC Ni, respectively. It might be attributed to the enhancement of the catalytic reaction and the retention time, which is caused by the increase of the catalyst weight. Furthermore, the tar reforming efficiency was not significantly reduced with a higher value of 99.3% after 5 cycles, indicating a high stability performance on the tar conversion.

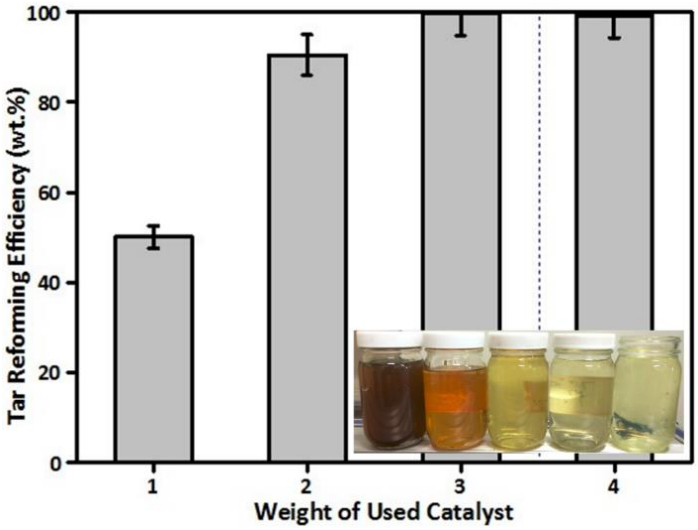

Figure 4.6 Effect of the catalyst weight [1: 3g; 2: 5g; 3: 10g; 4: 10g (5 cycles)] on the tar reforming efficiency

4.3.2 Effect of Catalytic Temperature

The catalytic temperature is another significant factor, because it directly influences the reaction activity. During the thermochemical reactions, high temperature could enhance the catalytic activity. Fig. 4.7 presents the effect of the reforming temperature on the tar conversion efficiency. The tar conversion efficiency generally increased with the increase of the reforming temperature. If the RHC Ni was used, the tar conversion efficiency can be significantly improved from 39.8% to 78.7% in the temperature range of 500-900 ^{o}C. Nevertheless, the tar conversion efficiency was not remarkably improved from 92.3% to 100% in the same temperature range. It means that the temperature can significantly affect the tar conversion efficiency, if no catalyst or RHC is employed. In addition, it can indicate that RHC Ni showed a higher catalytic activity for tar conversion even at lower temperatures.

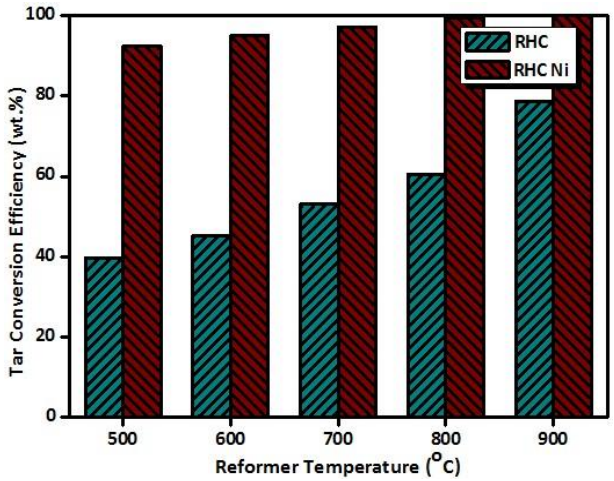

Figure 4.7 Effect of the reforming temperature on the tar conversion efficiency

4.3.3 Mass Balance

Gas, liquid and char are the main products from biomass pyrolysis or gasification. Liquid products including water and tar are not considerable products during biomass gasification, while the solid char could be fabricated into the value-added carbonaceous materials. Fig. 4.8A shows the yields of products derived from RH gasification at 750 ^{o}C. It can be found that the yield of pyrolysis char is not affected by using RHC or RHC Ni, which mainly depends on the biomass types and gasification conditions. The yield of char derived from RH pyrolysis at 750 ^{o}C was around 31.3-32.5%. However, the yields of liquid and producer gas had been changed significantly. In particular, if the RHC Ni was used for the catalytic reforming, the yield of liquid products was reduced from 30.2% to 10.7%, probably caused by the thermochemical reactions, such as the water-gas-shift reaction, the char gasification, and the tar reforming. Accordingly, the yield of the producer gas was greatly increased from 37.5% to 58.0% (Fig. 4.8B), in which the main components of the syngas are CO and H_2. From Fig. 4.8C, it can be found that using the RHC Ni, the volume fractions of CO and H_2 increased from 21.2% to 33.5% and from 18.5% to 24.3%, respectively. In addition, the volume fractions of CH_4, C_nH_m (i.e., C_2H_4, C_2H_6) and CO_2 were significantly reduced due to the catalytic reforming over the RHC Ni catalyst. It should be noted that RHC also exhibited a fixed catalytic activity for vapor conversion most likely due to the presence of trace minerals in it.

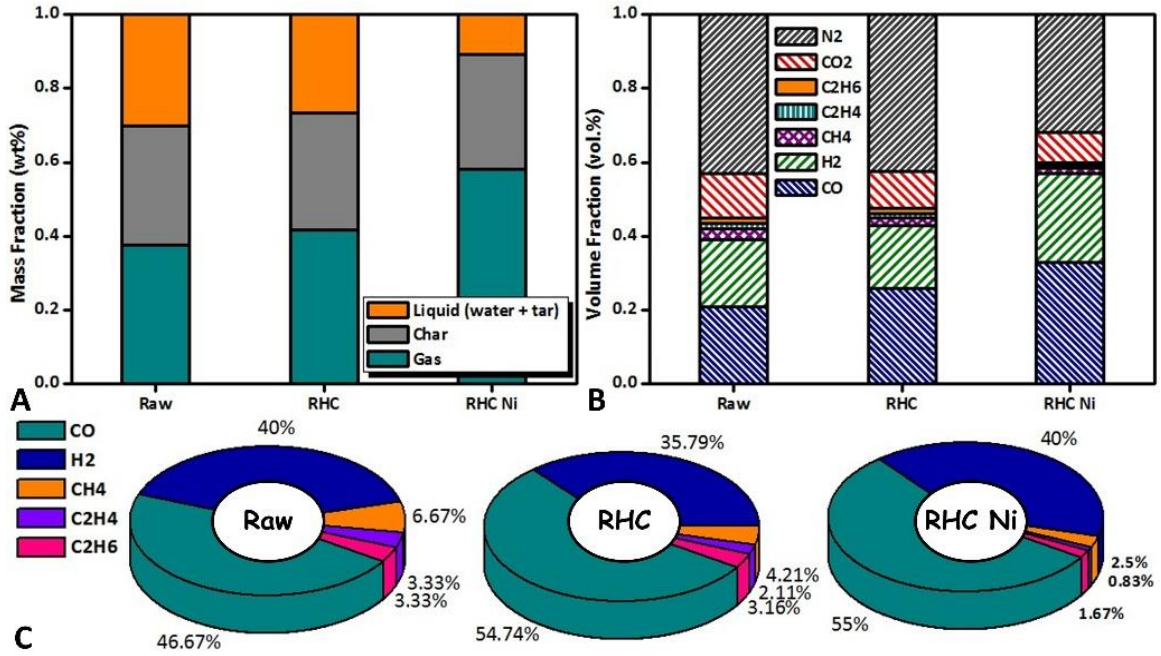

Figure 4.8 (A) Products yields and (B) composition of gas product derived from RH pyrolysis at 750 ^{o}C (reforming temperature: 700 ^{o}C, catalyst weight: 10 g); (C) Volume fraction of the syngas component

4.3.4 GC-MS Analysis of the Condensed Tar

Tars could be classified by their solubility and condensability [4-28], categorized into five classes (Fig. 4.9A). Class 1 refers to the GC undetectable heaviest tars, which can condense at high temperatures and very low concentrations; Class 2 refers to the heterocyclic aromatic compounds with high water solubility (e.g., phenol and cresol); Class 3 refers to the light hydrocarbons single-ring aromatic compounds (e.g., toluene and xylene); Class 4 refers to the light polyaromatic hydrocarbons (2-3 rings), which can condense at relatively high concentrations and intermediate temperatures (e.g., indene and naphthalene); Class 5 refers to the heavy polyaromatic hydrocarbons (4-7 rings), condensing at high temperatures and low concentrations (e.g., pyrene and coronene). Fig. 4.9B shows the GC-MS spectra of the condensed tar from RH pyrolysis at 750 ^{o}C. It could be observed that more than 117 absorbance peaks were detected. Likewise, Fig. 4.9C shows the GC-MS spectra of the condensed tar derived from RH pyrolysis-catalytic reforming by the RHC Ni at the same

temperature of 750 °C. In this case, the peak numbers are decreased to 37, indicating that the tar compounds was significantly reduced by the catalytic reforming. Meanwhile, these MS spectra were identified by the MS database. The most abundant organic components in the condensed tars were phenol, benzene, naphthalene, biphenylene, and their derivates. In particular, the naphthalene and its derivates occupied more than 30.26% in the tar sample 1 and 44.33% in the tar sample 2, respectively. However, the aromatic organic compounds consisting of PAHs, such as phenanthrene, pyrene, fluoranthene, existed in both of tar samples, indicating that it is difficult to convert them by means of the catalytic reforming. Furthermore, compared with the tertiary tars of PAHs, it is much easier to crack or reform the nascent tars by the RHC Ni. Moreover, the tertiary tars except for naphthalene were completely disappeared after the heterogeneous gasification process by the char and char-supported Ni catalysts. More significantly, the total amounts of tar by-products consisting of the tertiary tars were significantly reduced. CO_2 dry reforming can also reduce parts of nascent tar and convert them into thermally stable tertiary tar components such as toluene, naphthalene and styrene. Because of the corrosion, condensation, and deposition effects in syngas utilization, it is of great importance to reduce the PAHs content, especially in terms of these troublesome tars decomposed in the gasifier by the pyrolyzed biochar. In the reformer, the homogeneous partial oxidation and heterogeneous char conversion are two key factors to ensure that low-tar syngas is achieved. The selective properties of RHC Ni in eliminating the tertiary tars will significantly increase the application prospects of the gasifier [4-29]. In the present work, the major tar compounds came from tar Class 4; sometimes referred to as tertiary tars containing the non-oxygenated organic compounds with light PAHs. Among the compounds grouped in tar Class 4, the major contribution came from the naphthalene and its derivates. It can be indicated that RHC Ni showed the promising tar conversion efficiency on the GC-MS detected tars.

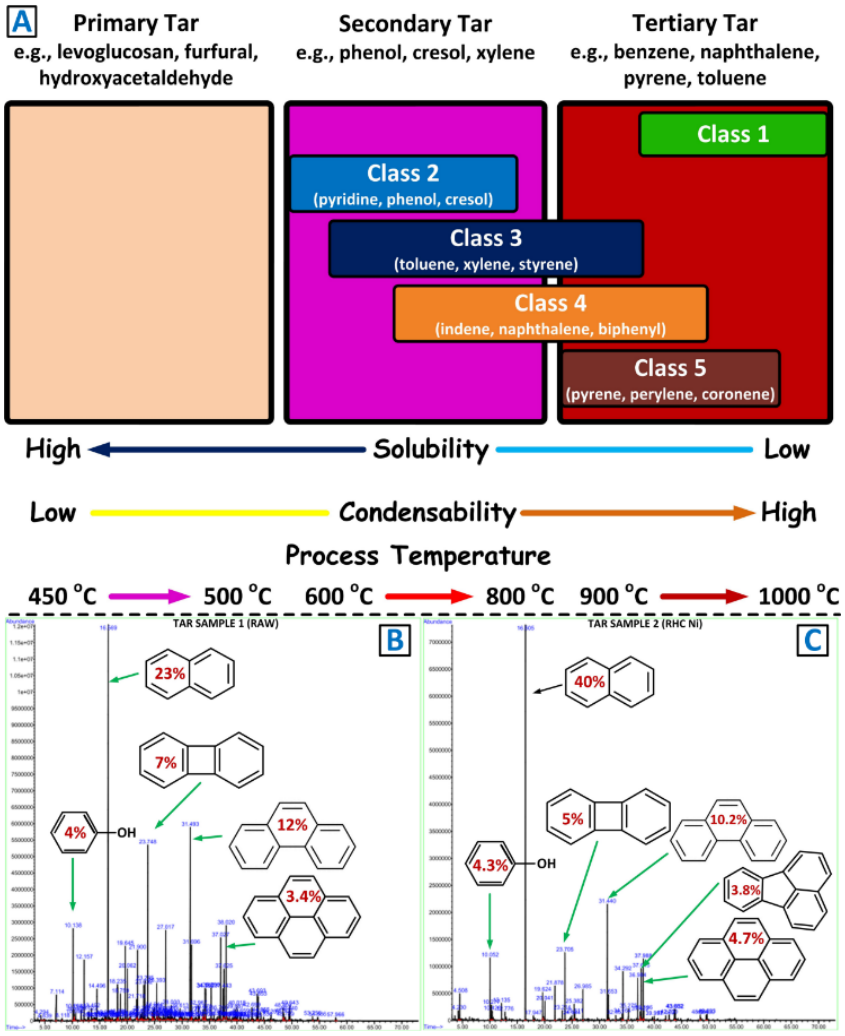

Figure 4.9 (A) Two typical classification methods of biomass tar; GC-MS spectra identified for main organic compounds in the condensed tar samples derived from RH pyrolysis (B) combined with RHC Ni catalytic reforming (C)

4.3.5 Characterization of RHC Ni

4.3.5.1 XRD analysis

The identification of crystal phases was conducted by XRD analysis using Rigaku D/Max 3400 powder diffraction system with Cu K_α radiation (λ = 0.1542 nm) at 45 kV and 40 mA with a scanning rate of 5^o/min. Fig. 4.10 shows the XRD patterns of the fresh and used RHC Ni catalysts. Silica (SiO_2) in all samples is amorphous structures. However, the typical silica characteristic is observed at a broad

peak centered at 2ϑ = 22.5°, which can be attributed to the presence of disordered cristobalite [4-30], [4-31]. The main chemical states of nickel in the RHC Ni catalysts were the nickel oxides (e.g., NiO, bunsenite) and metallic nickel (Ni^0) by the reactions (R1)-(R4). Initially, the nickel cations (Ni^{2+}) in the aqueous solution were transformed into the relative stable form of $Ni(H_2O)_6^{2+}$ (octahedral water coordination complexes) [4-32], which was therefore decomposed into the bunsenite (i.e., NiO). With the increase of the pyrolysis time, more nickel oxides (NiO) embedded in the carbon matrix of RHC were reduced into the metallic nickel (Ni^0) by the carbothermal reduction (R5 and R6) [4-7] and the hydrogenation reduction (R7). As shown in Fig. 4.10, the characteristic peaks of crystalline Ni^0 appeared after the pyrolysis of RH Ni [4-33]. After used for the catalytic reforming, the intensity of Ni^0 characteristic peaks in the RHC Ni2 became much stronger indicating its well crystallization. However, the size of nickel nanoparticles was not significantly changed.

Carbothermal reduction:

$$NiO + C \rightarrow Ni + CO \quad (R5)$$

$$NiO + CO \rightarrow Ni + CO_2 \quad (R6)$$

Hydrogenation reduction

$$NiO + H_2 \rightarrow Ni + H_2O \quad (R7)$$

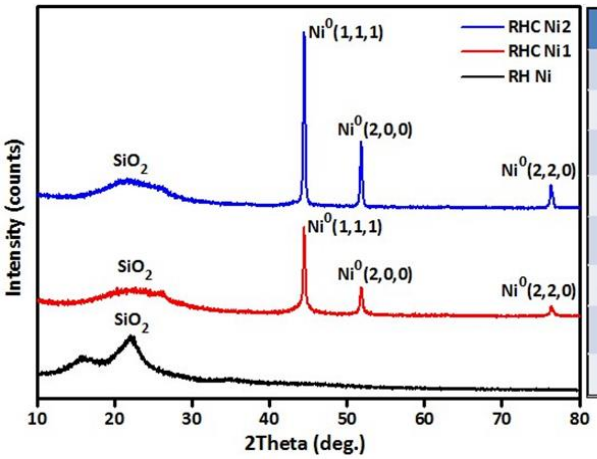

2θ (deg.)	Diameter (nm)	Phase Name
RHC Ni 1		
44.43	2.04	Nickel, syn (1,1,1)
51.80	1.76	Nickel, syn (2,0,0)
76.31	1.25	Nickel, syn (2,2,0)
RHC Ni 2		
44.44	2.04	Nickel, syn (1,1,1)
51.80	1.76	Nickel, syn (2,0,0)
76.33	1.25	Nickel, syn (2,2,0)

Figure 4.10 XRD patterns of the RHC, RHC Ni1 (fresh) and RHC Ni2 (used) catalysts

4.3.5.2 SEM analysis

Rice is one of the most widespread food crops for human sustenance. The content of RH reaches ~20 wt% of the entire rice kernel, a very large amount, considering the massive scale of global rice production. Moreover, RH contains a variety of components such as lignin (20-30 wt.%), cellulose (55-65 wt%), and silica (15-20 wt%), originating from monosilicic acid that is initially introduced into rice plants through their roots and is then moved to the rigid outer epidermal walls of the plants where it is converted into silica (Fig. 4.10B). As shown in Fig. 4.11C, silicon (Si) exists along the outer rugged surfaces of RH [4-34]. Typically, RH has a globular structure in nature, of which its main components are in the lemma/palea form, tightly interlocked with each other [4-35]. The corrugate structural outer epidermis is highly ridged, while its ridges are punctuated with the prominent globular protrusions. However, RH is assembled around the Si-O carcass, which is concentrated in the protuberances and hairs (trichomes) on the outer and inner epidermis, adjacent to the rice kernel. Many cavities having varying particle sizes were distributed within the char samples, as evidenced of the interconnected porous network and large specific surface area [4-36]. With the development of the reaction, the surface texture of char becomes irregularity ascribed to the shrinkage of the globular structure, which is caused by devolatilization [4-37]. Evaporation of volatile materials could create new pores on the particle with rough surface and irregular outlet (Fig. 4.11D). The external surface is found to be covered mostly with smooth open pores of different sizes (Fig. 4.11, D-G). Moreover, it appears that there was the possibility of fragmentation since several cracks passing through the particle could be observed clearly (Fig. 4.11, F-G). For the fresh and used RHC Ni samples, small particles with the globular shape could be observed by magnifying the above micrographs (Fig. 4.12). Some particles and clusters came from dust attached on the surface of parent RH. In addition, other larger clusters might be attributed to the soots formation and carbon deposits resulting from the hydrocarbons cracking [4-37], [4-38].

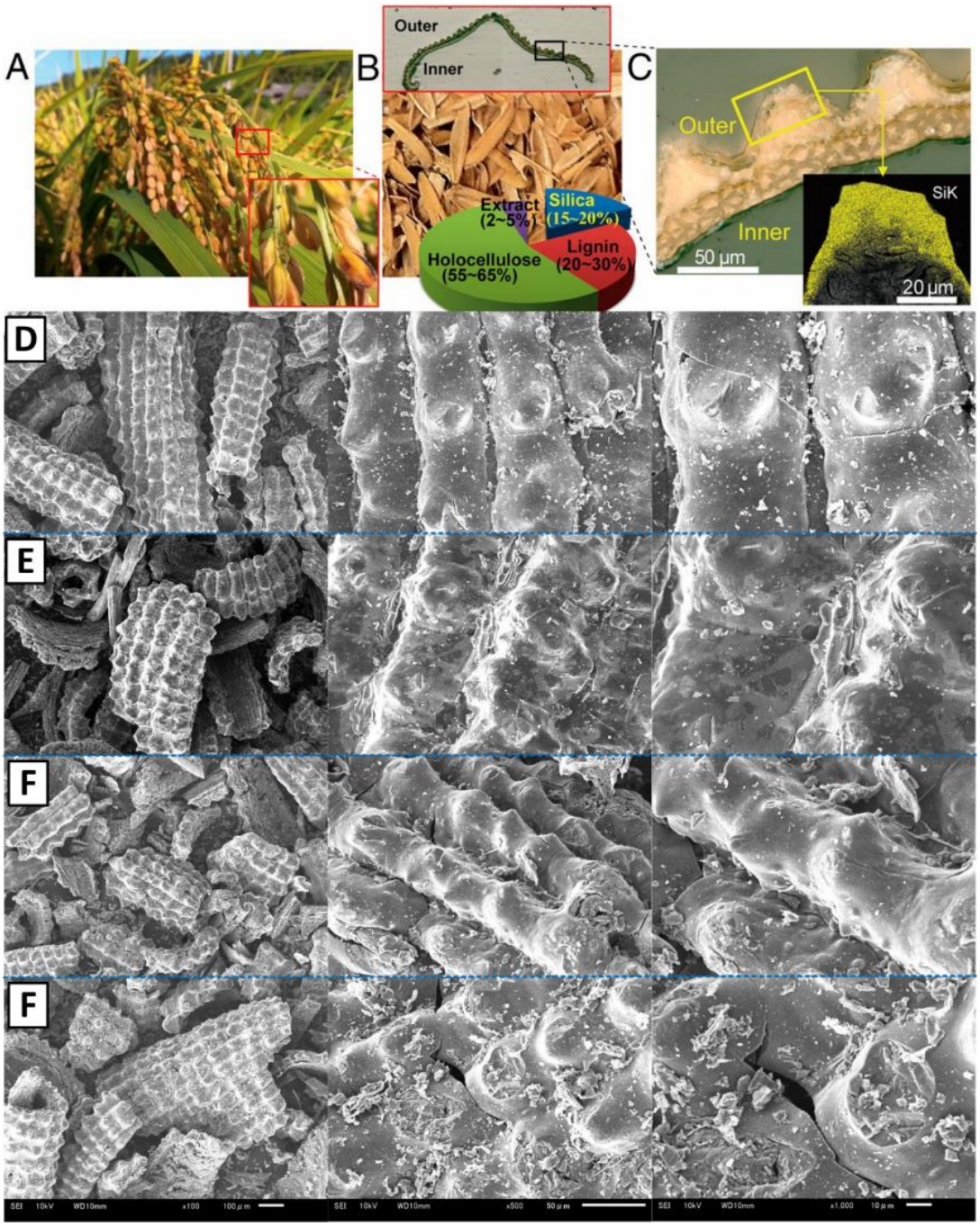

Figure 4.11 (*A*) Photographs of rice plant. (*B*) Photograph of RH. (*Upper Inset*): optical microscope image showing the morphological characteristic of outer/inner surfaces of RH; (*Lower Inset*): circular chart indicating the composition of RH. (*C*) Optical microscope image of a RH shell magnified from the black box in *B*. (*Inset*): Si-mapped SEM-EDS image. (*D-G*) SEM images of the RHC catalysts [RHC (D), fresh (E) and used (F & G) RHC Ni particles].

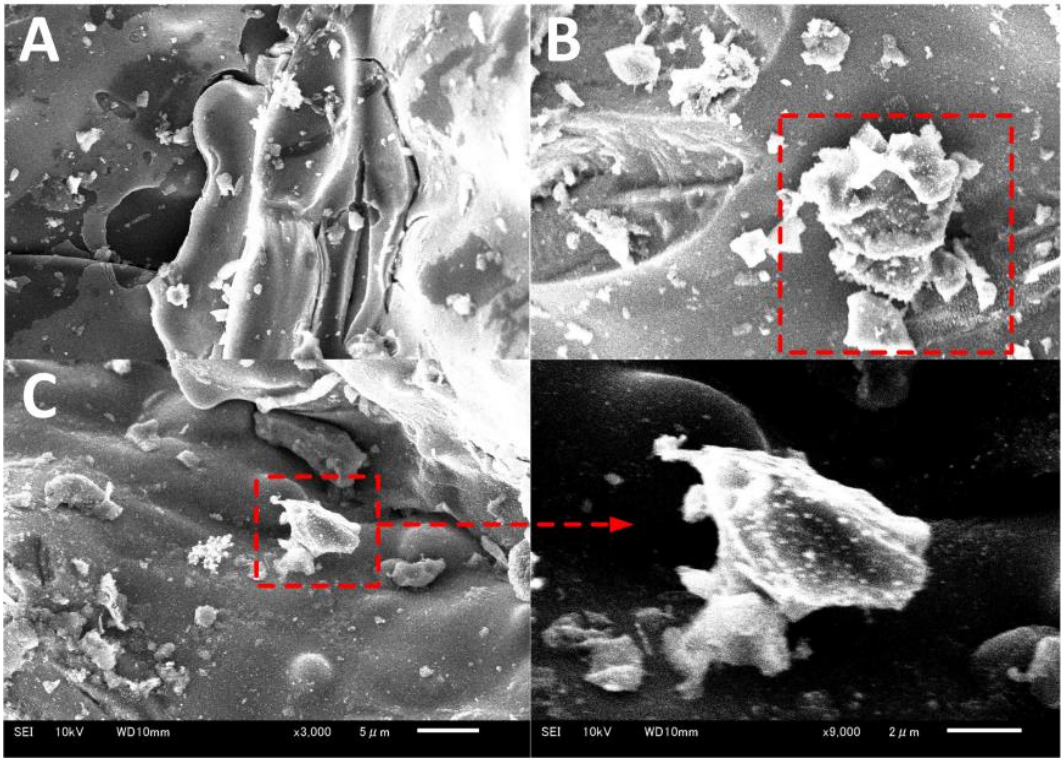

Figure 4.12 SEM images of the fresh (A) and used (B & C) RHC Ni catalysts

4.3.5.3 TEM analysis

Metallic nickel (Ni^0) nanoparticles could be dispersed uniformly in the carbon matrix of wood char obtained at the pyrolysis temperatures from 500 to 700 ^oC. However, the very wide dispersion of the monocrystalline metallic nickel (Ni^0) particles with the particle sizes of 2-4 nm could form at the pyrolysis temperatures ranging from 400 to 500 ^oC and their nanometric size confirmed the high dispersion of metal precursor in the wood obtained after the impregnation step [4-22], [4-32]. It could also be observed that nickel nanoparticles were embedded and highly dispersed in the carbon matrix with the particle sizes of around 10 nm (Fig. 4.13A). Nevertheless, these particle sizes became relatively non-uniform after the use (Fig. 4.13B), corresponding to the slight decrease of the particle size. Herein, the nickel nanoparticles with the particle size of 10-20 nm might be attributed to the coagulation with the nanosized amorphous carbon or silica. Furthermore, the carbon deposition on the surface of nickel particles could result in the increase of the particle size as well. It can also be

observed that some nanoparticles were encapsulated by the dark-colored substances after the use (Fig. 4.13B). The elemental constitutes were semi-quantitatively determined by the EDS analysis. The main elements in both fresh and used RHC Ni were carbon (C), silicon (Si) and nickel (Ni), etc. Also, a higher content of nickel (Ni) and a lower content of carbon (C) were detected in the used RHC Ni. Namely, the atomic ratio of Ni and C was increased after the use. It may be caused by the carbothermal reduction leading to the enhancement of carbon consumption and the formation of nickel nanoparticles. Since C, Si, and Ni are the predominate elements inside of the used RHC Ni, the silica-based nickel nanoparticles could be recycled and reused after carbon conversion.

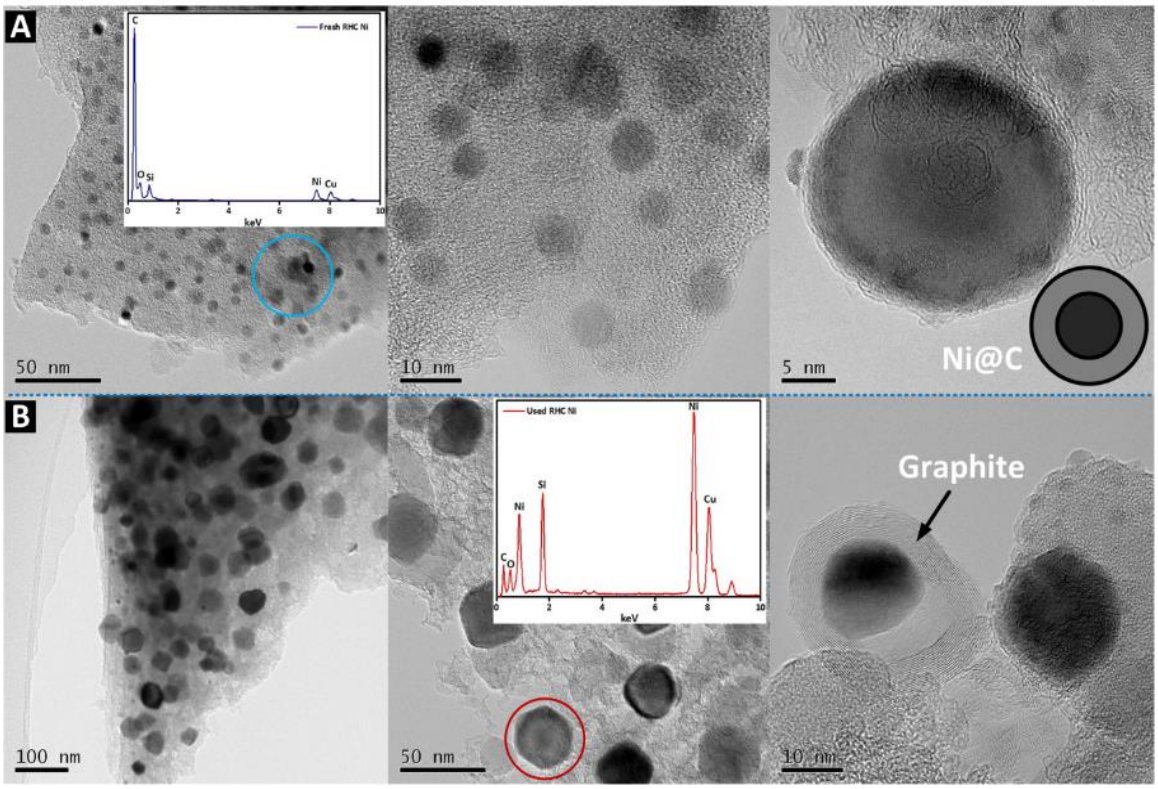

Figure 4.13 TEM-EDS analysis of (A) the fresh and (B) used RHC Ni catalysts

4.3.5.4 TG analysis

The thermal behavior of the fresh and the used RHC Ni catalysts were characterized by the TG analysis at the heating rate of 20 °C/min with the air flow rate of 150 mL/min. The TG curves of these samples are shown in Fig. 4.14A. The DTG curve of RHC had one sharp peak at ~400 °C due to

devolatilization and the combustion of volatiles and char (Fig. 4.14B). Significantly, the fixed carbon combustion was the dominant combustion process for biochar [4-39]. A larger mass loss of the fresh RHC Ni catalyst occurred in the temperature range of 300-500 °C, suggesting the presence of volatile matters in it, detectable even at the high temperature of 600 °C. Moreover, the total mass loss in these three samples was only 4-6% in the temperature range of 100-800 °C, indicating the thermal stability of the fresh and used RHC Ni catalysts. In the process of biomass catalytic pyrolysis, the aromatic compounds deposited on the catalyst can be generally eliminated over 350 °C [4-40]. It showed a stable mass loss rate for the used RHC Ni catalysts from 400 to 500 °C, possibly ascribed to the fixed carbon burn off. Basically, the burnout temperature of char and coke (R8) was over 500 °C [4-41], where the mass loss rate of the used 10g-RHC Ni was slow down, compared to the other used 3g- and 5g-RHC Ni catalysts. It indicated that hydrocarbons decomposition (R9) and the carbon deposition (R10) became much heavier when only the small amount of catalyst was employed. In addition, the carbon combustion appeared immediately after 400 °C, which can indicate that the amorphous carbons were formed during the pyrolysis of biomass [4-42]. .

$$C + O_2 \rightarrow CO_2 \quad \text{(carbon combustion)} \quad \text{(R8)}$$

$$C_nH_m \rightarrow C + H_2 + CH_4 + C_xH_y \quad \text{(R9)}$$

$$CH_4 \rightarrow C + 2\,H_2 \quad \text{(carbon deposition)} \quad \text{(R10)}$$

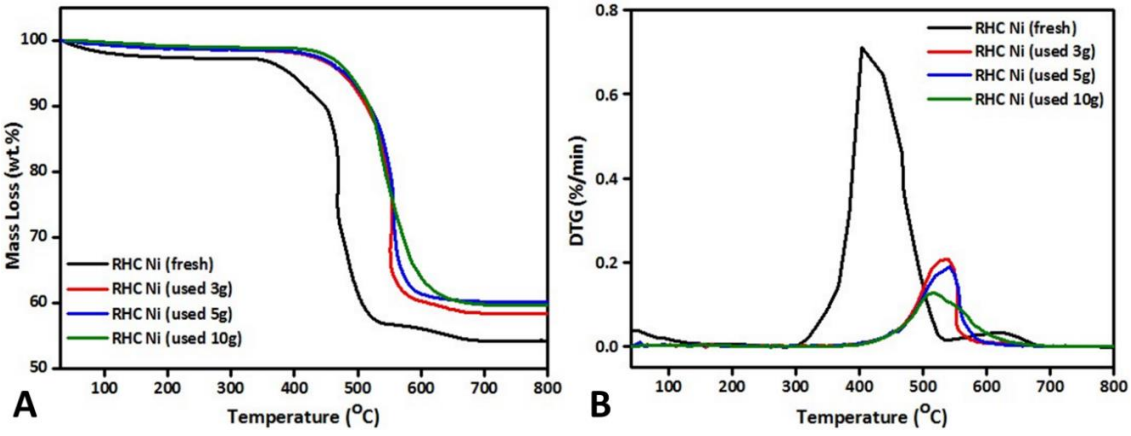

Figure 4.14 TG and DTG curves of the fresh and used RHC Ni

4.3.5.5 N_2 adsorption-desorption analysis

Table 5.1 presents the surface areas and the pore diameters of RHC, the fresh and used RHC Ni catalysts, which were analyzed using the nitrogen isothermal adsorption (77 K) as shown in Fig. 4.15A. RHC has a higher BET surface area (117.08 m^2/g) compared with the fresh RHC Ni catalyst (72.75 m^2/g), indicating that the metal (i.e., nickel) loading could decrease the surface area of char. The isotherms suggest the significant formation of mesopores during the reactions with the RHC Ni, because the isotherm curves resemble Type II isotherms after the catalytic reforming. In contrast, the fresh RHC Ni1 shows the Type I isotherm, more typical of a microporous structure. Moreover, an increase in the hysteresis elbow is clearly observed in the used RHC Ni2, indicating the widened mesopores and the possibility of deeper pore formations; accordingly, its BET surface area and the pore diameter increased from 72.75 m^2/g to 200.50 m^2/g and 0.12 m^2/g to 0.15 cm^3/g, respectively (Fig. 4.15B). Furthermore, the mass ratio of nickel in RHC Ni slightly decreased from 89.33 mg/g to 88.50 mg/g after it was used for the catalytic reaction. In general, the increase of the surface areas for the RHC Ni catalysts could be attributed to the formation of new pores by further decomposition, corresponding to the soot gasification rate higher than the deposition rate (Fig. 4.15C).

Table 5.1 Surface Areas, Pore Diameters and Nickel Mass Ratio of RHC, RHC Ni1 and RHC Ni2

Catalyst	Total pore volume (cm^3/g)	Average pore diameter (nm)	BET surface area (m^2/g)	Ni/RHC (mg/g)
RHC	*0.13*	*2.7*	*117.08*	*0*
RHC Ni1	*0.12*	*2.9*	*72.75*	*52.38*
RHC Ni2	*0.15*	*3.5*	*200.50*	*52.35*

Note:
1. RHC Ni1 was the fresh catalyst, and RHC Ni2 was the used 10 g catalyst after 5 cycles;
2. The BET surface areas (m^2/g) of the fresh and used RHC Ni catalysts after 1 cycle were as follows: fresh - 72.75, 3 g - 107.96, 5 g - 143.60, 10 g - 185.36;
3. The Langmuir surface areas (m^2/g) of the fresh and used RHC Ni catalysts after 1 cycle were as follows: fresh - 103.91, 3 g - 152.62, 5 g - 200.10, 10 g - 280.25.

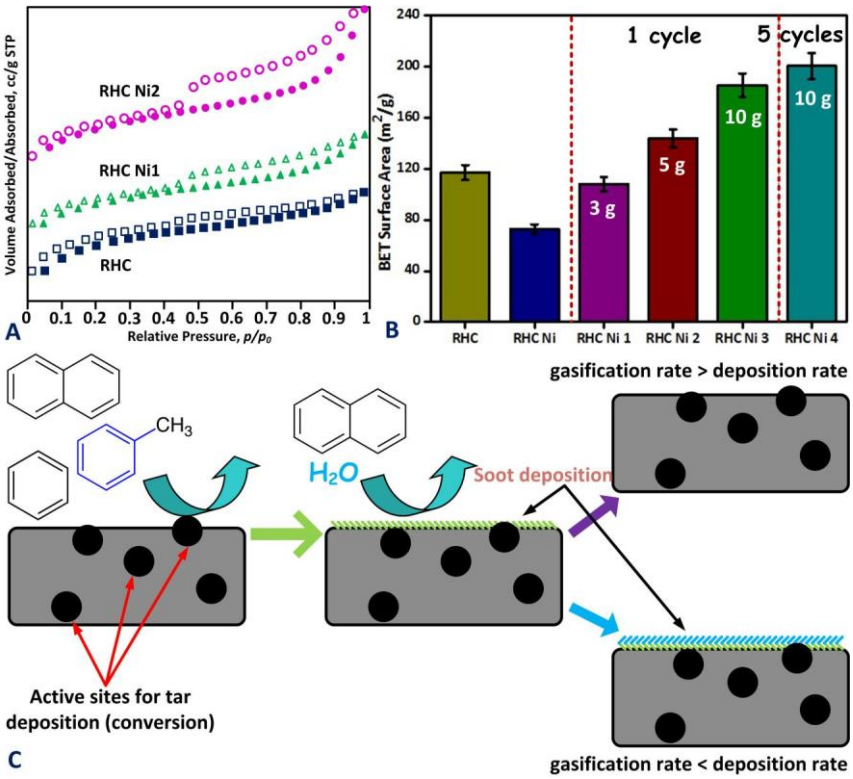

Figure 4.15 (A) N_2 adsorption-desorption curves of RHC, RHC Ni1 and RHC Ni2. (B) BET surface areas of RHC, the fresh and used RHC Ni; (C) Char gasification and carbon deposition

4.3.6 Integrated Catalytic Pyrolysis and Gasification Concept

The integrated strategy of the catalytic biomass gasification includes different key reaction steps as illustrated in Fig. 4.16, including (step 1) the metal precursor (e.g., Ni^{2+}) insertion to biomass, (step 2) the catalytic pyrolysis of biomass, (step 3) the catalytic nanoparticles (e.g., Ni^0) *in situ* generated and highly dispersed in the carbon matrix, (step 4) the catalytic conversion of tars by the formed nanoparticles, (step 5) the catalytic gasification of the char residue, and (step 6) the recycling and the reuse of the metal species in the ash (e.g., NiO/SiO_2). Each of these reaction steps requires a fundamental understanding to develop a new high-efficiency biomass pyrolysis/gasification process at nanoscales. Moreover, it is critical to develop the breakthrough conversion technologies with the design of the future intensified gasification processes.

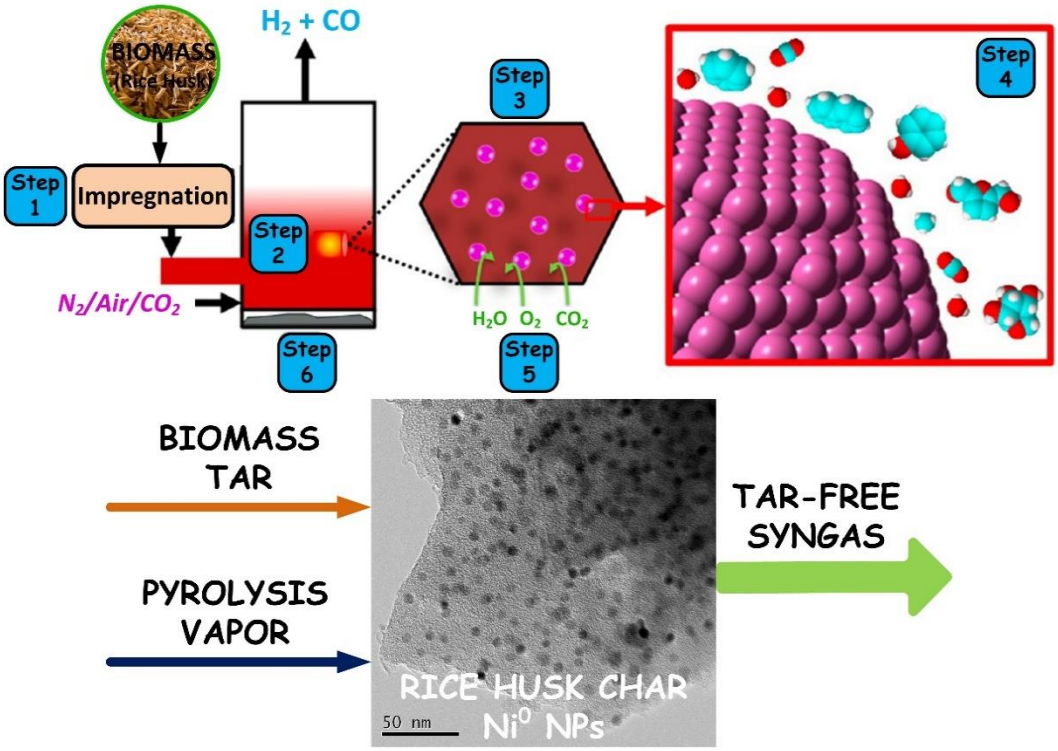

Figure 4.16 Integrated strategy of biomass catalytic pyrolysis/gasification

In this work, the metallic nickel (Ni^0) nanoparticles had been successfully embedded into the carbon matrix, which was employed for the catalytic conversion of tar derived from biomass gasification. The reactions in the second stage mainly include the tar cracking and reforming. The tertiary tar in R11 implies the total tar yields after different conditions. Besides tertiary tar, noncondensable gases such as CO, CO_2, H_2O, CH_4, C_nH_m, and H_2 are yielded as well. As for the important syngas components, these products formation will increase the tar conversion efficiency of the gasifier. The reforming effects of CO_2 on tar evolution is most likely caused by the hydroxy (OH) radicals produced from CO_2 during the thermal conversion of syngas. A higher concentration of OH radicals can enhance the oxidation process of tar compounds [4-43]. Over the RHC Ni, the dry reforming is significantly enhanced (R12). Herein, less water (H_2O) originated from biomass decomposition can enhance the nascent tar reforming and inhibit the polymerization reactions ascribed to more hydrogen produced by the reactions of R13-R18. Additionally, the presence of CO_2 or H_2O can influence the formation of other noncondensable aromatic hydrocarbons. However, gas molecules in the outlet of gasifier

are present in a relatively stable composition, possibly attributed to these reversible reactions (R13-R17). In the reforming zone, the biochar heterogeneous gasification is the dominant endothermic reaction, which is of benefit to the char conversion efficiency (R18 and R19) normally occurring at relatively high temperatures. Without sufficient energy, the proceeding of char/carbon gasification reactions such as *Boudouard reaction* will be inhibited or occurred with low-efficiency. Additionally, the process of pyrolysis or gasification combined with the catalytic reforming was conducted in an inert gas condition (e.g., N_2), so the RHC supported catalysts was not greatly consumed, contributing to the extension of the service life. However, the RHC Ni can be deactivated by the carbon deposition on the surfaces of metal actives. Consequently, the deposited carbon and the char could be directly catalytically gasified into the additional syngas by the gasification agents, such as CO_2, H_2O, thereby inhibiting its deactivation by producing new pores [4-44], [4-45].

Tar decomposition:	
Nascent tar + CO_2/H_2O/RHC → Tertiary tar + CO + H_2 + CO_2 + H_2O + C_nH_m + CH_4	(R11) [29]
Nascent tar + CO_2/H_2O/RHC Ni → CO + H_2 + CO_2 + H_2O + C_nH_m + CH_4	(R12)
Gas reforming:	
n CO_2 + C_nH_m ↔ 2n CO + m/2 H_2	(R13)
n H_2O + C_nH_m ↔ n CO + (n+m/2) H_2	(R14)
CH_4 + H_2O ↔ CO + 3 H_2	(R15)
CH_4 + CO_2 ↔ 2 CO + 2 H_2	(R16)
CO + H_2O ↔ CO_2 + H_2	(R17)
Char gasification (char present):	
C + CO_2 ↔ 2 CO	(R18)
C + H_2O ↔ CO + H_2	(R19)

4.3.7 Nickel-catalyzed CO_2 Gasification of RHC

Gasification temperature is known to be one of the most influential parameters in controlling the gasification reaction rate. Based on this knowledge, the gasification temperature was varied in the range of 700-1000 ^oC. In addition, the nickel catalyst loading in the range of 0-10% was investigated in the isothermal gasification. Fig. 4.17 shows the carbon conversion of CO_2 gasification of RHC Ni. The results confirmed the pronounced effect of the gasification temperature on promoting the char reactivity. Without adding nickel catalyst, the carbon conversion efficiency of 100% was achieved in 40 min at 1000 ^oC, whereas this time was prolonged to 130 min at 700 ^oC. Although the use of high temperatures improved the char reactivity by reducing the activation energy, however, it was speculated that relative high temperatures could shift the reaction rate towards the pore diffusion controlled regime. Besides, the addition of nickel catalyst could improve the char reactivity by reducing the activation energy. As shown in Fig. 4.17, the carbon conversion rate is remarkably increased by adding the nickel catalyst in the different gasification temperatures. In particular, the carbon conversion efficiency of 100% can be achieved in almost 10 min at 1000 ^oC by loading the nickel catalyst (Fig. 4.17A). Moreover, it indicated that the loading amount of nickel catalyst had trifling impact on the carbon conversion rate at very high temperatures (>1000 ^oC). As the decrease of gasification temperature, the catalytic effect of nickel was significantly reduced. The carbon conversion rate was not greatly decreased for 10% loading of nickel catalyst, while it was decreased for 3% and 5% loading of nickel catalyst at 900 ^oC (Fig. 4.17B). It is noted that, when loading 3% and 5% of nickel catalysts, the carbon conversion rates were similar at 800 ^oC and 900 ^oC, respectively (Fig. 4.17C). Subsequently, Fig. 4.18 presents the carbon conversion and the CO generation rates originated from CO_2 gasification of RHC Ni at 900 ^oC in a packed bed reactor. The carbon conversion rates are slightly lower than those in TGA, possibly influenced by the operating conditions, such as the CO_2 flow rate. As for the used RHC Ni (about 5%) for the tar reforming, the carbon conversion efficiency of 100% can be achieved around 30 min at 900 ^oC for CO_2 gasification.

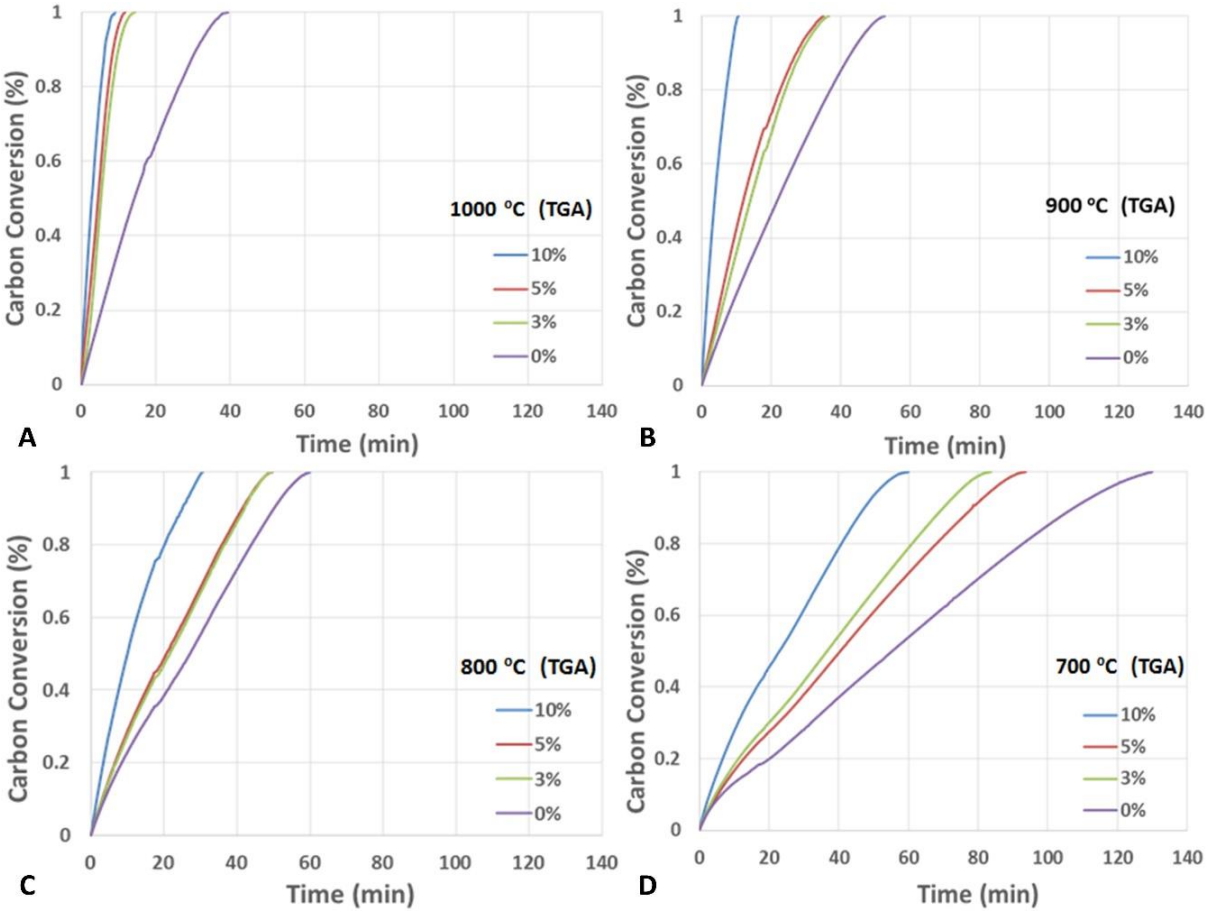

Figure 4.17 Carbon conversion of CO_2 gasification of RHC Ni at 700-1000 °C (A-D) by TGA

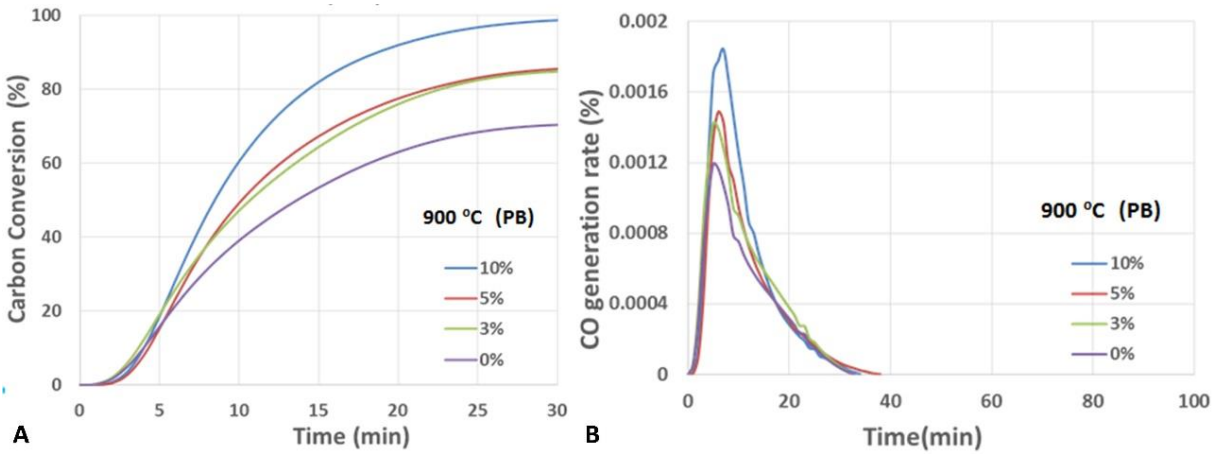

Figure 4.18 Carbon conversion (A) and CO generation rates (B) of CO_2 gasification of RHC Ni at 900 °C in a packed bed (PB) reactor

The fresh RHC Ni, the used RHC Ni and the remaining ashes (i.e., RHA Ni) from CO_2 gasification at 900 ^oC were characterized by the XRD analysis (as shown in Fig. 4.19). It could be clearly observed that RHC Ni1 and RHC Ni2 exhibited similar patterns with four sharp peaks. The first peak appeared at 22° is due to the presence of cristobalite silica, and the second weak peak at 26.6° can be assigned to the crystalline graphitic carbon. Besides, three sharp peaks appeared at 44.43°, 51.8° and 76.31°, respectively, are the characteristic peaks of crystalline metallic nickel (Ni^0). After CO_2 gasification completely, the characteristic peak intensity of cristobalite silica was enhanced, indicating its well crystallization, whereas the characteristic peak of crystalline graphitic carbon disappeared due to the carbon conversion. It is noted that the characteristic peaks of Ni^0 became weak or disappeared, whilst more characteristic sharp peaks of bunsenite (NiO) appeared at 37.17°, 43.24°, 62.87°, and 75.37°, respectively. It suggests that the metallic nickel (Ni^0) is oxidized into the nickel oxide (NiO) after CO_2 gasification at high temperatures. The mechanisms can be concluded as the following equation (20)-(22). Initially, the CO_2 concentration is much higher than the CO concentration in this system, which promotes the reversible reactions (20) and (21) to transform Ni^0 into NiO and Ni_2O_3 [4-46]. Furthermore, the crystal components in the RHA Ni are very pure, mainly composed of NiO and SiO_2. Based on the reported works, it has a potential to reuse a silica-based nickel catalysts [4-47], [4-48], in terms of the tar catalytic reforming [4-49].

$$Ni + CO_2 \rightarrow NiO + CO \quad (20)$$

$$2NiO + CO_2 \rightarrow Ni_2O_3 + CO \quad (21)$$

$$Ni_2O_3 + C \rightarrow 2NiO + CO \quad (22)$$

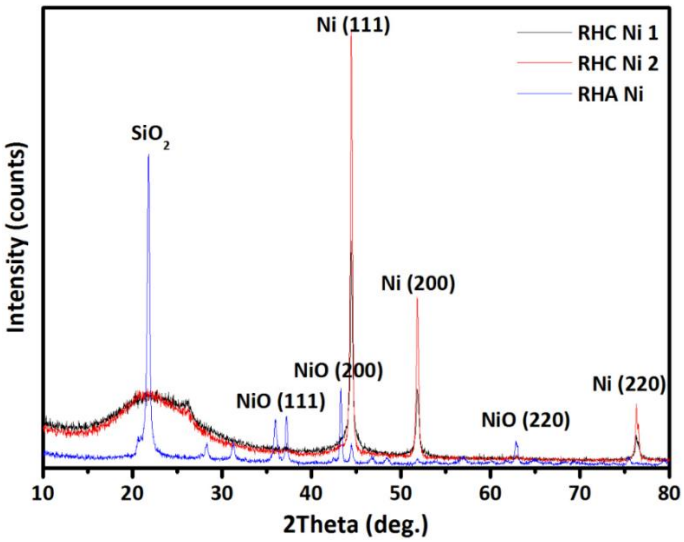

Figure 4.19 XRD patterns of RHC Ni1 (fresh), RHC Ni2 (used) and RHA Ni (after CO_2 gasification)

4.4 Conclusions

Metallic nickel (Ni^0) nanoparticles could be successfully *in situ* generated in the amorphous carbon matrix via the carbothermal reduction by using waste biomass as a carbon source. Ni^0 nanoparticles are embedded and highly dispersed in the RHC matrix with the particle size of around 10 nm. The RHC Ni exhibited a good performance on the tar catalytic reforming. In particular, the tar conversion efficiency increased with the increase of the catalyst weight and the reforming temperature. The tar reforming efficiency can reach about 50.1% by using 3 g of RHC Ni, while it significantly increased, up to 99.8% by using 10 g of RHC Ni, maintaining a higher value of 99.3% after 5 cycles. It might be attributed to the enhancement of the catalytic reaction and the retention time. Besides, if 10 g of RHC Ni used, the tar conversion efficiency could improve from 92.3% to 100% in the temperature range of 500-900 ^oC. It can suggest that RHC Ni showed a higher catalytic reactivity for tar conversion even at lower temperatures (>500 ^oC). More importantly, without using the RHC Ni, more PAHs can be formed. Compared to the tertiary tar compounds of PAHs, it is much easier to crack/reform the nascent tar compounds by RHC Ni. If the RHC Ni was used for catalytic reforming, the yield of liquid products decreased from 30.2% to 10.7%; accordingly, the yield of gas product was greatly increased

from 37.5% to 58.0%. Among these gas molecules, the volume fractions of CO and H_2 were increased from 21.2% to 33.5% and from 18.5% to 24.3%, respectively, attributed to the catalytic reforming over the RHC Ni. Moreover, the RHC Ni catalyst could be deactivated caused by the coke deposition on the surface of metal actives. Consequently, the waste RHC Ni could be catalytically gasified into the syngas, accompanied by recycling of the silica-based nickel nanocomposites. Furthermore, the catalytic kinetics and service life should be studied in a continuous pyrolysis-reforming facility.

References

[4-1] W.F. Fassinou, L. Van den Steene, S. Toure, G. Volle, P. Girard, Pyrolysis of *Pinus pinaster* in a two-stage gasifier: Influence of processing parameters and thermal cracking of tar. *Fuel Processing Technology* 2009, 90, 75-90.

[4-2] J.F. González, S. Roman, G. Engo, J.M. Encinar, G. Martinez, Reduction of tars by dolomite cracking during two-stage gasification of olive cake. *Biomass Bioenergy* 2011, 35, 4324-4330.

[4-3] J. Šulc, J. Stojdl, M. Richter, J. Popelka, K. Svoboda, J. Smetana, et al. Biomass waste gasification - Can be the two stage process suitable for tar reduction and power generation? *Waste Management* 2012, 32, 692-700.

[4-4] C. Wu, L.Z. Wang, P.T. Williams, J. Shi, J. Huang, Hydrogen production from biomass gasification with Ni/MCM-41 catalysts: Influence of Ni content. *Applied Catalysis B: Environmental* 2011, 108, 6-13.

[4-5] X. Xiao, X. Meng, D. Dung, T. Takarada, Two-stage steam gasification of waste biomass in fluidized bed at low temperature: Parametric investigations and performance optimization. *Bioresource Technology* 2011, 102, 1975-1981.

[4-6] Y. Shen, P. Zhao, Q. Shao, D. Ma, F. Takahashi, K. Yoshikawa, In-situ catalytic conversion of tar using rice husk char-supported nickel-iron catalysts for biomass pyrolysis/gasification. *Applied Catalysis B: Environmental* 2014, 152-153, 140-151.

[4-7] Y. Shen, K. Yoshikawa, Tar conversion and vapor upgrading via in-situ catalysis using silica-based nickel nanoparticles embedded in rice husk char for biomass pyrolysis/gasification. *Industrial & Engineering Chemistry Research* 2014, 53, 10929-10942.

[4-8] F.A. Agblevor, S. Beis, O. Mante, N. Abdoulmoumine, Fractional catalytic pyrolysis of hybrid poplar wood. *Industrial & Engineering Chemistry Research* 2010, 49, 3533-3538.

[4-9] M. Chen, J. Wang, M. Zhang, M. Chen, X. Zhu, F. Min, et al. Catalytic effects of eight inorganic additives on pyrolysis of pine wood sawdust by microwave heating. *Journal of Analytical and Applied Pyrolysis* 2008, 82, 145-150.

[4-10] D. Carpenter, T.L. Westover, S. Czernik, W. Jablonski, Biomass feedstocks for renewable fuel production: a review of the impacts of feedstock and pretreatment on the yield and product distribution of fast pyrolysis bio-oils and vapors. *Green Chemistry* 2014, 16, 384-406.

[4-11] R. French, S. Czernik, Catalytic pyrolysis of biomass for biofuels production. *Fuel Processing Technology* 2010, 91, 25-32.

[4-12] O.D. Mante, F.A. Agblevor, R. McClung, Fluid catalytic cracking of biomass pyrolysis vapors. *Biomass Conversion & Biorefinery* 2011, 1, 189-201.

[4-13] S. Liu, Y. Wang, R. Wu, X. Zeng, S. Gao, G. Xu, Fundamentals of catalytic tar removal over in situ and ex situ chars in two-stage gasification of coal. *Energy Fuels* 2014, 28, 58-66.

[4-14] F. Dabai, N. Paterson, M. Millan, P. Fennell, R. Kandiyoti, Tar formation and destruction in a fixed bed reactor simulating downdraft gasification: effect of reaction conditions on tar cracking products. *Energy Fuels* 2014, 28, 1970-1982.

[4-15] R.B. Cahyono, G. Saito, N. Yasuda, T. Nomura, T. Akiyama, Porous ore structure and deposited carbon type during integrated pyrolysis-tar decomposition. *Energy Fuels* 2014, 28, 2129-2134.

[4-16] A. Gomez-Barea, B. Leckner, *Gasification of Biomass and Waste*. Handbook of Combustion 2010, Vol. 4: Solid Fuels, Edited by Maximilian Lackner, Franz Winter, and Avinash K. Agarwal. WILEY-VCH.

[4-17] S.A. Davis, M. Breulmann, K.H. Rgodes, B. Zhang, S. Mann, Template-directed assembly using nanoparticle building blocks: a nanotectonic approach to organized materials. *Chemistry of Materials* 2001, 13, 3218-3226.

[4-18] Y. Shin, C. Wang, G.J. Exarhos, Synthesis of SiC ceramics by the carbothermal reduction of mineralized wood with silica. *Advanced Material* 2005, 17, 73-77.

[4-19] C.I. Lin, L.H. Wang, Adsorption of nickel (II) ion from aqueous solution using rice hull ash. *Journal of Chemical Engineering of Japan* 2011, 44, 278-285.

[4-20] V.C. Srivastava, I.D. Mall, I.M. Mishra, Characterization of mesoporous rice husk ash (RHA) and adsorption kinetics of metal ions from aqueous solution onto RHA. *Journal of Hazardous Material* 2006, B134, 257-267.

[4-21] L. Lin, S.R. Zhai, Z.Y. Xiao, Y. Song, Q.D. An, X.W. Song, Dye adsorption of mesoporous

activated carbons produced from NaOH-pretreated rice husks. *Bioresource Technology* 2013, 136, 437-443.

[4-22] Y. Richardson, J. Blin, G. Volle, J. Motuzas, A. Julbe, In situ generation of Ni metal nanoparticles as catalyst for H_2-rich syngas production from biomass gasification. *Applied Catalysis A: General* 2010, 382, 220-230.

[4-23] L.S. Lobo, Instrinsic kinetics in carbon gasification: Understanding linearity “nanoworms” and alloy catalysts. *Applied Catalysis B: Environmental* 2014, 148-149, 136-143.

[4-24] S. Yuan, X. Chen, J. Li, F. Wang, CO_2 gasification kinetics of biomass char derived from high-temperature rapid pyrolysis. *Energy Fuels* 2011, 25, 2314-2321.

[4-25] Y. Huang, X. Yin, C. Wu, C. Wang, J. Xie, Z. Zhou, L. Ma, H. Li, Effects of metal catalysts on CO_2 gasification reactivity of biomass char. *Biotechnology Advances* 2009, 27, 568-572.

[4-26] P. Lahijani, Z.A. Zainal,A.R. Mohamed, Catalytic effect of iron species on CO_2 gasification reactivity of oil palm shell char. *Thermochimica Acta* 2012, 546, 24-31.

[4-27] P. Lahijani, Z.A. Zainal, A.R. Mohamed, M. Mohammadi, CO_2 gasification reactivity of biomass char: Catalytic influence of alkali, alkaline earth and transition metal salts. *Bioresource Technology* 2013, 144, 288-195.

[4-28] J.H.A. Kiel, Primary measures to reduce tar formation in fluidised-bed biomass gasifiers. Final Report SDE Project P1999-012. Netherlands Energy Research Foundation; 2004.

[4-29] W. Wu, Y. Luo, Y. Su, Y. Zhang, S. Zhao, Y. Wang, Nascent biomass tar evolution properties under homogeneous/heterogeneous decomposition conditions in a two-stage reactor. *Energy Fuels* 2011, 25, 5394-5406.

[4-30] T. Liou, Preparation and characterization of nano-structured silica from rice husk. *Materials & Science Engineering: A* 2004, 364, 313-323.

[4-31] T. Liou, Evolution of chemistry and morphology during the carbonization and combustion of rice husk. *Carbon* 2004, 42, 785-794.

[4-32] Y. Richardson, J. Motuzas, A. Julbe, G. Volle, J. Blin, Catalytic investigation of in situ generated Ni metal nanoparticles for tar conversion during biomass pyrolysis. *Journal of Physical Chemistry C* 2013, *117*, 23812-23831.

[4-33] L. Li, K. Morishita, H. Mogi, K. Yamasaki, T. Takarada, Low-temperature gasification of a woody biomass under a nickel-loaded brown coal char. *Fuel Processing Technology* 2010, 91, 889-894.

[4-34] D.S. Jung, M.H. Ryou, Y.J. Sung, S.B. Park, J.W. Choi, Recycling rice husks for high-capacity lithium battery. *Proc. Natl. Acad. Sci. U.S.A.* 2013, 110, 12229-12234.

[4-35] B.D. Park, S.G. Wi, K.H. Lee, A.P. Singh, T.H. Yoon, Y.S. Kim, Characterization of anatomical features and silica distribution in rice husk using microscopic and micro-analytical techniques. *Biomass Bioenergy* 2003, 25, 319-327.

[4-36] M. Ahmaruzzaman, V.K. Gupta, Rice husk and its ash as low-cost adsorbents in water and wastewater treatment. *Industrial & Engineering Chemistry Research* 2011, 50, 13589-13613.

[4-37] S. Hu, J. Xiang, L. Sun, M. Xu, J. Qiu, P. Fu, Characterization of char from rapid pyrolysis of rice husk. *Fuel Processing Technology* 2008, 89, 1096-1105.

[4-38] J.M. Bermúdez, A. Arenillas, J.A. Menéndez, Syngas from CO_2 reforming of coke oven gas: Synergetic effect of activated carbon/Ni-γAl_2O_3 catalyst. *International Journal of Hydrogen Energy* 2011, 36, 13361-13368.

[4-39] Q. Yi, F. Qi, G. Cheng, Y. Zhang, B. Xiao, Z. Hu, et al. Thermogravimetric analysis of co-combustion of biomass and biochar. *Journal of Thermal Analysis and Calorimetry* 2013, 112, 1475-1479.

[4-40] X. Guo, Y. Zheng, B. Zhang, J. Chen, Analysis of coke precursor on catalyst and study on regeneration of catalyst in upgrading of bio-oil. *Biomass Bioenergy* 2009, 33, 1469-1473.

[4-41] Z.A. Mayer, A. Apfelbacher, A. Hornung, A comparative study on the pyrolysis of metal- and ash-enriched wood and the combustion properties of the gained char. *Journal of Analytical and Applied Pyrolysis* 2012, 96, 196-202.

[4-42] P.H. Blanco, C. Wu, J.A. Onwudili, P.T. Williams, Characterization and evaluation of Ni/SiO_2 catalysts for hydrogen production and tar reduction from catalytic steam pyrolysis-reforming of refuse derived fuel. *Applied Catalysis B: Environmental* 2013, 134-135, 238-250.

[4-43] A. Dufour, S. Valin, P. Castelli, S.B. Thiery, G. Boissonnet, A. Zoulalian, et al. Mechanisms and Kinetics of Methane Thermal Conversion in a Syngas. *Industrial & Engineering Chemistry Research* 2009, 48, 6564-6572.

[4-44] S. Yuan, X. Chen, J. Li, F. Wang, CO_2 gasification kinetics of biomass char derived from high-temperature rapid pyrolysis. *Energy Fuels* 2011, 25, 2314-2321.

[4-45] T. Sueyasu, T. Oike, A. Mori, S. Kudo, K. Norinaga, J. Hayashi, Simultaneous steam reforming of tar and steam gasification of char from pyrolysis of potassium-loaded woody biomass. *Energy Fuels* 2012, 26, 199-208.

[4-46] Y. Hannachi, J. Mascetti, Metal insertion route of the Ni + CO_2 → NiO + CO reaction. *Journal of Physical Chemistry, A* 2003, 107, 6708-6713.

[4-47] F.W. Chang, T.J. Hsiao, S.W. Chung, J.J. Lo, Nickel supported on rice husk ash – activity and selectivity in CO_2 methanation. *Applied Catalysis A: General* 1997, 164, 225-236.

[4-48] M.T. Tsay, F.W. Chang, Characterization of rice husk ash – supported nickel catalysts prepared by ion exchange. *Applied Catalysis A: General* 2000, 203, 15-22.

[4-49] J. Tao, C. Dong, Q. Lu, H. Liao, X. Du, Y. Yang, E. Dahlquist, Catalytic cracking of biomass high-temperature pyrolysis tar using NiO/AC catalysts. *International Journal of Green Energy* 2014, in press.

Chapter 5

Conclusions and Recommdenations

5.1 Concluding Remarks

This thesis focuses on the development of a sustainable rice husk ash or char supported nickel catalyst for tar conversion in biomass high temperature pyrolysis/gasification. Preliminarily, rice husk char supported iron or nickel catalysts will be comparatively studied for tar *in situ* conversion via co-pyrolysis with raw biomass (i.e., rice husk). The metal nickel nanoparticles could be *in situ* generated and highly dispersed in the carbon matrix of rice husk char, which is further studied for tar conversion, including *in situ* and *ex situ*. Finally, the used rice husk char supported nickel catalyst is investigated for CO_2 gasification with the aim of recovering the energy from the char and recycling the silica-based nickel nanocomposite in the ash. The followings are the summary of findings in this thesis.

In Chapter II, an *in-situ* tar catalytic conversion has been developed for biomass gasification. By co-pyrolysis with rice husk char (RHC) or rice husk ash (RHA) supported Ni-Fe catalysts, the tar yield and the CO_2 concentration were significantly decreased in biomass gasification. In particular, the condensable tar conversion efficiency could reach about 92.3% by mixing with the RHC Ni-Fe catalyst; accordingly, the light tar with three- and four-ring aromatic compounds could significantly be transformed to single-ring organic compounds or gas molecules. It is noted that partial metal oxides were reduced into the metallic states, thereby enhancing the catalytic reactivity. Although the bimetallic RHC/RHA supported catalysts (i.e., RHA Ni-Fe, RHC Ni-Fe) exhibited a lower tar

conversion efficiency compared with the monometallic RHA Ni, the expense of the catalyst synthesis was much cheaper due to low-concentration Ni used. Moreover, omitting the calcination step, the preparation procedure of catalysts became much convenient and energy saving. Without steam, the synergetic effects between the activation of tar on the nickel species and the oxygen atom supplied to the carbonaceous intermediate from neighboring iron atoms was not displayed in dry reforming. The char-supported Ni catalyst is recommended to be employed for biomass gasification in an inert environment. Reacting with sufficient oxygen agents at high temperatures, the char-supported catalysts could be consumed, reducing their service life and increasing CO_2 concentration in the syngas. Nevertheless, the waste RHC Ni might be catalytically gasified to the syngas. Furthermore, by optimizing the operation parameters (e.g., the particle size, the mass fraction) in the mode of FBG, mixing with solid particles (e.g., sand, RHA supported catalysts) can improve the RH fluidization behavior. Consequently, the RH mass fraction of 0.5 and the particle diameter of 0.5 mm can be employed in the mixture of RH and RHA catalysts.

In Chapter III, an integrated concept of *in-situ* tar conversion and vapor upgrading has been proposed for pyrolysis of biomass, which was pretreated by nickel insertion combined with sodium borohydride ($NaBH_4$) modification. Significantly, it is a potential approach for *in-situ* generation of nickel nanoparticle catalysts in the carbon matrix. The ultra-low tar yield can be achieved by RH Ni and RH Ni-B pyrolysis, in terms of high conversion efficiencies of 96.9% and 98.6%, respectively, compared to the raw RH pyrolysis. On one hand, the removed tar was converted into the extra gases by the thermochemical reactions (i.e., the cracking, the reforming) with the nickel catalytic effect; on the other hand, the nickel catalyst can enhance the pyrolysis efficiency and restrain the formation of condensable tar due to polymerization. In addition, the condensed tar compounds existed mainly in the forms of mononuclear aromatics and oxygenated aromatic compounds. The condensable tar can be catalytically transformed into the non-condensable tar or small molecule gases. The metallic

nickel species coexisted with the nickel oxides caused by the partial reduction by carbon atom or reducing gas (e.g., CO). The formed polymolecularity Ni^0 may be attributed to the disproportionated reaction and the strong reducing property of $NaBH_4$. Compared to the catalysts preparation through the hydrogenation reduction under the strict conditions, this method is convenient and energy-saving. The condensable tar derived from RH pyrolysis could be significantly removed up to 96.5% and 92.6%, by co-pyrolysis with the RHC Ni and the RHC Ni-B, respectively.

The synthesized RHC Ni catalysts exhibited high catalytic performances on the tar conversion via co-pyrolysis with biomass. Meanwhile, the yield of product gas increased along with syngas upgrading, which is associated with the char further devolatilization and biomass tar catalytic conversion. Only small amounts of PAHs in the form of two-ring hydrocarbons (i.e., naphthalene) existed in the condensed tar derived from RH co-pyrolysis with the RHC Ni catalysts. Therefore, *in-situ* catalytic conversion could inhibit the micromolecular tars polymerization and eliminate the macromolecular tar generation. In addition, high specific surface areas of the RHC supported catalysts with micro- and meso-porous structures can extend the residence time of the tar cracking, thereby enhancing the tar reforming activity. However, the surface characteristics of RHC Ni (e.g., pore structure and surface area) can influence on the catalytic activity of the tar conversion in consideration of the carbon-based catalysts. It is anticipated that more metallic nanoparticles could be generated, if the time of pyrolysis (*i.e., carbothermal reduction*) is prolonged.

In Chapter IV, metallic nickel (Ni^0) nanoparticles could be successfully embedded in the amorphous carbon matrix via the carbothermal reduction by using waste biomass as a carbon source. The RHC Ni showed a good catalytic performance on tar reforming. In particular, the tar conversion efficiency could be increased with the increase of the catalyst weight and the reforming temperature. The tar reforming efficiency can reach about 50.1% by using 3 g of RHC Ni, while it significantly increased,

up to 99.8% by using 10 g of RHC Ni, maintaining a higher value of 99.3% after 5 cycles. It might be attributed to the enhancement of the catalytic reaction and the residence time. Besides, if 10 g of RHC Ni is employed, the tar conversion efficiency could be improved from 92.3% to 100% in the temperature range of 500-900 ^{o}C. It could indicate that RHC Ni showed a higher catalytic activity for the tar conversion even at lower temperatures. More importantly, without using the RHC Ni, more PAHs can be formed. Compared to the tertiary tars of PAHs, it is much easier to crack/reform the nascent tars by RHC Ni. When the RHC Ni was used for the catalytic reforming, the yield of liquid products was reduced from 30.2% to 10.7%; accordingly, the yield of gas product was greatly increased from 37.5% to 58.0%. Among these gas molecules, the volume fractions of CO and H_2 were increased from 21.2% to 33.5% and from 18.5% to 24.3%, respectively, attributed to the catalytic reforming over the RHC Ni. Moreover, the RHC Ni catalyst could be deactivated due to the coke deposition on the surface of the Ni actives. Consequently, the waste RHC Ni could be gasified into the additional syngas. The presence of nickel inside the char matrix can enhance the reactivity of CO_2 char gasification. After CO_2 gasification at high temperatures, the metallic nickel (Ni^0) is initially oxidized into the nickel oxide (NiO). However, the ash components are relative pure, mainly composed of NiO and SiO_2. Therefore, it has a potential to reuse a silica-based nickel catalysts.

5.2 Recommendations

Some research focus might be developed based on the present works as follows:

1. RHC or RHA supported catalysts (e.g., RHA NiO) should be preliminary studied for tar elimination in the pilot-scale FBG for biomass gasification. The operating conditions, such as the physical strength, the mass fraction and the particle size, should be investigated in detail.
2. To evaluate the catalytic performance with other commercial catalysts (e.g., Ni/SiO_2), the as-synthesized RHC Ni-Fe catalysts should be comparatively investigated for the dry or steam

reforming of tar compounds (e.g., phenols, naphthalene) to produce the value-added syngas with a high hydrogen content.

3. In order to compare the catalytic performances with other commercial catalysts, the catalytic kinetics and the catalyst longevity should be studied in a continuous pyrolysis-reforming facility.

4. Compared with CO_2 gasification, steam gasification of the waste RHC Ni should be evaluated.

Acknowledgements

Like a good movie ends with the credits, I should like to finish with thanking all the people that have in one way or another contributed to the making of this work.

Firstly, I would appreciate the *China Scholarship Council (CSC)* for the financial support under the grant No.201206230168. Meanwhile, I would like to sincerely thank Prof. Kunio Yoshikawa and associate Prof. Fumitake Takahashi for their help and guidance and for giving me the opportunity to work at one of the acclaimed *Tokyo Institute of Technology* among not only brilliant scientists but people that, after two and a half exciting years, I consider dear friends. I would appreciate associate Prof. Kouji Tokimatsu for his kind suggestion and guidance on my life and work. Mr. Zhao, Mr. Ma and Mr. Shao are thanked for helping me conduct all kinds of the experiments. I would like to thank Dr. Suzuki in the analysis center of Ookayama campus for her assistance to conduct the XRD, FTIR and TEM measurements as well. I want to thank all my other dear friends in a warm family at Yoshikawa laboratory: Ms. Yang, Mr. Wu, Mr. Lin, Mr. Liu, Ms. Nid, Mr. Kunta, Ms. Peng, Mr. Pi, Mr. Bakhtiyor, Ms. Xue, Mr. Nakamura, and many more for scientific discussions and, more importantly, for so many non-scientific fun hours! Special thanks go to whom for taking care of me in times of need. I am indebted to so many people for making my days and nights that much fun and the past years the experience of a life time, that I have probably forgotten to mention some of you, but I wholeheartedly thank each and every one of you none the less; it's been an honor meeting you. I would also like to thank Prof. Tonghua Sun and Prof. Jinping Jia in *Shanghai Jiaotong University* for their kindly guidance on the research work and the future career. They look like a lighthouse guiding my life way in the dark sea. Finally, I would be sincerely grateful of my family members (special thanks to my parents) for their support, care and concern all the way during the process of pursing my dreams.